# Biophysical insights into the conformational flexibility of AUX/IAA transcriptional repressors for auxin sensing

Dissertation

zur Erlangung des

Doktorgrades der Naturwissenschaften (Dr. rer. nat.)

der

Naturwissenschaftlichen Fakultät I – Biowissenschaften –

der Martin-Luther-Universität Halle-Wittenberg

vorgelegt

von Herrn

Jhonny Oscar Figueroa Parra

geboren am 07.04.1990 in Caracas

Gutachter:

I.     Prof. Dr. Steffen Abel

II.    Prof. Dr. Andrea Sinz

III.   Prof. Dr. Dolf Weijers

Date of defense: 05.02.2024

"Die Entropie der Welt strebt einem Maximum zu"

Rudolf Clausi

# Table of Contents

i

# Summary

Intrinsically disordered proteins and disordered regions, here collectively referred as IDR(s), bind through different protein-protein binding modes leading to the regulation of diverse cellular processes *in vivo*. IDRs structure fluctuates in native conditions, as they do not fold into a stable three-dimensional (3D) structure. Instead, IDRs are dynamic, may compact and extend, therefore creating an ensemble of multiple and heterogeneous conformations. Also, structural fluctuations in IDRs may expose multiple binding motifs making them hubs in cellular signaling networks.

In plants, the family of <u>AUX</u>IN/<u>I</u>NDOLE-3-<u>A</u>CETIC <u>ACID</u> (AUX/IAA) transcriptional repressors are central for auxin-driven growth and development, as they integrate repression and auxin sensing functions. AUX/IAAs dual role is mainly accomplished by three functional domains connected to each other by IDRs of variable length and amino acid composition. The N-terminal EAR motif and the C-terminal PB1 domain possess repression function, while a 13-residues long degron motif in between the former is essential for auxin sensing. AUX/IAAs repression functions are overruled by auxin, a small tryptophan derivate phytohormone. Auxin is sensed in the nucleus by a <u>S</u>KP1 <u>C</u>ULLIN1 <u>F</u>-BOX (SCF)- E3 ligase together with its substrates AUX/IAAs. Specifically, AUX/IAAs degron, locks an auxin molecule into a pocket in the <u>T</u>RANSPORT <u>I</u>NHIBITOR <u>R</u>ESPONSE <u>I</u>/<u>AUX</u>IN <u>F</u>-<u>B</u>OX PROTEIN <u>1-5</u> (TIR1/AFB1-5). Nuclear auxin sensing leads to the polyubiquitylation of AUX/IAAs targeting them for proteasomal degradation. This activates auxin transcriptional response by derepression of <u>AUX</u>IN <u>R</u>ESPONSE <u>F</u>ACTORS (ARFs) transcription factors. In *Arabidopsis thaliana*, 23-degron containing AUX/IAAs differentially respond to varying intracellular levels of auxin regulating a plethora of cellular processes. They include embryonic and postembryonic development, tropisms, cell division, cell differentiation and cell elongation.

Recent structural proteomics data showed that IDRs flanking the degron, as well as the AUX/IAAs PB1 domain bind to the top surface of TIR1 during auxin perception. Here, AUX/IAAs cover the top mushroom-shape like surface of TIR1 and it was proposed that sequence divergence among AUX/IAAs degron flanking regions influence the binding to auxin. For instance, domain swap between two different AUX/IAAs, IAA7 and IAA12, showed that the IDRs and PB1 regions may enhance or diminish auxin binding affinity. Together with other biochemical and *in planta* data, these results indicated that AUX/IAA regions that surround the degron, which interact with TIR1 may positively or negatively influence auxin binding affinity by TIR1·AUX/IAAs complexes. However, from a structural point of view, the exact binding mechanism of AUX/IAAs degron flanking regions to TIR1, remains elusive.

This work broadens the structural understanding of the binding mode between TIR1 and AUX/IAA proteins in auxin perception using biophysical techniques and coarse-grained (CG) modeling. The data show that the N-terminal IDR length of AUX/IAAs is inversely proportional to their compactness and directly proportional to their conformational space in the free state. Single-molecule Förster resonance energy transfer (smFRET) was used to determine TIR1·AUX/IAA conformational ensembles *in vitro*. Using IAA7 as a representative of the AUX/IAA family, the results indicate that the IAA7 conformational ensemble changes from compact in the free state to expanded in the TIR1-bound state. Binding affinity experiments reveal that the IDR and PB1 of IAA7 allosterically enhance its affinity towards TIR1.

Additionally, a combination of crosslinking mass spectrometry (XL-MS) and CG-simulation data show that AUX/IAA conformations are highly heterogeneous or "fuzzy" on the top surface of TIR1 during auxin perception. This conformational heterogeneity is greater in AUX/IAAs with longer IDRs, allowing multiple inter-residue contacts between TIR1 and AUX/IAAs. It is proposed that this "fuzzy" binding mode of AUX/IAAs has two significant functional outcomes: first, it enhances the binding affinity between TIR1 and AUX/IAAs for the formation of the auxin receptor complex; second, it facilitates the polyubiquitylation of AUX/IAAs at different lysine residues, enabling them to sample the active site of the SCF$^{TIR1/AFBs}$ E3 ligase.

# Zusammenfassung

Intrinsisch ungeordnete Proteine und ungeordnete Regionen, hier gemeinsam als IDR(s) bezeichnet, binden über unterschiedliche Protein-Protein-Bindungsmodi, was zur Regulierung verschiedener zellulärer Prozesse *in vivo* führt. Die Struktur von IDRs schwankt unter natürlichen Bedingungen, da sie sich nicht zu einer stabilen dreidimensionalen (3D) Struktur falten. Stattdessen sind IDRs dynamisch, können sich verdichten und ausdehnen und so ein Ensemble aus mehreren und heterogenen Konformationen erzeugen. Außerdem können strukturelle Schwankungen in IDRs mehrere Bindungsmotive freilegen, die sie zu Knotenpunkten in zellulären Signalnetzwerken machen.

In Pflanzen ist die Familie der AUX/IAA-Transkriptionsrepressoren von zentraler Bedeutung für Auxin-gesteuertes Wachstum und Entwicklung, da sie Repressions- und Auxin-Sensorfunktionen integrieren. Die Doppelrolle von AUX/IAAs wird hauptsächlich durch drei funktionelle Domänen erfüllt, die durch IDRs unterschiedlicher Länge und Aminosäurezusammensetzung miteinander verbunden sind. Das N-terminale EAR-Motiv und die C-terminale PB1-Domäne besitzen eine Repressionsfunktion, während ein 13 Reste langes Degron-Motiv zwischen ersteren für die Auxin-Erkennung essenziell ist. Die Repressionsfunktionen von AUX/IAAs werden durch das Phytohormon Auxin, ein kleines Tryptophan-Derivat, außer Kraft gesetzt. Auxin wird im Zellkern von einer S̲KP1 C̲ULLIN1 F̲-BOX (SCF)-E3-Ligase zusammen mit seinen AUX/IAA-Substraten wahrgenommen. Insbesondere fixiert das Degron von AUX/IAA ein Auxinmolekül in einer Tasche im T̲RANSPORT I̲NHIBITOR R̲ESPONSE 1/A̲UXIN F̲-B̲OX PROTEIN 1̲-5̲ (TIR1/AFB1-5). Die nukleare Auxin-Erkennung führt zur Polyubiquitylierung von AUX/IAAs, wodurch diese vom Proteasom abgebaut werden. Dies aktiviert die transkriptionelle Antwort von Auxin durch Derepression der Transkriptionsfaktoren A̲UXIN R̲ESPONSE F̲ACTORS (ARFs). In *Arabidopsis thaliana* reagieren 23-Degron-haltige AUX/IAAs unterschiedlich auf variierende intrazelluläre Auxinkonzentrationen und regulieren eine Vielzahl von zellulären Prozessen. Dazu gehören die embryonale und postembryonale Entwicklung, Tropismen, Zellteilung, Zelldifferenzierung und Zellstreckung.

Aktuelle strukturelle Proteomikdaten zeigten, dass sowohl Degron-flankierende IDRs als auch die AUX/IAA-PB1-Domäne während der Auxin-Wahrnehmung an die Oberfläche von TIR1 binden. Hierbei bedecken AUX/IAAs die obere pilzförmige Oberfläche von TIR1 und es wurde postuliert, dass die Sequenzdivergenz zwischen AUX/IAA-Degron-flankierenden Regionen die Bindung an Auxin beeinflusst. Beispielsweise zeigte der Domänenaustausch zwischen zwei verschiedenen AUX/IAAs, IAA7 und IAA12, dass die IDRs und PB1-Regionen die Auxin-Bindungsaffinität

erhöhen oder verringern können. Zusammen mit anderen biochemischen und *in planta*-Daten deuten diese Ergebnisse darauf hin, dass AUX/IAA-Regionen, die das Degron umgeben und mit TIR1 interagieren, die Auxin-Bindungsaffinität von TIR1·AUX/IAA-Komplexen positiv oder negativ beeinflussen können. Aus struktureller Sicht bleibt jedoch der genaue Bindungsmechanismus der Degron-flankierenden Regionen von AUX/IAAs, die an TIR1 binden, unklar.

Diese Arbeit erweitert das strukturelle Verständnis des Bindungsmodus zwischen TIR1 und AUX/IAA-Proteinen bei der Auxinwahrnehmung unter Verwendung biophysikalischer Techniken und grobkörniger Modellierung. Die Daten zeigen, dass die Länge des N-terminalen IDR von AUX/IAAs umgekehrt proportional zu ihrer Kompaktheit und direkt proportional zu ihrem konformationellen Raum im freien Zustand ist. Einzelmolekül-Förster-Resonanzenergietransfer (smFRET) wurde verwendet, um TIR1·AUX/IAA-Konformationsensembles *in vitro* zu bestimmen. Anhand von IAA7 als Vertreter der AUX/IAA-Familie zeigen die Ergebnisse, dass sich das IAA7-Konformationsensemble vom kompakten Zustand im freien Zustand in einen expandierten Zustand im TIR1-gebundenen Zustand ändert. Bindungsaffinitätsexperimente zeigen, dass der IDR und PB1 von IAA7 allosterisch die Affinität zu TIR1 erhöhen.

Zusätzlich zeigt eine Kombination aus Crosslinking-Massenspektrometrie (XL-MS) und grobkörnigen (CG) Simulationsdaten, dass die AUX/IAA-Konformationen auf der Oberseite von TIR1 während der Auxinwahrnehmung hochgradig heterogen oder „fuzzy" sind. Diese konformationelle Heterogenität ist bei AUX/IAAs mit längeren IDRs größer und ermöglicht mehrere interresiduale Kontakte zwischen TIR1 und AUX/IAAs. Es wird vorgeschlagen, dass dieser „fuzzy" Bindungsmodus von AUX/IAAs zwei bedeutende funktionale Auswirkungen hat: Erstens erhöht er die Bindungsaffinität zwischen TIR1 und AUX/IAAs zur Bildung des Auxin-Rezeptorkomplexes; zweitens erleichtert er die Polyubiquitylierung von AUX/IAAs an verschiedenen Lysinresten, wodurch sie das aktive Zentrum der SCFTIR1/AFBs E3-Ligase erreichen können.

# List of abbreviations

| | |
|---|---|
| 3D | Three-dimensional |
| *a.k.a* | also known as |
| AFB1-5 | AUXIN F-BOX PROTEIN from 1 to 5 |
| AID | Auxin-inducible degron |
| ARFs | AUXIN RESPONSE FACTORS |
| *At* | *Arabidopsis thaliana* |
| AUX/IAA(s) | AUXIN/INDOLE-3-ACETIC ACID protein(s) |
| CD | Circular dichroism |
| CG | Coarse-grained |
| CI | Compaction index |
| C-terminal | Carboxy-terminal |
| CV | Coefficient of variation |
| Da | Dalton |
| DLS | Dynamic light scattering |
| *E* | Energy transfer efficiency |
| *e.g.* | *exempli gratia* – for example |
| EAR | Ethylene response factor-associated amphiphilic |
| ELM | Eukaryotic linear motif |
| EOM | Ensemble optimization method |
| FBPs | F-BOX PROTEINS |
| FCCS | Fluorescence cross correlation spectroscopy |
| FWHM | Full width at half maximum |
| *i.e.* | *id est* – that is |
| IAA | Indole-3-acetic acid |
| IAA"number" | Individual AUX/IAA protein |
| IDR(s) | Intrinsically disorder proteins or intrinsically disordered regions |
| IVU | *In vitro* ubiquitylation (reaction) |
| Kd | Dissociation constant |
| LCRs | Low complexity regions |
| LLPS | Liquid-liquid phase separation |
| M | molar |

| | |
|---|---|
| MoRFs | Molecular recognition features |
| ms | Microseconds |
| MST | Microscale thermophoresis |
| N8 = NEDD8 | NEURAL PRECURSOR CELL EXPRESSED, DEVELOPMENTALLY DOWNREGULATED8 |
| NLS | Nuclear localization signal |
| nm | Nanometers |
| NMR | Nuclear magnetic resonance |
| N-terminal | Amino-terminal |
| PB1 | Phox Beam 1 |
| PDD | Probability of disorder |
| *Pp* | *Physcomitrium patens* |
| *Ps* | *Pinsum sativum* |
| PTMs | Postrasnlational modifications |
| RBA | Radiolingand binding assay |
| $R_{ee}$ | End-to-end distance |
| $R_g$ | Radius of gyration |
| $R_S$ | Stoke radius |
| SAXS | Small angle X-ray scattering |
| SCF | SKP1 CUL1 F-BOX |
| SLiMs | Short linear motifs |
| SLS | Static light scattering |
| smFRET | Single molecule Förster resonance energy transfer |
| *So* | *Sisymbirum orientale* |
| TIR1 | TRASNPORT INHIBITOR RESPONSE 1 |
| TPL, TPD, TPR | TOPLESS, TOPLESS domain, TOPLESS-RELATED |
| Ub | Ubiquitin |
| UPS | Ubiquitin proteasome system |
| XL-MS | Crosslinking mass spectrometry |

Throughout this thesis the amino acid three-letter or one-letter code is used according to IUPAC-IUB (recommendations 1983).

# List of figures

# List of supplementary figures

# List of tables

# List of supplementary tables

# 1. Introduction

## 1.1 Widespread entropy within thermodynamic systems

In thermodynamic systems, energy transfer and matter behavior change in response to variations in temperature, pressure, and volume (J. G. Morris, 1974). Entropy is an intrinsic property of these systems (Michaelides, 2008), reflecting the degree of disorder and the number of accessible microstates available to the system (Brady & Sharp, 1997). For instance, in the case of gases, argon has a higher entropy than helium under the same temperature and pressure conditions because argon atoms have more degrees of freedom (such as more possible positions and velocities) due to their larger mass and size. Consequently, the entropy of argon is greater than that of helium (Michaelides, 2008).

In structural biology, the same thermodynamic laws apply to proteins and protein complexes. Protein folding occurs due to specific and favorable intramolecular interactions, such as hydrogen bonds, salt bridges, hydrophobic contacts, and disulfide bonds (Brady & Sharp, 1997). This folding process typically results in a decrease in the entropy of the protein itself, as it transitions from a more disordered, unfolded state to a more ordered, folded state. However, the overall entropy of the system, which includes the protein and the surrounding solvent, can increase due to thof water molecules from hydrophobic regions into the bulk solvent.Conversely, in intrinsically disordered proteins (IDPs), strong intramolecular electrostatic repulsion and reduced hydrophobic interactions prevent the protein from adopting a single, stable folded structure. This results in a higher conformational entropy for IDPs, as they remain flexible and can sample a wide range of conformations (Uversky, 2019).

## 1.2 Featuring intrinsically disordered protein: from amino acid sequence to structure(less), to functions

Over the past decades IDRs have gained recognition in mainstream biology due to their prominent role in cellular processes. In fact*, in silico* analyses using disordered predictors have evidenced that between ~30-40% of the eukaryotic proteome contains an intrinsically disordered region (IDR(s)) (proteins with >30% disordered residues) (Edwards, Lobley, Pentony, & Jones, 2009). In the model plant, *Arabidopsis thaliana* 29.5% of the proteome is predicted to be IDRs (Pietrosemoli, García-Martín, Solano, & Pazos, 2013). IDPs and IDRs (hereafter referred collectedly as IDR(s)) lack of a stable 3D structure showing structural plasticity and entropy-driven motions (Felli, Gonnelli, & Pierattelli, 2014; Uversky, 2019). Particularly, IDRs structure fluctuates under native conditions (pH, osmolarity and temperature) exhibiting a high degree of flexibility.

This is attributed to their biased amino acid composition with a higher proportion of charged residues over hydrophobic ones (Trivedi & Nagarajaram, 2022). Larger number of charged residues increases IDRs net charge, promoting electrostatic repulsion and hydrogen bonding with the surrounding aqueous solvent (Newberry & Raines, 2019). Also, low number of hydrophobic residues prevents the formation of hydrophobic interactions, which typically would drive folding by repelling water and forming protein's hydrophobic core (Trivedi & Nagarajaram, 2022; Uversky, 2019). In general, IDRs contain more frequently alanine (A), lysine (K), glutamine (Q), serine (S), glutamic acid (E), and proline (P); and, are depleted in cysteine (C), tryptophan (W), isoleucine (I), tyrosine (Y), phenylalanine (F), leucine (L), histidine (H), valine (V), asparagine (N) and methionine (M) compared to folded proteins (Uversky, 2019) (**Figure 1**). IDRs play a central role in the regulation of signaling pathways, regulations of transcription, translation and cellular processes (Wright & Dyson, 2015). In biochemistry, IDRs are referred as moonlight proteins which refers to the ability to carry out and coordinate more than one function (Gupta & Uversky, 2023).
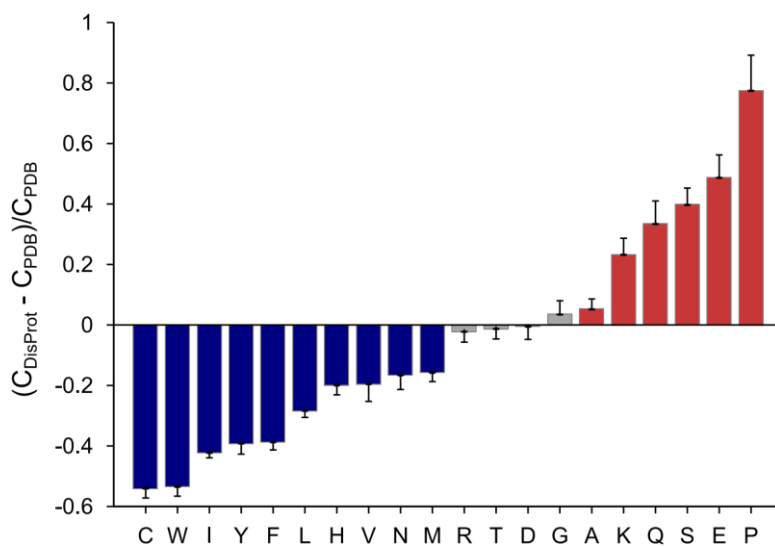


**Figure 1. Bias amino acid composition of IDRs favors primarily polar and charged residues over hydrophobic ones.** IDRs from the DisProt database (https://disprot.org/) were compared with the PDB Select 25 dataset, a subset folded proteins with less than 25% of sequence identity from the Protein Data Bank (PDB). The plot shows the fractional amino acid composition difference between IDRs and folded proteins. The fractional difference was calculated with the equation: $C_{DisProt}$-$C_{PDB}$/$C_{PDB}$, where $C_{DisProt}$ is the amino acid composition in the $Dis_{Prot}$ database and $C_{PDB}$ is the amino acid composition in the PDB dataset. Negative bars, colored in blue show depleted residues (p≤0.01), gray bars show amino acids with no significant differences (p>0.01) and positive red bars show enriched amino acids (p≤0.01) for IDRs. The plot was generated in the sequence profile server: http://www.cprofiler.org/cgi-bin/profiler.cgi (Vacic, Uversky, Dunker, & Lonardi, 2007).

## 1.3 Structural and functional implications of IDRs conformational ensemble and conformational heterogeneity

IDRs cover a wide range of conformations compared to folded proteins or flexible multidomain proteins (**Figure 2**) (Hraber et al., 2020). The study of IDRs conformational ensemble seeks to extract biological relevant conformations that enable researchers to stablish an IDRs ensemble/function relationship (Mittag et al., 2010). Functionally, the conformational heterogeneity of IDRs permits a window in which IDRs can engage with multiple interaction partners after exposing multiple linear binding motifs along their amino acid sequence (Bondos, Dunker, & Uversky, 2021; Wright & Dyson, 2015). Contrary to folded proteins, IDRs binding modes are diverse given their conformational heterogeneity. For instance, IDRs binding motifs may fold or remain disordered in the target bound state. The binding modes of IDRs will be discussed in the next sections.

| Folded protein | Flexible multidomain protein | IDRs |
|---|---|---|

PDB: 2M1M | PDB: 2MJN | PED: 00001

Conformational heterogeneity
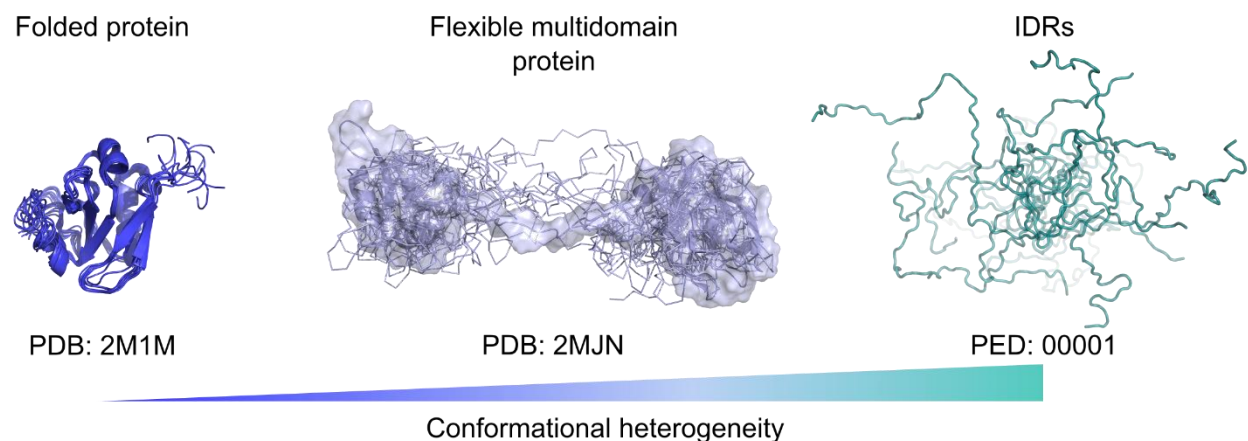
**Figure 2. IDRs ensembles show the highest conformational heterogeneity compared to folded and flexible multidomain proteins.** Protein structures display multiple conformations in solution ranging from relatively small to large. The conformational heterogeneity of folded proteins is relatively small due to favorable intraprotein interactions. Folded domains change their conformation with respect to each other when connected by flexible linkers. IDRs represent the highest level of conformational heterogeneity due to entropic intraprotein forces that prevent folding into a fixed 3D structure. This figure shows the ensemble structures of the *Pisum sativum* (*Ps*) IAA4[PB1] as folded protein example; the TIA-1 as flexible multidomain protein; and ten representative structures from pSic conformational ensemble available in Protein Ensemble Database (https://proteinensemble.org/). Figure modified from Hraber et al., 2020.

## 1.4 IDRs serve as hubs within signaling networks

IDRs are considered central nodes or hubs in signaling pathways, as they establish multiple protein-protein interactions through linear binding motifs (Figueiredo & Strader, 2022). They serve as multipurpose proteins given their ability to response to the cellular environment for sensing functions or function on multiple interacting partners depending on the cellular conditions. Multiple

binding sites also enable allosteric regulation in biological signaling, this means that the binding to one target may influence the way that an IDR interacts with other partners changing its function. Linear binding motifs may also expose recognition sites to protein kinases, acetylases, methylases, or other enzymes resulting in different signaling outputs via posttranslational modifications (Wright & Dyson, 2015). Hence, the structural and functional plasticity of IDRs increases the complexity of signaling pathways. In plants, the protein family of A̲UXIN/I̲NDOLE-3-A̲CETID A̲CID (AUX/IAA) display such a hub role carrying a dual function as transcriptional repressors, and auxin sensing functions through an IDR (Figueiredo et al., 2022; Figueiredo & Strader, 2022; Niemeyer et al., 2020; Ramans-Harborough et al., 2023). AUX/IAAs IDRs interact with multiple binding partners enabling such a dual role *in vivo*. In *Arabidopsis thaliana* 23 AUX/IAAs respond to intracellular levels auxin regulating key developmental growth processes in plants (Overvoorde et al., 2005; Tria, Mertens, Kachala, & Svergun, 2015). Furthermore, IDRs in AUX/IAAs carry additional features that are postulated to mediate their half-lives *in vivo* permitting to act as rapid transcriptional regulators via protein degradation (Dreher, Brown, Saw, & Callis, 2006; B. L. Moss et al., 2015). AUX/IAAs structural features and roles in protein signaling will be discuss in the next sections.

## 1.5 IDRs carry different protein-protein interaction sequence modules for cellular functions

IDRs have a prominent function in mediating protein-protein interactions that regulate cellular processes (Cermakova & Hodges, 2023; Wright & Dyson, 2015). IDRs fulfill their function, primarily through multiple and conserved linear binding motifs that interact with nucleic acids or other proteins (Cermakova & Hodges, 2023). More than 100,000 linear binding motifs are predicted in the human proteome which represents 50 times more the number of the predict humans' proteins (Aebersold et al., 2018; Hraber et al., 2020). Thus, this highlights the importance of IDRs for mediating protein-protein interactions.

Based on their primary sequences and conformation in the target bound state, linear binding motifs may be grouped into three modules, these include: 1) m̲olecular r̲ecognition f̲eatures (MoRFs), 2) s̲hort l̲inear m̲otifs (SLiMs), and 3) l̲ow c̲omplexity r̲egions (LCRs) (O. M. Morris, Torpey, & Isaacson, 2021; van der Lee et al., 2014). MoRFs are 10-70 residues long motifs which function in the molecular recognition of interaction partners (Mohan et al., 2006; Vacic et al., 2007). MoRFs conformation changes from disordered in the free state to order in the target bound state. They are classified into four types according to the secondary structure accomplished in the target bound state. α-MoRFs, form α-helices; β-MoRFs form β-strands; ι-MoRFs, which forms

irregular structures; and, finally, complex-MoRFs, which form a mixture of secondary structures (Mohan et al., 2006; Vacic et al., 2007) (**Figure 3**).

SLiMs are short conserved sequences, up to 10 residues long which can be either ordered or disordered in the target bound state (van der Lee et al., 2014; Van Roey et al., 2014). Since the bound state conformation of SLiMs can be either ordered or disordered, this contrasts with the binding mode of MoRFs where folded structures are always formed. From the functional point of view, MoRFs and SLiMs are undifferentiable and may be collectively referred to as eukaryotic linear motifs (ELM). Currently, 4029 experimentally validated ELMs covering 267 taxons are available in the ELM resource repository (http://elm.eu.org/) (Kumar et al., 2019). ELMs can be assigned to six categories according to their functions, which includes: proteolytic cleavage sites; degradation site, part of polyubiquitylation; docking sites, involved in protein recruitment but no directly targeted by an active site; ligand binding sites, primarily for protein-protein interactions; posttranslational modifications sites; and, targeting sites for subcellular localization (Hraber et al., 2020).

Low complexity regions in IDRs are highly repetitive sequences with only one or few type of residues that exhibit a high level of binding promiscuity (O. M. Morris et al., 2021). LCRs drive protein aggregation during the development of neurodegenerative diseases such Alzheimer disease (Shim, Kang, Youn, An, & Kim, 2022). LCRs also participate in the formation of biomolecular condensates which are a kind of membraneless cellular compartments with concentrated proteins, nucleic acids and other biomolecules which regulate protein activity, buffering and intracellular localization of biomolecules (Martin & Mittag, 2018).
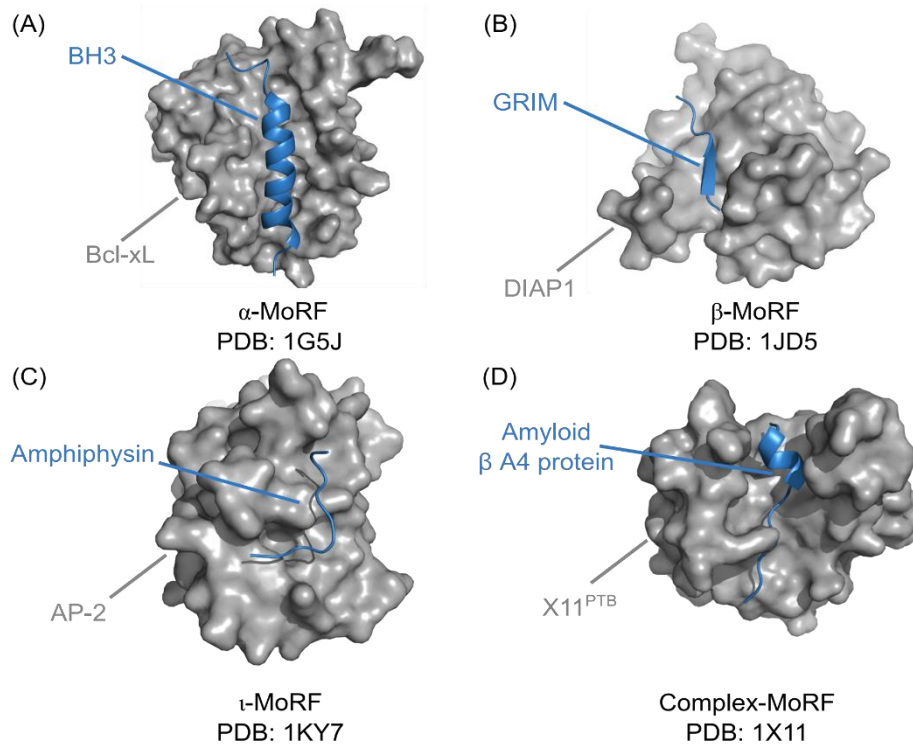
**Figure 3. Structural representation of MoRFs classification based on the secondary structure in the bound state.** Folded partners are shown in surface representation colored in gray and MoRFs in blue cartoon representation. (A) α-MoRF. BH3 domain of BAD bound to Bcl-xL. (B) β-MoRF. Inhibitor of apoptosis protein DIAP1 bound to N-terminus of cell death protein GRIM. (C) ι-MoRF. AP-2 (partner) bound to the recognition motif of amphiphysin. (D) Complex-MoRF. Phosphotyrosine-binding domain (PTB) of the X11 protein bound to amyloid β A4 protein. Models were built in pymol for this dissertation using as reference: Vladimir Vacic et al., 2007.

## 1.5.1 IDRs bind through diverse protein-protein interaction binding modes to fulfill their function

IDRs may adopt different structure types when bond with a binding partner (Fuxreiter, 2020a, 2020b; van der Lee et al., 2014). The elucidation of IDRs conformation in the target bound state is essential for understanding how IDRs carry out their function in the regulation of cellular processes via protein-protein interaction. Additionally, understanding how IDRs perform their biological functions is key for the development of new therapeutics and biotechnological products that target IDRs binding (Thomasen & Lindorff-Larsen, 2022). This is of special importance in the medical field since IDRs are often involved in the dysregulation of cellular processes leading to diseases. Some examples of IDRs linked to diseases are α-synuclein in Alzheimer (Shim et al., 2022), the amyloid β peptide in Parkinson (Coskuner & Uversky, 2019), and huntingtin linked Huntington's disease (Birol & Melo, 2019).

IDRs interactions with a protein partner may result in multiple structural outcomes. For instance, IDRs may fold upon binding, or they may as well remain highly disordered in the target bound state. Alternately, IDRs may exhibit varying degrees of order and disorder conformations in the bound state. Thus, the bound state of IDRs is conceptually considered as a probability continuum between order and disorder bound states (Fuxreiter, 2018) (**Figure 4**). The bound state is defined as the probability of disorder ($P_{DD}$) in the bound state. Where $P_{DD} = 0$ represents order in the bound state, while $P_{DD} = 1$ represents disordered in the bound state (Fuxreiter, 2018, 2020a). Intermediate $P_{DD}$ values represent different degrees of disorder or conformational heterogeneity. IDRs binding modes include disorder-to-order transition, disordered binding and fuzzy binding.

## 1.5.2 IDRs conformation is stabilized through disorder-to-order transition binding modes

Disorder-to-order transition results when an IDR binds to a folded protein partner resulting in a stabilized conformation of the IDR binding motif (**Figure 4**) (Fuxreiter, 2018, 2020a; O. M. Morris et al., 2021; van der Lee et al., 2014). Here, IDRs interaction with a binding partner reduces entropic driven-motions resulting in a single conformation of the IDR binding motif (Fuxreiter, 2020a). All MoRFs and most of SLiMs in IDRs bind via disorder-to-order transition.

## 1.5.3 IDRs maintain their conformational heterogeneity in disordered binding mode

Disorder binding mode *a.k.a.* disorder-to-disorder binding, occurs when two or more disordered partners keep their conformational heterogeneity in the target-bound state (**Figure 4**) (Fuxreiter, 2018, 2020a; O. M. Morris et al., 2021). In this case, a folded or stable conformation of IDRs is never formed when bound to its target. Disorder-to-disorder bound complexes have high-entropy states (Fuxreiter, 2018, 2020a). For instance, multiple structural methods have shown that human histone H1 (H1) and the nuclear chaperon prothymosin-α (proTα) retain their structural disorder in the complex bound state (Borgia et al., 2018). Despite being highly disordered, H1 and proTα bind in a picomolar binding affinity due to a strong electrostatic interaction with ProTα carrying forty-four negative charges and H1 fifty-three positive charges (Borgia et al., 2018). Proteins that form biomolecular condensates bind through disordered binding mode. Here, multiple interactions are achieved by favorably interacting residues spaced by IDRs linkers following the spacer-sticker model (Choi, Holehouse, & Pappu, 2020). Therefore, it has been proposed that in disorder-to-disorder binding mode, multiple, yet separate amino acids promote protein-protein interactions

7

contrasting with disorder-to-order binding mode, which is carried out by SLiMs/MoRFs (Choi et al., 2020).
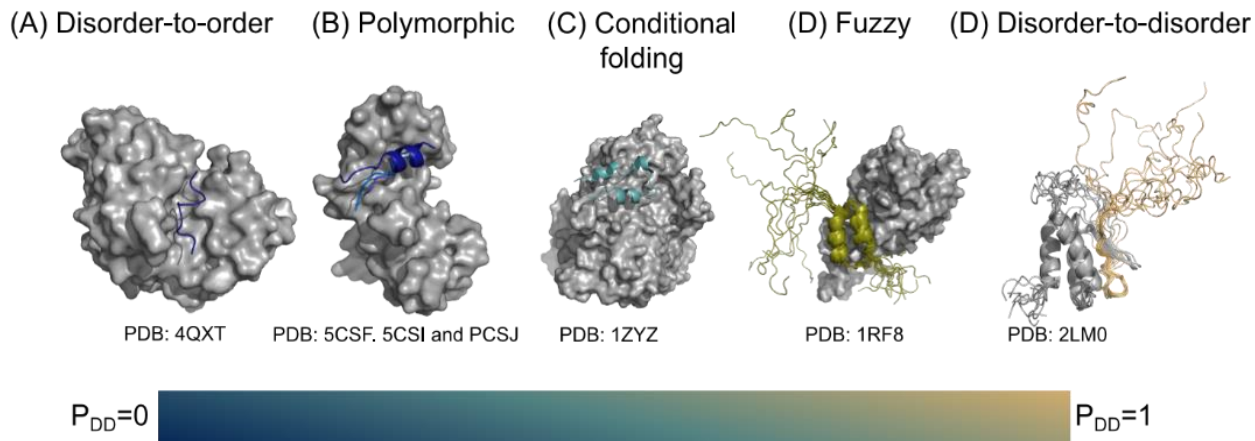


**Figure 4. Multiplicity of IDRs binding modes ranges from completely folded to completely disorder in the target bound-state.** IDRs binding modes span between a $P_{DD} = 0$ (blue) when they fold upon-binding, or a $P_{DD} = 1$ (beige) when they remain disorder in the bound state. Intermediate $P_{DD}$ values are expected to IDRs with heterogeneous conformations in the bound state. IDRs binding modes includes: (A) Disorder-to-order transition: the merozoite surface protein 2 of Plasmodium falciparum folds upon interacting with the monoclonal antibody m6D8. (B) Ribosomal S6 kinase 1 adopts different secondary structures upon binding to S100B, corresponding to the autoinhibited and active forms. (C) The N-terminal region (15e45 AA) of ribonucleoside-diphosphate reductase large chain conditionally folds depending on its partner. (D) The p150 subunit of the eukaryotic initiation factor 4F wraps around the translation initiation factor 4E, but its N-terminal flanking region (215e235 AA) is not constrained in the assembly. (D) Disorder binding: Upon interactions between leukemia fusion protein AF9 and elongation factor AF4 both partners retain considerable conformational heterogeneity. Modified from Fuxreiter, 2018.

## 1.5.4 IDRs fuzzy binding mode covers a wide spectrum of structural types and protein topologies in the target-bound state

IDR's fuzzy binding mode is considered context-dependent, since it is determined by protein behavior in response to external factors such as posttranslational modifications, changes in subcellular localization, temperature, osmolarity, concentration of a given metabolite, pH, etc. (Hatos et al., 2023). (Fuxreiter, 2018, 2020a; O. M. Morris et al., 2021; Sharma, Raduly, Miskei, & Fuxreiter, 2015). Fuzzy binding represents the most diverse binding mode of IDRs, since different types of structure(less) and protein topologies may be formed when IDRs bind to their targets (Fuxreiter, 2020a, 2020b; Sharma et al., 2015) (**Figure 4**). From the biological point of view, fuzzy binding increases the opportunities of IDRs binding in order for IDRs to perform a specific function depending of the cellular conditions (Fuxreiter, 2020b).

## 1.6 AUX/IAAs intrinsic disorder tunes auxin perception

Auxins are a class of tryptophan-derivate plant hormones which regulate a vast number of growth and development processes *e.g.* cell signaling, cell cycle regulation, endocytosis, embryogenesis, organogenesis (Hadfi, Speth, & Neuhaus, 1998; C. Liu, Xu, & Chua, 1993; Paciorek et al., 2005; Skoog & Miller, 1957). In plants, the most abundant form of auxins in plants is indole-3-acetic acid (IAA), and it is typically referred to just as auxin (Bandurski & Schulze, 1977; Ljung, Bhalerao, & Sandberg, 2001; Ljung et al., 2005). Auxin is sensed in the nucleus by an SKP1 CULLIN1 F-BOX PROTEIN (SCF)-type E3 ubiquitin ligase together with its substrates AUX/IAAs (Tan et al., 2007). F-Box proteins (FBPs) act as modular E3 ubiquitin ligase adaptor proteins within SCF complexes (named after their main components, SKP1, CULLIN, and an F-box proteins), in which they bind substrates for ubiquitin-mediated proteolysis (Skaar, Pagan, & Pagano, 2013). SCF complexes facilitate interaction between substrates and ubiquitin-conjugating enzymes, which then covalently transfer ubiquitin onto substrates. Polyubiquitylated substrates are subsequently degraded by the 26S proteasome (Davis, Spaller, & Matouschek, 2021). SCF complexes differ only in the FBP subunit, and the ability of the SCF backbone to bind multiple FBP, each with specific substrate specificity, substantially increases the substrate repertoire (Kipreos & Pagano, 2000). While some redundancy in terms of substrate binding exists between FBPs from different subfamilies, in general each FBP has a unique repertoire of substrates and pathways that it regulates (Craig & Tyers, 1999) . The ultimate regulation of the activity of specific SCF complexes occurs at the level of substrate recruitment (Jin, Ang, Shirogane, & Wade Harper, 2005). In response to stimuli, FBPs must rapidly and specifically bind their target proteins in the complex cellular milieu and recruit them to the core SCF scaffold, which exerts ubiquitin ligase activity. Conversely, binding between an FBP and its substrate can be perturbed in response to stimuli. Therefore, both FBP–substrate interfaces and the FBPs themselves are subject to tight regulation (Schmidt, McQuary, Wee, Hofmann, & Wolf, 2009; Skaar et al., 2013). Among eukaryotes, plants contain unique systems for SCF target recognition mediated by small molecules *a.k.a* phytohormones (Gagne, Downes, Shiu, Durski, & Vierstra, 2002). One crucial phytohormone is auxin which recruits the AUX/IAAs transcriptional repressors to an SCF[TIR1AFBs] – E3 ligase (Tan et al., 2007). Auxin specifically acts as a molecular glue between one F-BOX proteins TRANSPORT INHIBITOR RESPONSE 1 (TIR1)/AUXIN F-BOX PROTEINS 1-5 (AFB1-5) and its ubiquitylation substrates AUX/IAA transcriptional repressors (Tan et al., 2007). Auxin sensing leads first to the polyubiquitylation of AUX/IAAs (Gray, Kepinski, Rouse, Leyser, & Estelle, 2001). Ubiquitylated AUX/IAAs are next recognized and internalized by the proteasome for degradation (Ramos, Zenser, Leyser, & Callis, 2001). AUX/IAAs degradation enables transcription of auxin

response genes by derepression of AUXIN RESPONSE FACTORS (ARFs) (Tiwari, Wang, Hagen, & Guilfoyle, 2001). Auxin-driven interaction of AUX/IAAs with TIR1/AFBs occurs mainly by a conserved degron motif which serves therefore as a degradation signal for ubiquitin mediated-proteolysis of AUX/IAAs. In the model plant *Arabidopsis*, 23-degron containing AUX/IAAs and 6 TIR1/AFBs have combinatorial potential of more than hundred auxin receptors that respond to varying intracellular levels of auxin (Calderón Villalobos et al., 2012).

Disruption of normal auxin sensing is detrimental for normal plant growth and morphology. *Arabidopsis* mutant plants carrying stabilized versions of AUX/IAAs *a.k.a* gain-of-function mutations show abnormal growth phenotypes due to constitutive repression of ARFs (Overvoorde et al., 2005). Gain-of-function AUX/IAAs carry single amino acid exchange mutations at the degron motif which prevent their binding with SCF$^{TIR1/AFB1-5}$ turning into constitutive transcriptional repressors. For example, *At*IAA3 (*short hypocotyl 2*, *shy2*) constitutive repression activity causes enlarged cotyledons, short hypocotyls, reduced lateral root growth, slowed gravitropic responses and decreased auxin-regulated gene expression  (Tian, Nagpal, & Reed, 2003; Tian, Uhlir, & Reed, 2002). The gain-of-function of *At*IAA7 (*auxin-resistant 2-1*, *axr2-1*) causes gravitropic defects in roots, hypocotyls and inflorescences (Nagpal et al., 2000; Timpte, Wilson, & Estelle, 1994). *At*IAA8 gain-of-function plants show more lateral branches than wild-type and short primary inflorescence stems, decreased shoot apical dominance, curled leaves and abnormal flower organs (short petal and stamen, and bent stigmas) (J. Wang, Yan, Yuan, Gao, & Lu, 2013). *At*IAA12 (*BODENLOS*, *BDL*) gain-of-function shows several embryonic defects (T. Hamann, Benkova, Bäurle, Kientz, & Jürgens, 2002). *At*IAA14 (*solitary-root 1*, *slr-1*) gain-of-function lacks lateral roots (Fukaki, Tameda, Masuda, & Tasaka, 2002). *At*IAA19 (*MASSUGU2*, *msg2*) gain-of-function displays neither hypocotyl gravitropism nor phototropism, and is defective in lateral root formation (Tatematsu et al., 2004). Similarly, the loss-of-function of TIR1 (*tir1-1*) is deficient in hypocotyl elongation and lateral root formation (Ruegger et al., 1998).

*In vitro* binding affinity studies showed that ASK1·TIR1 complex alone binds auxin in low affinity with a binding dissociation constant ($K_d$) of 13.4 μM (Cao et al., 2022). AUX/IAAs alone do not show any detectable auxin binding (Cao et al., 2022). Biologically relevant auxin sensing occurs when TIR1/AFBs interact directly with AUX/IAAs. Binding affinity for auxin was determined to be between 10-272 nM depending on *At*TIR1/AFBs and *At*AUX/IAAs combination *in vitro* (Calderón Villalobos et al., 2012; Niemeyer et al., 2020). The TIR1 structure shows a leucine-rich-repeat (LRR) domain with 18 LRR. Each LRR consists of a β-strand followed by a α-helix that ensemble into a solenoid structure with an overall horseshoe-like shape (Tan et al., 2007). The LRR-12 to

LRR-16 and the LRR-2 form the auxin binding pocket, a highly concave surface where auxin sits (**Figure 5A, B**). The crystal structure of ASK1·TIR1·auxin·*At*IAA7-degron shows that auxin is locked into TIR1's auxin binding pocket by AUX/IAA protein's GWPPV core degron motif (Tan et al., 2007) (**Figure 5A)**.

Importantly, *in vitro* and *in vivo* screens for auxin binding affinity showed that *At*AUX/IAAs with identical degron motifs possess different affinities to auxin (Calderón Villalobos et al., 2012; Shimizu-Mitao & Kakimoto, 2014). This prompted the hypothesis that *At*AUX/IAAs regions outside the degron motif increase or diminish auxin binding affinity expanding the dynamic range of auxin sensitivities *in vivo* (Calderón Villalobos et al., 2012). However, given the fact that degron flanking regions are IDRs, the structural advances in understanding how these regions precisely influence auxin perception came more recently and will be discussed in the following sections.
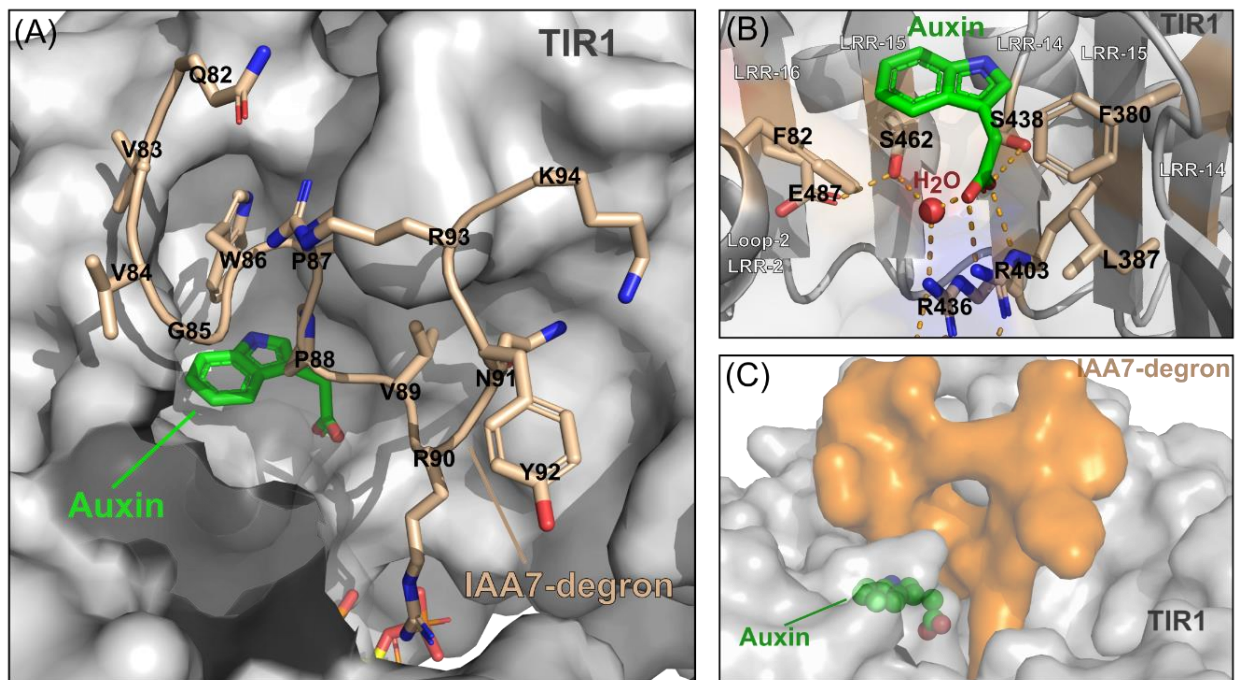


**Figure 5. Molecular mechanism of auxin perception by X-ray crystallography.** (A) Auxin fits into a hydrophobic cavity in TIR1's auxin binding pocket and is locked into the pocket by IAA7-degron. IAA7-degron residues W86, P87 and P87 contact auxin while the rest of residues establish multiple interactions with TIR1's binding pocket and surroundings. (B) At the binding pocket floor auxin establishes hydrogen-bond and salt-bridges with a single water molecule and TIR1's residues R403 and S483. (C) Surface representation shows auxin at the bottom of TIR1's binding pocket and locked by IAA7-degron. Models were built in pymol using as reference Tan et al., 2020.

## 1.6.1 IDRs interconnect modularly built AUX/IAAs

AUX/IAAs are built in a modular fashion with four functional and conserved domains spaced by IDRs with variable length and amino acid composition (Abel, Nguyen, & Theologis, 1995). Sequence alignment coupled with molecular and biochemical studies show that canonical AUX/IAA proteins carry at least four conserved and functional domains: ethylene-responsive element binding factor-associated amphiphilic repression (EAR), KR, degron and Phox/Bem1 (PB1) (Abel et al., 1995; Abel & Theologis, 1996; Hagen & Guilfoyle, 2002; Luo, Zhou, & Zhang, 2018). The region upstream the degron, outside the KR and EAR motif, are highly divergent in amino acid composition and its function beside a linker is unknown so far. The KR motif, consisting of a lysine and an arginine, is a nuclear localization signal (NLS) which has been additionally linked to the degradation rate of AUX/IAAs base in mutational analysis in transgenic plants *in vivo* and AUX/IAAs stability assays in yeast (Abel et al., 1995; Dreher et al., 2006; B. L. Moss et al., 2015). The EAR is located close to the end of the N-terminal region and consist of the consensus sequence LxLxLx, which recruits TOPLESS/TOPLESS-RELATED1-4 (TPL/TPR1-4) corepressor (Szemenyei, Hannon, & Long, 2008). Downstream the degron a variable region called the degron tail connects to the conserved Phox/Bem1 (PB1) folded domain located at the C-terminal. The PB1 domain exhibits a ubiquitin-like β-grasp fold, with five β-sheets and two α-helices (Dinesh et al., 2015; Y. Kim et al., 2020; Mutte & Weijers, 2020). The PB1 domain is necessary for AUX/IAAs homo- and hetero-oligomerization with ARF (Dinesh et al., 2015; Y. Kim et al., 2020). Circular dichroism (CD) spectroscopy analysis of *At*IAA7 and *At*IAA12 showed that the N-terminal region containing the EAR, degron and degron tail are IDRs (Niemeyer et al., 2020). Although regions outside the degron motif do not directly sense auxin, they in fact influence the binding affinity for auxin. Experiments were the degron tail and PB1 domain sequence in *At*IAA7 were swapped for those of *At*IAA12 caused 2-fold decrease in the auxin binding affinity of IAA7 chimeras compared to the *At*IAA7 wild-type (Niemeyer et al., 2020). Moreover, it was shown that an in-frame deletion of *Sisymbirum orientale* (*Os*) IAA2 which deletes its degron tail reduced *Os*IAA2 binding affinity towards *At*TIR1 and *At*AFB5 (Figueiredo et al., 2022). Thus, auxin binding affinity by AUX/IAAs may depend on the neighboring IDRs flanking the degron as they may enhance or diminish the association with TIR1/AFBs. Most of AUX/IAA proteins carry all functional four domains and IDR linkers connecting these domains are responsible for most of the amino acid sequence divergence among the AUX/IAA family. Differences in domains architecture are proposed to add alternative functions to AUX/IAAs.

## 1.6.2 Functional implications of intrinsic disorder for auxin perception

Structural proteomics analyses using cross-linking mass spectrometry (XL-MS) showed for the first time how full-length AUX/IAAs ensemble into the auxin receptor complex. Specifically, *At*IAA7 and *At*IAA12 IDRs and PB1 were shown to bind to the edges of TIR1's top surface while the degron, in between these regions, lock auxin into TIR1's pocket (Niemeyer et al., 2020). At the IDR site, the KR dipeptide motif has been proposed to bind to TIR1's cluster II corresponding to LRR17–18 (481–529 amino acids) based on XL-MS data. On an opposite side, the PB1 domain contacts TIR1's cluster I at LRR3-7 (140–229 amino acids) (Niemeyer et al., 2020) (**Figure 6**). These results pointed out how regions outside and distant from the degron motif interact with TIR1. Furthermore, chimera versions of *At*IAA7 and *At*IAA12 where their respective PB1 and degron flanking region were swapped showed that these regions may allosterically diminish or enhance direct auxin binding by the respective TIR1·*At*IAA7 and TIR1·*At*IAA12 complexes (Niemeyer et al., 2020). Since the degron is the only interface of AUX/IAAs that contact auxin based on the crystal structure, the allosteric effect in auxin binding is assumed to come from PB1 and degron flanking regions. For example, IDRs and PB1 of AUX/IAAs may bind strongly to TIR1 independently of auxin, making a pre-ensemble complex readable for capturing auxin. On the contrary, IDRs and PB1 that bind weakly to TIR1 will result in a weak TIR1 and AUX/IAA association, and therefore a low auxin affinity. However, quantitative data that measures the contribution of IDRs and PB1 to TIR1 binding is still missing.

Recent work with *At*IAA17 shows that its N-terminal IDR has a propensity to secondary structural elements (Ramans-Harborough et al., 2023). Coupling the NMR spectroscopy results with coarse-grained (CG) *in silico* modeling the authors found that *At*IAA17 has preferentially two conformers in the free state were 13.2% of the sequence forms helices, 41.6% extended regions and the remaining 46% of the sequence may form coils or a low proportion of β-sheets. Moreover, Ramans-Harborough et al., (2023) shows different secondary structure conformation in *At*IAA17 may form when binding to TIR1. However, no quantitative data describes the contribution of the N-terminal *At*IAA17 side for TIR1 binding.
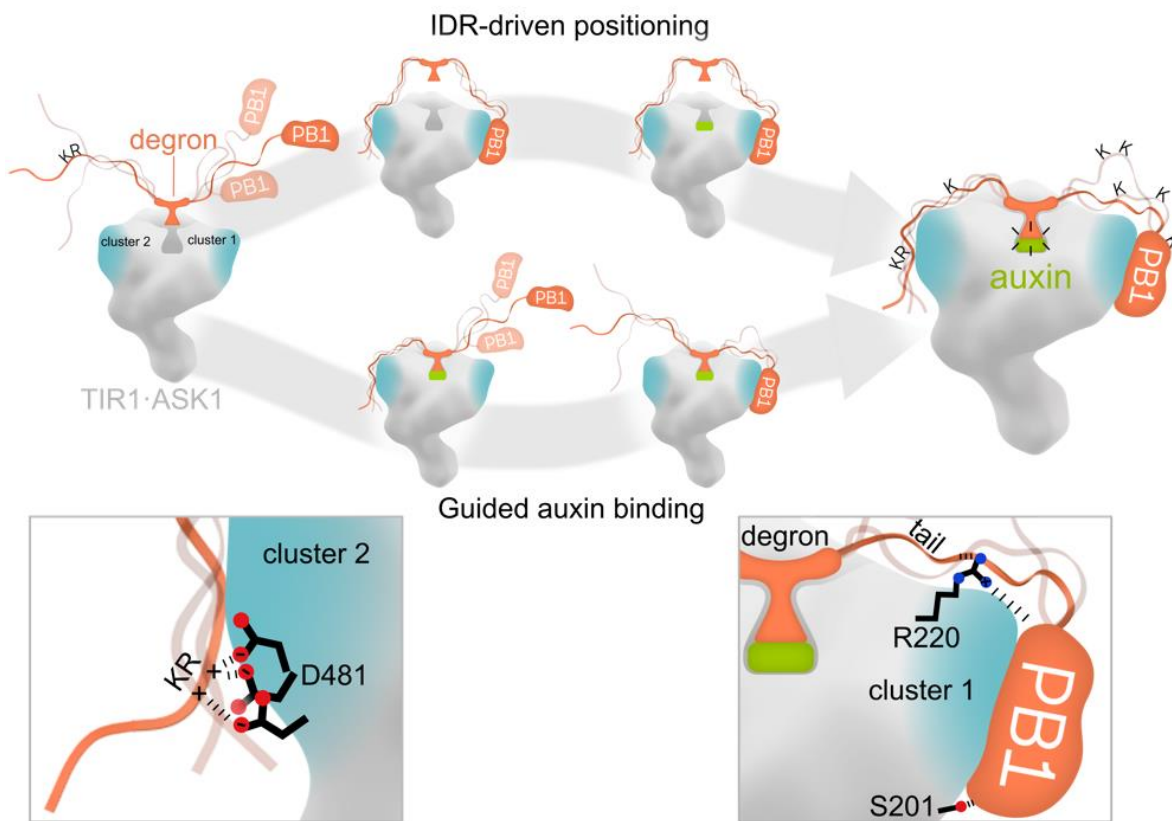


**Figure 6. Proposed binding mechanism for auxin receptor complex formation with full-length AUX/IAAs by Niemeyer et al., (2020).** IDRs flanking the degron assist in the positioning of the PB1 at cluster I and the KR motif at cluster II. In the IDR-driven positioning pathway (top arrow), AUX/IAAs initially bind to TIR1's clusters in an auxin independent manner. In the guided auxin binding (bottom arrow), AUX/IAAs recruitment to TIR1 is initiated through the degron by auxin. In the fully engage receptor complex, AUX/IAAs cover TIR1's top surface securing auxin into TIR1's auxin binding pocket. Lysine residues which will undergo ubiquitylation are exposed to the solution. At cluster 2, TIR1 residue D481 establishes salt bridges with AUX/IAA's KR motif and cluster 1 TIR1s residues R220 and S201 bind AUX/IAA's PB1 domain. Taken from Niemeyer et al., 2020

# 1.7 AUX/IAA proteins sequence carries multiple binding modes for transcriptional regulation and auxin sensing functions

This section aims to conceptually categorize the binding modes of AUX/IAAs IDRs based on existing literature and solved structures featuring AUX/IAAs domains. This seeks to understand how AUX/IAAs interact with multiple binding partners exerting a dual function as transcriptional repressors and part of the auxin receptor complex. We hypothesize that structural plasticity in AUX/IAAs proteins, specifically in their IDR sequence allows such dual role *in vivo*.

## 1.7.1 A disorder-to-order binding mode at AUX/IAAs degron locks auxin into TIR1's auxin binding pocket

Based in X-ray crystallography, CD and NMR studies AUX/IAAs, the degron motif is located in a IDR that folds into a stable coil conformation for auxin binding with TIR1 (Niemeyer et al., 2020; Ramans-Harborough et al., 2023; Tan et al., 2007). Therefore, AUX/IAA's degron can be classified as 13-residue long ι-MoRF as it acquires an irregular, yet stable structure when binds to TIR1 and auxin. Moreover, nuclear magnetic resonance (NMR) studies showed that the W-P peptide bond in the core sequence GWPPV spontaneously undergoes a *cis/trans* isomerization *in vitro* (Ramans-Harborough et al., 2023). Effective binding of *At*IAA17 and ASK1·TIR1 driven by auxin occurs with the *cis* isomer while the *trans* isomer showed reduced TIR1-binding by NMR (Ramans-Harborough et al., 2023). Hence, stabilization of the degron motif via disorder-to-order transition requires a *cis* degron configuration.

## 1.7.2 EAR motif mediates AUX/IAAs and TOPLESS interaction via disorder-to-order transition

The EAR motif of *At*AUX/IAA is also located as well in a predicted IDR and mediates TPL/TPR interaction (Niemeyer et al., 2020; Tiwari, Hagen, & Guilfoyle, 2004). TPL/TPR function is essential for normal plant growth as TPL/TPR mutants show defects in the formation of roots and shoots during embryonic states (Jeff A. Long, Ohno, Smith, & Meyerowitz, 2006; J. A. Long, Woody, Poethig, Meyerowitz, & Barton, 2002). TPL/TPR interaction with AUX/IAAs is exerted by the N-terminal region at the LIS1 homology (LisH) and a C-terminal to LisH (CTLH) domain (Szemenyei et al., 2008). Truncation of the EAR motif of *At*IAA3, *At*IAA6 and *At*IAA19 resulted in almost complete loss of their repression activity *in vivo* (Tiwari, Hagen, & Guilfoyle, 2003; Tiwari et al., 2004; Tiwari et al., 2001). This indicates that the EAR motif is essential for AUX/IAAs repression function. The crystal structure of *At*TPL·*At*IAA27^EAR (**Figure 7**) and *Oryza sativa* (*Os*)TPR2·*At*IAA1^EAR shows *At*IAA27^EAR and *At*IAA1^EAR adopt a single coiled conformation in the

bound state (Martin-Arevalillo et al., 2017). This interaction is energetically supported by hydrophobic residues within the EAR motif and TPL groove 3 hydrophobic residues (Martin-Arevalillo et al., 2017). Additional ionic interactions of the EAR with TPL/TPR support the $At$TPL·$At$IAA27$^{EAR}$ and OsTPR2·$At$IAA21$^{EAR}$ binding (Martin-Arevalillo et al., 2017). Similarly, $At$IAA1$^{EAR}$ and $At$IAA10$^{EAR}$ share a common mode of interaction with $Os$TPR2. This is mediated by hydrophobic interactions between three conserved leucine residues in the EAR motif and highly conserved hydrophobic residues at TPL groove 3 of $Os$TPR2 (Ke et al., 2015). Both, $At$IAA1$^{EAR}$ and $At$IAA10$^{EAR}$ form a stable coiled conformation in the $Os$TPR2 bound state (Ke et al., 2015). These results allow to classify the AUX/IAA EAR as a nine residue long SLiMs which bind to TPL/TPR via disorder-to-order transition (Korasick, Enders, & Strader, 2013; van der Lee et al., 2014). AUX/IAAs therefore integrate auxin sensing and EAR repression functions through their IDRs regions that fold upon binding.

### 1.7.3 PB1-PB1 structural complementary mediates AUX/IAAs transcriptional repression function at the C-terminal

At the C-terminal PB1 domain, AUX/IAAs homo- and hetero-oligomerize within themselves and with ARFs, respectively, for repression of ARF transcriptional activity (Guilfoyle, 2015). In the Arabidopsis genome twenty-two (22) ARFs have been identified (Boer et al., 2014; Guilfoyle, 2015). Most ARFs have three conserved domains. An N-terminal DNA-binding domain (DBD) which bind to auxin-responsive genes promotors (Freire-Rios et al., 2020; Tiwari et al., 2003); a middle IDR region which confers either transcriptional repression or activation functions and promotes formation of biomolecular condensates (Powers et al., 2019; Tiwari et al., 2003); and, a C-terminal PB1 domain for homo- and heterodimerization with AUX/IAAs and/or ARFs (Guilfoyle, 2015; Korasick et al., 2014; Tiwari et al., 2003).

In general, the first half of the PB1 domain contains a positively charged face, while the other second half represents a negatively charged face (Guilfoyle, 2015; Korasick et al., 2014). At the negative face the consensus sequence D-x-D/E-x-D/E is also referred to as the OPCA motif (Guilfoyle, 2015; Korasick et al., 2014). The crystal structure of $At$ARF5$^{PB1}$·$At$IAA17$^{PB1}$ complex, shows two structurally complementary positive and negative interfaces which bind via a salt-bridge network (Y. Kim et al., 2020). Collectively, four positively charged residues of IAA17 participate in the formation of salt bridges with negatively charged residues of ARF5 (**Figure 7**) (Sun H. Kim et al., 2022). The nuclear magnetic resonance (NMR) solution structure of *Pisum sativum* (*Ps*) IAA4$^{PB1}$ showed a basic patch with K96, K107 and R106, and an acid patch with D151, D153, D155 and D161 on opposite faces (Dinesh et al., 2015). IAA4$^{PB1}$ oligomerizes by a

salt-bridge network between the acid and basic patches in a similar fashion as ARF5$^{PB1}$·IAA17$^{PB1}$ complex (Dinesh et al., 2015).
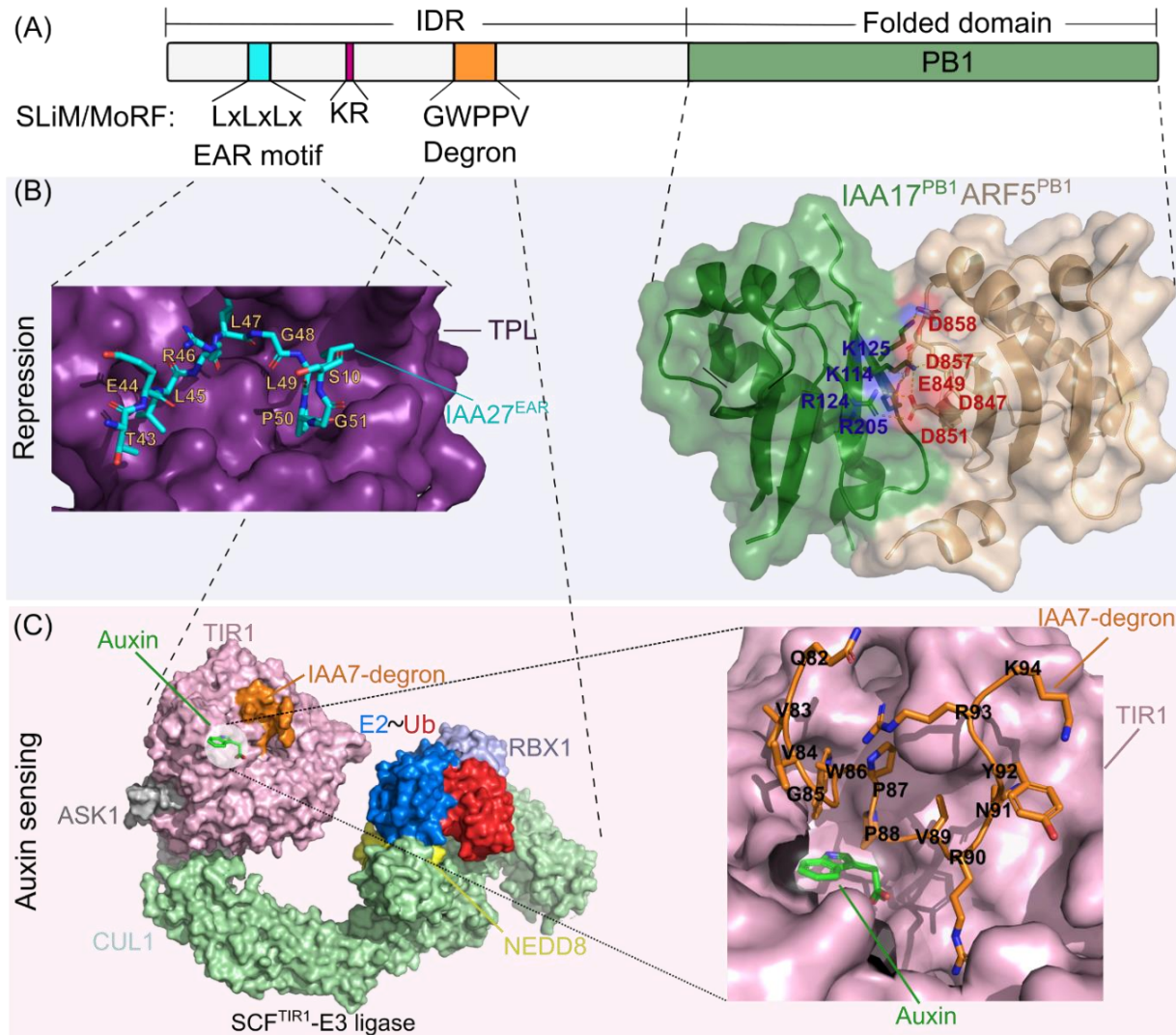


**Figure 7. Canonical AUX/IAAs architecture and its interaction binding modes.** (A) Canonical AUX/IAA proteins carry an EAR, KR and a degron motif located in an IDR, while the C-terminal PB1 domain is a folded domain. Both EAR and degron motifs undergo disorder-to-order transitions when bound to their targets. (B, left) Interaction of TPL and IAA27$^{EAR}$ (PDB: 5NQV). The IAA27$^{EAR}$ shows a stable conformation in the bound state with not secondary structure shown by X-ray crystallography. (B, right) Interaction of IAA17$^{PB1}$ and ARF5$^{PB1}$, both proteins surfaces carry complementary interfaces which bind via electrostatic interactions network (PDB: 6L5K). (C) Auxin sensing by a SCF$^{TIR}$-E3 ligase. The IAA7-degron shows a stable conformation in the TIR1-bound state, securing auxin into TIR's auxin binding pocket (PDB: 2P1Q, 6TT4).

From the structural point of view, the binding mode of PB1-PB1 follows the traditional folded structural/function paradigm where structural complementary promote the protein-ligand interaction, and therefore the domain function (van der Lee et al., 2014). It is important to note that in many AUX/IAAs the PB1 domain represents on average ~50% of the total sequence, and its interaction is limited to PB1·PB1. However, through small binding motifs IDRs in AUX/IAAs increase their regulatory functions through the EAR, KR and degron motifs. This highlights the important role of IDRs for AUX/IAAs dual function *in vivo.*

### 1.7.3.1 Specificity of PB1 mediated AUX/IAAs and ARFs interaction *in vivo*:

AUX/IAAs specificity towards ARFs it is proposed to depend on the their developmental expression pattern (Weijers et al., 2005). This means for AUX/IAAs to repress ARFs activity they must co-localize in the same kind of cell, during the same developmental stage. Typically, genetic studies with AUX/IAAs gain-of-function showed a similar phenotype as the loss-of-function of ARFs, hinting to overlapping regulatory role for plant growth. A classic example is the loss-of-function of *At*ARF5 (*MONOPTEROS*) and the gain-of-function of *At*IAA12 (*BODENLOS*) where both mutant plants showed altered hypophysis formation and orientation of the division plane of the apical daughter of the zygote, resulting in double-octant proembryos (Berleth & Jürgens, 1993; T. Hamann et al., 2002; Thorsten Hamann, Mayer, & Jürgens, 1999). This suggested that *At*ARF5 and *At*IAA12 act in the same developmental pathway, and their interaction was proven by other *in vivo* and *in vitro* (T. Hamann et al., 2002). Furthermore, it was shown that *At*IAA12 repress *At*ARF5 activity specifically for the control of the embryonic root formation (Weijers et al., 2005). *In vivo* data has also shown that *At*IAA3 and *At*IAA19 repress *At*ARF7 and *At*ARF19 activity specifically for the regulation of gravitropic root growth and lateral root formation (Chapman & Estelle, 2009; Weijers et al., 2005).

## 1.8 Synergistic features of AUX/IAA IDRs prompt their ubiquitylation and turnover

AUX/IAAs half-lives range between 6 to 80 min (Abel et al., 1995). Variations in AUX/IAAs degradation rate are attributed to their auxin binding affinity and variability within the IDRs flaking the degron which changes their processivity by the ubiquitin proteasome system (UPS) (Calderón Villalobos et al., 2012; Dreher et al., 2006; Havens et al., 2012; Ramos et al., 2001). AUX/IAA proteins sequence carry a tripartite degron consisting of: 1) an E3 ligase recognition site (degron); 2) ubiquitylation sites; and 3) IDRs for initiation of proteasomal degradation (Guharoy, Bhowmick, Sallam, & Tompa, 2016). While the degron mediates the interaction with SCF[TIR1/AFBs] driven by auxin, the IDRs flanking the degron will expose the lysine residues for ubiquitylation. Additionally,

most of AUX/IAAs carry IDRs >50 residues at the N-terminal region which has been established as a requirements for efficient proteasomal engagement with other synthetic substrates *in vivo* and *in vitro* (Niemeyer et al., 2020; Tomita & Matouschek, 2019).

*In vitro* reconstitution of the ubiquitylation cascade coupled with mass spectrometry experiments identified putative ubiquitylation sites in *At*IAA6, *At*IAA7, *At*IAA12 and *At*IAA19 bringing us closer to understand how this process occurs *in vivo* (**Figure 8**) (Niemeyer et al., 2020; Winkler et al., 2017). Ubiquitylation sites occur in lysine residues, preferentially within IDRs flanking the degron motif and but are also detected at the PB1 (**Figure 8**) (Niemeyer et al., 2020; Winkler et al., 2017). Although it is commonly hypothesized that flexible IDRs in AUX/IAA facilitate their ubiquitylation, the exact structural mechanism that explains the location of AUX/IAAs ubiquitylation sites is still unknown. For *At*IAA6, *At*IAA7, *At*IAA12 and *At*IAA19 *in vitro* ubiquitylation occurs rapidly and is detectable at 5-10 min (Niemeyer et al., 2020; Winkler et al., 2017). Differences in AUX/IAAs ubiquitylation dynamics have been attributed to the auxin binding affinities of the respective TIR1/AFBs·AUX/IAA receptor complex (Niemeyer et al., 2020). For instance, *in vitro* ubiquitylation of *At*IAA7 by an SCF$^{TIR1}$ occurs more rapidly that of *At*IAA12 due to a TIR1·*At*IAA7 (auxin $K_d$ = 17 nM ±7.81) higher auxin binding affinity compared to that of TIR1·*At*IAA12 (auxin $K_d$ = 270 nM±54.09) (Calderón Villalobos et al., 2012).

Reconstitution of the auxin signaling pathway in yeast has permitted to obtain a glimpse of auxin induced degradation dynamics of *At*AUX/IAAs (Havens et al., 2012; B. L. Moss et al., 2015). Here, by heterologous expression of *At*TIR1/AFBs and *At*AUX/IAAs tagged with yellow florescence protein (YFP) in yeast treated with auxin, AUX/IAAs half-lives were assed (Havens et al., 2012; B. L. Moss et al., 2015). Removal of the conserved PB1 domain caused a modest acceleration of *At*IAA1, *At*IAA17 and *At*IAA28 degradation rate compared to the full-length protein (B. L. Moss et al., 2015). However, an amino acid exchange at the KR motif by AA in *At*IAA17 caused a three-fold increase in the half-life (B. L. Moss et al., 2015). Similarly, for *At*IAA1 a KR→AA amino acid exchange cause a ~two-fold increase in its half-life (B. L. Moss et al., 2015). The half-life of IAA17 was also increased from 8.8 min to 28.2 min in *Arabidopsis* plants by introducing a KR→QQ mutation (Dreher et al., 2006). These results demonstrate that the IDR region through the KR motif negatively influences AUX/IAAs half-life.
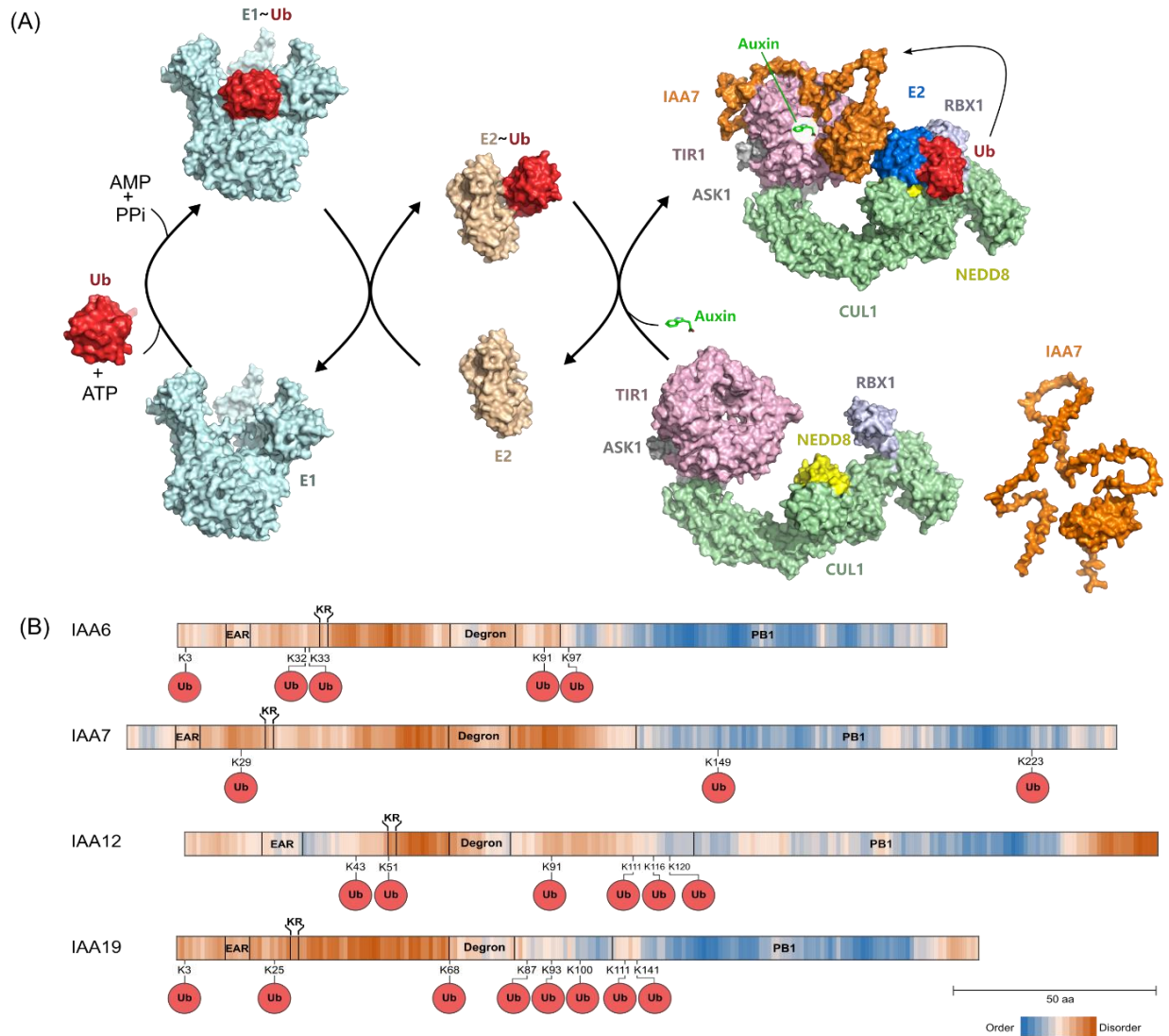
**Figure 8.** *In vitro* **reconstitution of the ubiquitylation cascade shows ubiquitylation sites in AUX/IAAs.**(A) Ubiquitylation cascade includes a three-step enzymatic cascade: (1) an E1 (PDB: 6DC6) adenylate Ub (PDB: 1UBQ) to form a high-energy thioester bond between the Ub C-terminal carboxyl group and the thiol group of the active site cysteine residue; (2) The activated Ub is transferred to the cysteine residue of an E2 (PDB: 3A33) enzyme through a thioester linkage; (3) an E3 ligase (PDB: 6TTU, 2P1Q) recruits a charged E2 to transfer Ub to AUX/IAAs (IAA7, Alphafold: AF-Q38825-F1) in the presence of auxin. (B) *In vitro* ubiquitylation sites of AUX/IAAs preferentially occur within the N-terminal IDRs that flank the degron motif while ubiquitylation at the PB1 is less common.

## 1.9 AUX/IAAs protein family expanded in land plants

Examining the evolution of AUX/IAAs has deepened our comprehension of alterations in the complexity of the auxin signaling pathway. Genome wide-analysis have identified AUX/IAA proteins in all major land plant groups (Luo et al., 2018; Paponov et al., 2009; Wu et al., 2017). AUX/IAA protein evolution spans 450-530 million years ago (MYA) appearing for the first time in bryophytes (Kato, Nishihama, Weijers, & Kohchi, 2018; Mutte et al., 2018). Early land plants only contain a small pool of AUX/IAA proteins, for example the bryophytes *Marchantia polymorpha* and *Physcomitrium patens* only contain one and three AUX/IAA proteins, respectively (Kato et al., 2018; Luo et al., 2018; Paponov et al., 2009; Wu et al., 2017). Nevertheless, AUX/IAAs underwent a progressive diversification in higher plants, a process called radiation, by segmental and/or tandem genome duplication (Paponov et al., 2009) (**Figure 9**). In fact, in the angiosperms *Arabidopsis thaliana* and *Glycine max,* 76% and 90% of AUX/IAA genes were segmentally duplicated, respectively (Luo et al., 2018; Wu et al., 2017). Together, these processes led to a tremendous increase in the number of AUX/IAA proteins in flowering plants (Luo et al., 2018; Wu et al., 2017). To date, in the angiosperm group, 29 AUX/IAA genes have been identified in *Arabidopsis thaliana*, 55 in *Brassica rapa*, 26 in Citrus, 26 in *Eucalyptus grandis*, 26 in *Solanum lycopersicum*, 26 in *Vitis vinifera* and 35 in *Populous trichocarpa* (Wu et al., 2017). Since AUX/IAAs are central in auxin response, this increase in diversity points out towards an increase complexity of the auxin signaling pathway in higher plants (Paponov et al., 2009). It is proposed that changes in the cellular expression pattern contribute to AUX/IAA neofunctionalization leading to plant adaptation to environmental changes (Paponov et al., 2009; Wu et al., 2017). Furthermore, at a sequence level, AUX/IAAs conserved domains are connected by linker regions that vary drastically in sequence length across land plant species. Currently, no study has focused in evaluating how the length of these linker regions varies across AUX/IAAs of different species. Moreover, it is also unknown how intrinsic disorder differs across land plants.

| | Bryophytes | | Lycophytes | Ferns | Gymnosperms | Angiosperms | |
|---|---|---|---|---|---|---|---|
| | *Marchantia polymorpha* | *Physcomitrium patens* | *Selaginella moellendorffii* | *Azolla filiculoides* | *Picea abies* | *Oryza sativa* | *Arabidopsis thaliana* |
| AUX/IAAs: | 1 | 3 | 7 | 9 | 18 | 32 | 29 |
| TIR1/AFBs: | 1 | 4 | 2 | 3 | ? | 5 | 6 |
| ARFs: | 3 | 17 | 10 | 9 | 8 | 25 | 22 |

~470 MYA — ~410 MYA — 360 MYA — 300 MYA — 150 MYA

Embryo / Multicelular diploid sporophyte / 3D pattering

Vasculature / Dominant sporophyte / Control of shoot development

Seed evolution / Floral homeotic genes

Seeds / Pollen

**Plant's complexity**

**Figure 9. The increase in land plant's complexity was accompanied by an expansion of the auxin signaling pathway components.** The number of AUX/IAAs, TIR1/AFBs and ARFs are shown for representative members of the main land plant groups. The plant's complexity is relative to the number of added growth and developmental processes which are absent in early colonizing land plants (Banks et al., 2011; Boer et al., 2014; de Vries et al., 2016; Guilfoyle, 2015; Shen et al., 2010; Su et al., 2023).

## 1.10 Biotechnological applications of the auxin signaling pathway

The scientific importance of deciphering the molecular mechanisms auxin driven protein-protein interaction transcends the plant field borders and reaches the medical field. The solved structure of the auxin receptor introduced for the first time a molecular glue system, where two proteins have a weak interaction with each other which is greatly enhanced by a small molecule (Calderón Villalobos et al., 2012; Tan et al., 2007; Winkler et al., 2017). Moreover, this interaction leads to selective proteolysis of protein targets *in vivo* controlling protein stability (Dreher et al., 2006; Britney L. Moss et al., 2015; Ramos et al., 2001). Since many diseases such as Alzheimer's disease, Parkinson's disease, amyotrophic lateral sclerosis (ALS), Huntington's disease, dementia with Lewy bodies, frontotemporal diseases, and multiple system atrophy, occurs due to an overaccumulation of proteins (Soto & Pritzkow, 2018), the auxin perception system is an attractive model to recreate in order to induce selective target proteolysis by small molecules (Cao et al., 2022; Frere, de Araujo, & Gunning, 2022). A similar principle applies to immunomodulatory drugs such lenalidomide and pomalidomide and antitumor aryl-sulfonamides which promotes E3 – ligases interaction with specific protein targets  (Matyskiela et al., 2020; Petzold, Fischer, &

Thomä, 2016). For instance, lenalidomide causes selective degradation of IKZF1 and IKZF3 by a CRBN-CRL4 ubiquitin ligase in multiple myeloma cells, inhibiting cell growth (Krönke et al., 2014). Recent efforts in the molecular conceptualization of different molecular glues system including the auxin sensing system, seeks to extract the biochemical principles of different molecular glues systems in order to rationally design molecular glues for targeted proteolysis (Cao et al., 2022). Additionally, the auxin-inducible degron (AID) system was developed and it is used in the cancer research field to deplete *in vivo* protein targets which are co-expressed as tagged versions with AUX/IAA's degron and with TIR1 (Nishimura, Fukagawa, Takisawa, Kakimoto, & Kanemaki, 2009; Yesbolatova et al., 2020). Since auxin is harmless to human cells it can be exogenous applied to induce protein depletion and study the effect of a specific protein target degradation *e.g.* in cancer (Nishimura et al., 2009; Yesbolatova et al., 2020).

## 1.11 Structural approaches used in the study AUX/IAAs binding modes and conformational ensembles

Structural fluctuations in IDRs make it difficult to visualize their conformational ensemble by a single structural technique. Missing structural information about IDRs hinders the possibility of establishing a proper ensemble/function relationship neglecting additional IDRs roles (e.g. IDRs linker functions). Structural techniques, for example, vary in time- and length- scales sensitivities and IDRs properties may show a broad range of time-dependent behaviors. For example, NMR, X-ray scattering and single molecule Förster resonance energy transfer (smFRET) access to IDRs structural fluctuations over a wide range of length and time-scales which spanning from nanoseconds (10-9 s) to seconds (100 s) scales (Chance, Farquhar, Yang, Lodowski, & Kiselar, 2020; Evans, Ramisetty, Kulkarni, & Weninger, 2023). While X-ray, cryo-electron microscopy and XL-MS provide access to static snapshots across longer length scales accessing only to one or few conformations (Evans et al., 2023). Additionally, biophysical methods have different size requirements ranging for example from: >10 kDa small angle X-ray scattering (SAXS), <100 kDa NMR, and >100 kDa cryogenic electron microscopy (cryo-EM) (Chance et al., 2020). Techniques resolution may also show limits ranging from ~3 Å (NMR, X-ray crystallography, cryo-EM) to >20 Å (SAXS). Additionally, methods such as NMR require a high protein concentration which could be a limitation for proteins with aggregation propensity (Yee, Semesi, Garcia, & Arrowsmith, 2014). Label-based methods such smFRET require covalent modification of protein with fluorescent dyes, making necessary the application of alternative methods (typically, computational) to prove that such covalent modifications do not affect the results (Toseland,

2013). Overall, techniques selection should reveal different aspects of IDRs behaviors enabling them to outline a complete picture of their ensemble/function relationship.

In the case of AUX/IAAs, several structural techniques were used in the past to visualize the binding mode of single domains (**Figure 7, Figure 10**). The X-ray crystallography on *At*IAA7-degron and several AUX/IAAs-EAR revealed their binding mode for TIR1 and TPL/TPR interactions, respectively (Ke et al., 2015; Martin-Arevalillo et al., 2017; Tan et al., 2007). Moreover, NMR solution structures of *Ps*IAA4[PB1] and *At*IAA17 showed the binding mechanism of AUX/IAAs at the PB1 (Dinesh et al., 2015; Han et al., 2014). NMR studies with *At*IAA17 N-terminal region showed the importance of the *cis/trans* isomerization for AUX/IAAs degron function in auxin sensing (Ramans-Harborough et al., 2023). Despite the gain in structural knowledge from all these approaches, a global picture of how AUX/IAAs interconnect repression and auxin sensing functions simultaneously is still missing. Niemeyer et al., (2020) used for the first-time full-length AUX/IAAs and proved that they are disordered at the N-terminal region. Furthermore, by using XL-MS and protein docking coupled with molecular dynamic simulations they showed that *At*IAA7 and *At*IAA12 bind the top surface of TIR1 (Niemeyer et al., 2020). While these approaches proved useful to describe an overall assembly of the auxin receptor complex, technical limitation failed to describe the complete conformational ensemble of AUX/IAAs during auxin perception. This dissertation seeks to broaden our structural understanding of full-length AUX/IAAs ensembles during auxin perception. This will bring us closer to mechanistically understanding the role IDRs for auxin receptor complex formation and the way that AUX/IAAs are ubiquitylated. To accomplish this, we used biophysical and computational techniques such as light scattering, SAXS, smFRET, XL-MS/MS and coarse-grain (CG) modeling that allow to describe the conformational ensemble of AUX/IAAs when they bind to TIR1 during auxin perception (**Figure 10**).

**NMR**
-Solution structure of *Ps*IAA4[PB1], *At*IAA17[PB1] and *At*IAA17[PB1]·*At*ARF5[PB1].
-PB1 binding mode
-Proposed secondary strucutral model elements in IAA17[IDR]
-*cis/trans* isomerization of W-P at the degron motif
*Han et al., 2014, Dinesh et al., 2015, Kim et al., 2020, Ramans-Harborough et al., 2023*

High resolution techniques

**X-ray crystallography**
-Degron binding mode
-EAR binding mode
*Tan et al., 2007, Ke et al., 2015, Martin-Aervalillo et al., 2017*

Structural approaches applied to AUX/IAAs

**XL-MS, molecular dynamics and CD**
-Recognition of IDRs in AUX/IAAs
-Topology of auxin receptor complex
*Niemeyer et al., 2020; Harborough et al., 2023*

Low resolution/ensemble techniques

**smFRET, SAXS, light scattering, FCCS, CG-modeling**
-IDR lenght impact on AUX/IAAs ensemble
-Conformational ensemble of AUX/IAAs and auxin receptors
-Allosteric modulation of auxin receptors by IDRs and PB1
-Ensemble/function relationship of AUX/IAAs for binding and ubiquityation
*In this dissertation*

**Figure 10. Structural approaches applied to the study of AUX/IAAs interaction.** Previous structural approaches applied on AUX/IAAs provided a static view on the protein-protein interaction binding mode neglecting the function of IDRs linking regions in most cases. This dissertation seeks to describe the conformational ensemble of AUX/IAAs during auxin perception in order to establish a proper ensemble/function relationship for auxin sensing and ubiquitylation at their IDRs.

# 2. Hypothesis and objectives

AUX/IAA proteins integrate translational repression and auxin sensing functions through their IDR and PB1 domains by engaging in various protein-protein interactions through different binding modes. The solved crystal structure of the auxin receptor complex showed how IAA7-degron motif locks auxin into TIR1 auxin binding pocket by a single coiled conformation (Tan et al., 2007). While the IAA7-degron motif has a clear disorder-to-order binding mode. From the structural point of view, the binding mode of the rest of AUX/IAAs sequence at the IDR and the PB1 to the formation of the auxin receptor complex have remained elusive. XL-MS showed for the first time the complete auxin receptor complex topology where the IDRs flanking the degron and the PB1 cover the top surface of TIR1 (Niemeyer et al., 2020). Nevertheless, the model proposed by Niemeyer et al., (2020) may reflect only one or few ensembles of the AUX/IAAs on top of TIR1 given the XL-MS well-known limitations. The proposed model for example does not explain how ubiquitylation sites of AUX/IAAs are spread out throughout the primary sequence of AUX/IAAs (**Figure 8**). Specially, since in the model AUX/IAAs interaction with TIR1 are fixed at TIR1's cluster I and II (**Figure 6**). Hence, only the PB1 will be proximal enough to the active site of the SCF$^{TIR1}$-E3 ligase, yet ubiquitylation sites are also found at the IDR of IAA7. Furthermore, it was still unknown the binding contribution of residues outside the degron motif to the affinity between AUX/IAAs and TIR1/AFBs. Since AUX/IAAs are divergent in amino acid composition predominately at the IDR, IDRs may be responsible of how AUX/IAAs differentially associate with TIR1/AFBs. The solution to these fundamental questions from the protein structural biology perspective seeks to get us closer to understand how auxin receptor complexes specialized for the perception of different levels of auxin concentrations at a molecular level. This is highly relevant for the plant field, since auxin-driven transcriptional outputs start at the perception of auxin.

After Niemeyer et. al., (2020) I have handled the hypothesis that AUX/IAAs conformational ensemble changes from the free- to the TIR1-bound state. Furthermore, I hypothesized that this conformational change in AUX/IAAs may underlie functional roles for auxin receptor complex formation and AUX/IAAs ubiquitylation. Noting that in *Arabidopsis* there are 23-degron containing AUX/IAAs with variable IDRs and 6 TIR1/AFBs, the elucidation of the AUX/IAAs binding modes may help to understand the different sensitivities in auxin perception observed in plants. Additionally, the elucidation of AUX/IAAs binding mode may also explain why AUX/IAAs exhibit different ubiquitylation and degradation rates which ultimately guide plant growth and development. To test these hypotheses this dissertation seeks to answer the following questions:

a. How do IDRs in AUX/IAAs influence their conformational ensembles? The conformational ensemble of AUX/IAAs will be addressed by applying DLS/SLS and SAXS to selected members of the AUX/IAAs family of varying sequence length.

b. How is the AUX/IAAs conformational ensemble in the free and TIR1-bound state? This will be answered by applying smFRET to fluorescently labeled-IAA7 alone or in combination with auxin and/or ASK1·TIR1.

c. Do IDRs in AUX/IAAs influence the binding between ASK1·TIR1 and AUX/IAAs? Microscale thermophoresis (MST) assays will be used to determine the binding affinity between ASK1·TIR1 and IAA7 variants lacking either the KR motif or the PB1. Additionally, XL-MS and coarse-grain modeling will be used to describe the conformational ensemble of IAA1, IAA7, IAA12 and IAA27 which contrast in the IDR length and sequence composition.

d. Do IDRs influence AUX/IAAs polyubiquitylation by an SCF$^{TIR1}$-E3 ligase? *In vitro* reconstitution of the ubiquitylation (IVUs) cascade assays will be applied to determine ubiquitylation sites in IAA1 and IAA27 which possess IDRs of different lengths.

e. Do AUX/IAAs share a common binding mechanism across land plant species for auxin receptor complex formation? To address this question, we will perform a database search of AUX/IAA sequences across the seven major land plant groups. AUX/IAAs sequences will be analyzed *in silico* to extract sequences features that could hint towards different binding mechanisms for auxin receptor complex formation across different land plants.

# 3. Results

## 3.1 How do IDRs in AUX/IAAs influence their conformational ensembles?

### 3.1.1 IDRs length is inversely proportional to *At*AUX/IAAs compactness

*At*AUX/IAAs are relatively small plant proteins ($\bar{x}$ = 24.4 kDa±5.24, $\bar{x}$ = 219 amino acids±49.75 [$\bar{x}$±s.d., n=29]) with a dual function as transcriptional repressors and as part of the auxin receptor (Figueiredo & Strader, 2022; Luo et al., 2018; Nemhauser, 2018). To gain a better understanding of the AtAUX/IAAs ensemble/function relationship, I applied a combination of <u>d</u>ynamic <u>l</u>ight <u>s</u>cattering and <u>s</u>tatic <u>l</u>ight <u>s</u>cattering (DLS/SLS) on a subset of *At*AUX/IAAs that have IDRs of varying length. This approach will provide information on how IDRs length differences in *At*AUX/IAAs influence their compactness in their free state. DLS/SLS measurements were performed in collaboration with Dr. Anja Thalhammer and Dr. Martin Wolff from Potsdam University.

First, *At*AUX/IAAs were classified based in their total sequence length as: short (≤199 amino acids), medium (≥200-≤299 amino acids) and long (≥300 amino acids) (**Figure 11**). Next, we chose two representative *At*AUX/IAAs of each length group (as above) and recombinantly expressed and purified them. For the selection of *At*AUX/IAAs, we also considered the predicted AUX/IAAs IDR length published in Niemeyer et al., (2020). Of note, in order to prevent protein oligomerization and aggregation, which would reduce protein solubility in our assays, full length *At*AUX/IAA proteins were expressed as <u>b</u>asic patch <u>m</u>utant <u>3</u> (BM3) versions (Dinesh et al., 2015). We also recombinantly expressed the N-terminal IDR and the PB1 domain of IAA7 separately, which we correspondingly called IAA7$^{\Delta PB1}$ and IAA7$^{PB1}$. These two IAA7 variants were used as IDR and folded domain references of compactness, respectively. IAA7 has been extensively used for structural studies where the N-terminal region was proven to be an IDR and homology based-models have provided structural insights into its PB1 domain (Niemeyer et al., 2020; Tan et al., 2007). This makes IAA7 a suitable protein reference for structural studies among *At*AUX/IAA.
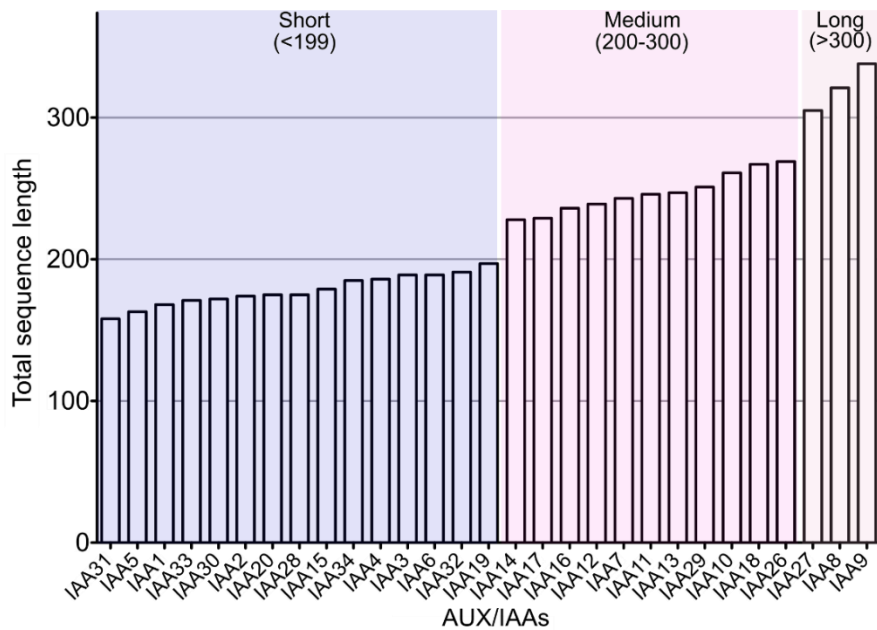
**Figure 11. *At*AUX/IAAs grouped by sequence length.** The 29 AtAUX/IAAs were arbitrary grouped into short (<199 residues), medium (200-300 residues) and long (>300 residues) based in the total number residues. Two representatives of each group were selected for DLS/SLS measurements to study their length and compaction relationship.

DLS determines *At*AUX/IAAs average dimensions based on their diffusion behavior in solution, which is inversely proportional to their Stokes radius ($R_S$). Simultaneously, SLS was carried out to determine the masses of *At*AUX/IAAs in solution, which is indicative of their oligomeric state in equilibrium conditions. IDRs such *At*AUX/IAAs and globular proteins have a characteristic dependency between their $R_S$ and mass, which is described by the scaling law equation: $R_S = a \times M^b$ (Gast & Fiedler, 2012), where $M$ is the protein mass, and $a$ and $b$ are constants that depend on the structural type of the proteins. While globular proteins show a scaling exponent of approximately $b = 0.357$, which is close to that of a sphere shape, fully disordered proteins (here referred as IDRs) scale closer to a value of $b = 0.493$ (Gast & Fiedler, 2012).

For depiction of the scaling behavior of the selected *At*AUX/IAAs, the $R_S$ vs Mass were plotted containing the experimental DLS/SLS information **(Figure 12A)**. We found that full-length *At*AUX/IAAs show an intermediate scaling behavior, which we propose is the result of *At*AUX/IAAs containing a folded C-terminal PB1 domain and an N-terminal IDR. Thus, AUX/IAAs do not scale as completely folded nor as complete IDRs. Our interpretation of the DLS results is further supported by the data from IAA7$^{\Delta PB1}$, which showed a scaling behavior closer to that of IDRs. Conversely, removal of the IDR of IAA7, or IAA7$^{PB1/BM3}$, resulted in a decrease of the scaling behavior compared to full length IAA7$^{BM3}$ and IAA7$^{\Delta PB1}$ **(Figure 12A)**.
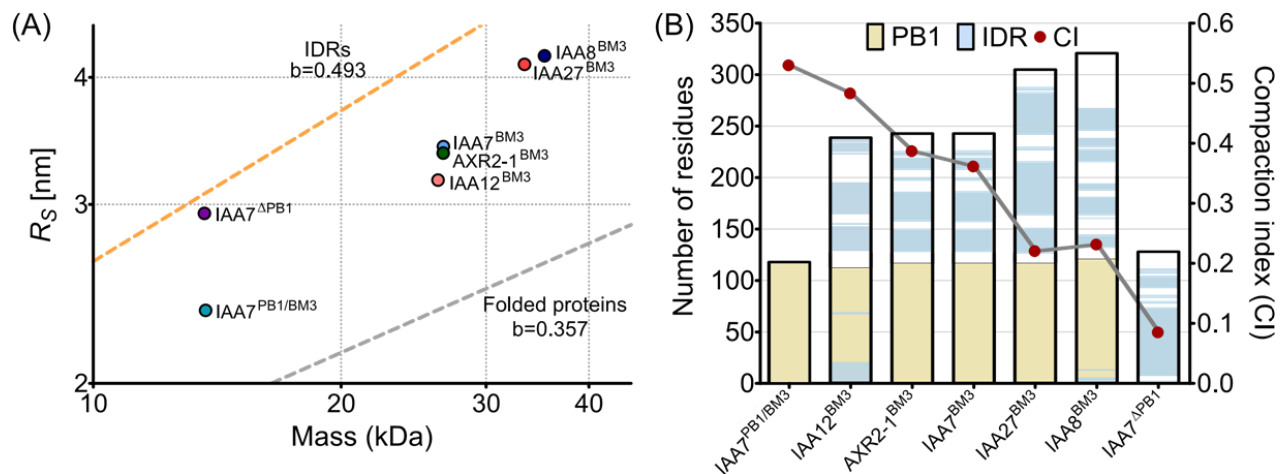
**Figure 12. *At*AUX/IAAs N-terminal IDR length is inversely proportional to their compactness.** (A) $R_S$ vs. mass plot of *At*AUX/IAAs. The $R_S$ and oligomeric state of *At*AUX/IAAs was determined by a combination of DLS and SLS. The plot shows the scaling of IDRs (orange) and folded proteins (gray) in linear regressions where the slope is detonated by the letter "b". For IDRs b=0.493 and for folded proteins b=0.357. (B) Relationship of sequence disorder length and compaction indices (CI) of AUX/IAAs. Compaction indices (CI) were calculated as compactness relative to the scaling behavior of IDRs and folded reference proteins, where a CI=0 represents a complete IDR and a CI=1 represents a globular protein. Bar representation of AUX/IAAs sequence show the PB1 (yellow) and the N-terminal region with IUPRED value scores ≥0.5 (blue) (https://iupred2a.elte.hu/).

To facilitate the interpretation of the scaling behavior of the *At*AUX/IAAs, we expressed $R_S$ values in terms of the compaction index (CI) (Uversky, Santambrogio, Brocca, & Grandori, 2012; Wolff et al., 2020). CI provides a relative measure of protein compactness giving the difference between the scaling exponents of IDRs, and globular proteins with respect to their mass. While globular proteins have a CI = 1, IDRs CI equals 0. When analyzing compactness data of all measured *At*AUX/IAA variants, we observed that compactness is the highest when truncating the N-terminal IDR of IAA7, in the IAA7[PB1/BM3] (CI=0.53) **(Figure 12B)**. IAA7[PB1/BM3] has, however, low compactness compared to a typical globular protein. It is possible that IAA7[PB1/BM3] low CI may reflect the short C-terminal IDR at end of the IAA7[PB1], which is shown disordered by some predictors tools (Niemeyer et al., 2020). IAA7[ΔPB1] showed the lowest compactness with a CI = 0.06, close to what is expected for IDRs, which agrees with the expectation **(Figure 12B)**. Full-length AUX/IAAs showed overall a progressive decrease in their CI values with increasing IDR length, as follows IAA12[BM3]>AXR2-1[BM3]>IAA7[BM3]>IAA8[BM3]>IAA27[BM3] **(Figure 12B)**. Altogether DLS/SLS results showed that *At*AUX/IAAs of different IDR length differ in their degree of compactness. We also established that *At*AUX/IAAs compaction is inversely proportional to the length of their N-terminal IDRs. Our data allow us to predict that *At*AUX/IAAs with longer IDRs correlate with larger $R_S$ and as a result lower compactness. Knowing that IDRs are necessary to expose linear binding motifs, it is possible that the reduced compactness of *At*AUX/IAAs may be

required to expose linear binding motifs required for *At*AUX/IAAs function. It is likely that the observed differences in compactness may change the accessibility of *At*AUX/IAA domains to bind simultaneously their targets. While low compactness may increase exposure of the EAR, degron and PB1, on the contrary, high compactness may reduce it.

### 3.1.2 AUX/IAAs differentially oligomerize through their PB1

A technical advantage of DLS/SLS measurements is its power to discriminate between the oligomeric mixtures of a protein in solution. While we created mutations in the PB1 domain of *At*AUX/IAAs (basic patch mutant 3, BM3) to hinder oligomerization, we noticed that this mutation did not consistently ablated intermolecular interactions, and therefore not always resulted in monomeric *At*AUX/IAAs (**Figure 13**, **Figure S1**). Specifically, we observed that the short length IAA1$^{BM3}$ and IAA4$^{BM3}$ exist in a monomer-dimer equilibrium with a dimer dissociation upon dilution (**Figure 13**). Therefore, we could not extrapolate IAA1$^{BM3}$ and IAA4$^{BM3}$ $R_S$ values to zero protein concentration. Apparently, residues outside the BM3 support oligomerization in *At*AUX/IAA's PB1 domains, as previously proposed (Y. Kim et al., 2020). Nevertheless, we aimed to generate a monomeric version of IAA1 in order to gain structural insights into its self PB-PB1 interaction. To accomplish this, we expressed an IAA1$^{BM4}$ version, which carries an additional lysine to alanine mutation (K155A) by elimination of another positive charge in the PB1 basic patch. This mutation resulted, however, in a monomer-dimer equilibrium similar to IAA1$^{BM3}$, indicating that additional residues support IAA1 oligomerization (**Figure 13**). We concluded that AUX/IAAs oligomerize through different binding mechanism outside the BM3 basic patch, particularly those of shorter length (≤199 amino acids) such as IAA1 and IAA4.
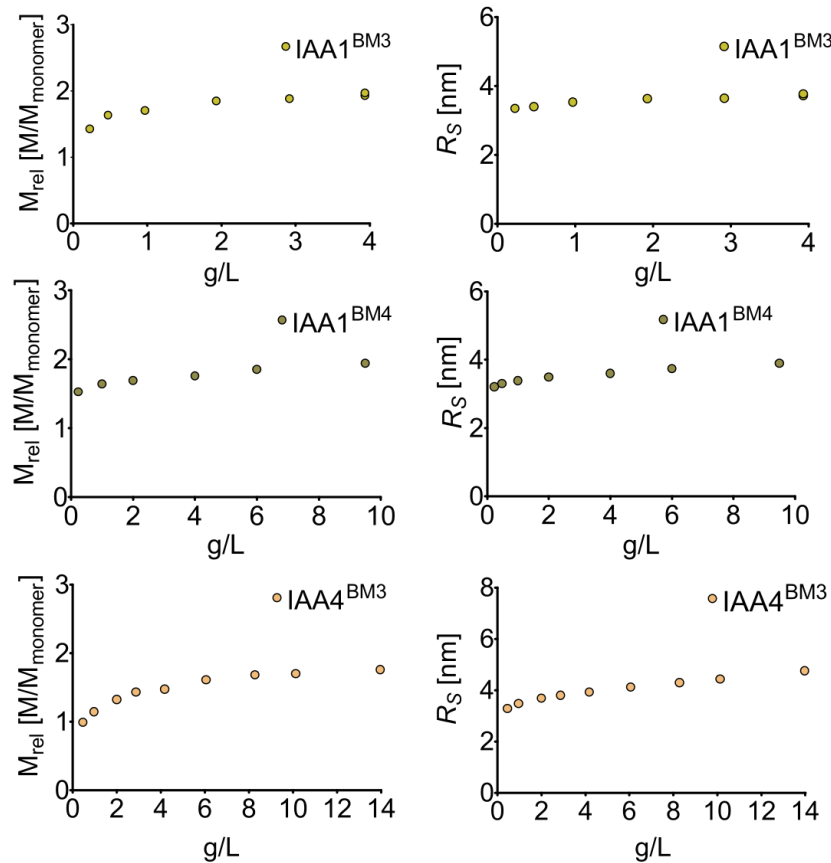
**Figure 13.**Extrapolated mass and $R_S$ of IAA1[BM3], IAA1[BM4] and IAA4[BM3]. SLS and DLS measurements were carried out in serial dilution. The relative mass indicates the number of monomeric units with respect to the protein concentration. IAA1[BM3], IAA1[BM4] and IAA4[BM3] are dimmers which dissociated upon dilution. Extrapolation to zero protein concentration is not possible due to a monomer/dimmer mixture.

### 3.1.3 The size of AUX/IAAs conformational ensemble correlates with their IDR length

In addition to light scattering measurements which showed average AUX/IAAs dimensions by determination of their $R_S$, I applied small angle X-ray scattering (SAXS) in collaboration with Dr. Maria Ott from the Martin Luther University of Halle-Wittenberg (MLU), Halle (Saale). SAXS not only provides average protein size in terms of the radius of gyration ($R_g$), but can also offer powerful information on the conformational ensemble of IDRs via the ensemble optimization method (EOM) (Bernadó, Mylonas, Petoukhov, Blackledge, & Svergun, 2007; Tria et al., 2015). EOM identifies the most probable conformations that best describes the experimental SAXS profiles, resulting in a probability distribution of $R_g$ values and end-to-end distances ($R_{ee}$). $R_{ee}$ is defined as the distance between the first and the last α-carbon atom in a protein (Zhang, Liu, Shang, Shi, & Yun, 2012). Hence, to understand how the PB1 domain and IDRs variability within AUX/IAAs influence their conformational ensemble (*i.e.* size distribution) in the free state, we complemented our DLS/SLS experiments with small angle X-ray scatterings (SAXS) (**Figure**

**14A**). We sought to compare the EOM parameters between IAA7$^{BM3}$ with the IAA7$^{\Delta PB1}$, which lacks the PB1 domain, and with IAA27$^{BM3}$ carrying an IDR sixty-one residues longer than that of IAA7$^{BM3}$, but equal PB1 length (with 68.38% of PB1 sequence identity). The EOM results show that the average $R_g$ ( $\langle R_g \rangle$ ) and average $R_{ee}$ ( $\langle R_e \rangle$ ), as well as the maximum $R_{ee}$ ($R_{ee}^{max}$) for IAA7$^{BM3}$ are larger than IAA7$^{\Delta PB1}$ (**Figure 14B, Table 1**). In the case of IAA27$^{BM3}$ we observed larger values for $\langle R_g \rangle$ , $\langle R_{ee} \rangle$ , and $R_{ee}^{max}$ than IAA7$^{BM3}$ and IAA7$^{\Delta PB1}$ (**Figure 14B, Table 1**). This data agrees with our DLS/SLS data indicating that average dimensions from the largest to the smallest *At*AUX/IAA follows the order: IAA27$^{BM3}$>IAA7$^{BM3}$>IAA7$^{\Delta PB1}$ (**Figure 12A**). $R_{ee}^{max}$ , which informs about the maximum probable distance of the protein ensemble, showed that *At*AUX/IAAs have a propensity to an extended conformation. This propensity appears to increase with larger IDR length (**Table 1**).

Until now, except for $R_{ee}^{max}$, the conformation of *At*AUX/IAAs was explained with parameters that describe their average ensemble size such as $R_S$, $R_g$ and $R_{ee}$. However, to describe AUX/IAAs overall ensemble or their size distribution, we used the full width at half maximum (FWHM) of the $R_g$ distributions (**Figure 14**). The FWHW is the width of the $R_g$ distributions measured between two points on the y-axis, which are half the maximum amplitude. This serves as a proxy for quantitatively describing the conformational ensemble of AUX/IAAs in terms of size distribution. Data showed that the FWHM of $R_g$ value for IAA7$^{BM3}$ (FWHW = 1.24) is twice the value of IAA7$^{\Delta PB1}$ (FWHW = 0.66) (**Table 1**). This implies that the PB1 domain might enlarge IAA7 conformational ensemble despite being a folded domain. Interestingly, for IAA27$^{BM3}$ we measured an FWHM of $R_g$ (FWHW = 1.00) smaller than IAA7$^{BM3}$ despite having a longer IDR (**Table 1**). However, IAA27$^{BM3}$ FWHM is within larger $R_g$ values than IAA7$^{BM3}$ as is shown in the $R_g$ distribution (**Figure 14**). Taken together, these data enable to postulate that the length of the *At*AUX/IAAs IDRs is directly proportional to the size of their conformational ensemble.

We anticipated that differences in *At*AUX/IAAs conformational ensemble size change the way that AUX/IAAs bind to their interacting partners. We specifically focused on the conformation ensemble of *At*AUX/IAAs to gain better understanding of the contribution of regions outside the degron to formation of the auxin receptor complex. I hypothesize that *At*AUX/IAAs conformation ensemble may change from the free to the TIR1-bound state. Specifically, I hypothesize that the

folded, stable, and large size of TIR1, may enlarge the conformational ensemble of AUX/IAAs upon auxin-driven interaction.
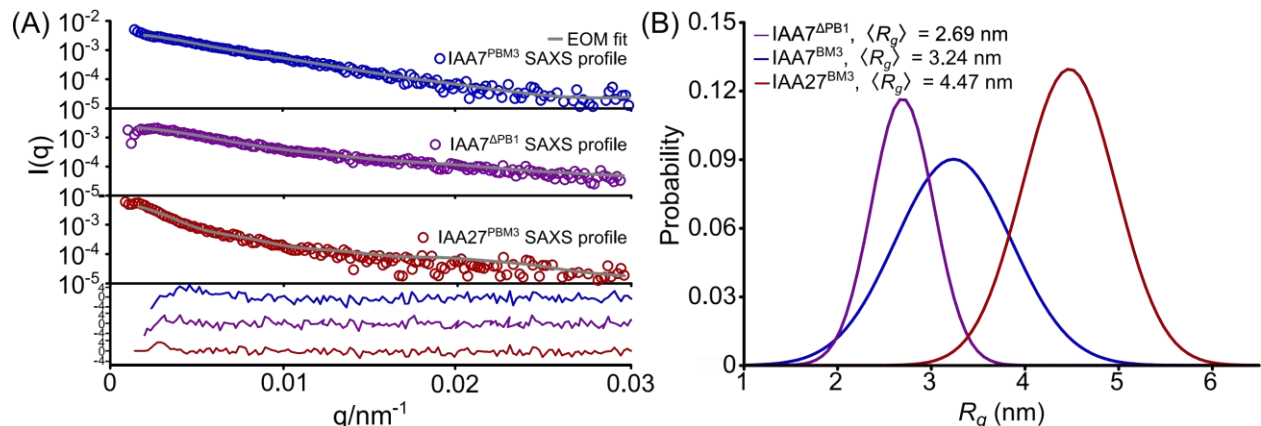


**Figure 14. Conformational space of IAA7$^{\Delta PB1}$, IAA7$^{BM3}$ and IAA27$^{BM3}$ by SAXS.** (A) SAXS profile and EOM fit of IAA7$^{\Delta PB1}$, IAA7$^{BM3}$ and IAA27$^{BM3}$ with their respective residual plot. EOM analyses were performed on the mean scattering intensities of two technical replicas (n=2). (B) Radius of gyration $(R_g)$ distribution by EOM analysis. The FWHM of $R_g$ was used to describe the conformational space of IAA7$^{\Delta PB1}$, IAA7$^{BM3}$ and IAA27$^{BM3}$.

**Table 1.** SAXS parameters calculated from the EOM analysis.

|  | $\langle R_g \rangle$ (nm) | Full width at half maximum (FWHM) | $\langle R_{ee} \rangle$ (nm) | $R_{ee}^{max}$ (nm) |
|---|---|---|---|---|
| IAA7$^{\Delta PB1}$ | 2.69 | 0.66 | 6.06 | 19.84 |
| IAA7$^{BM3}$ | 3.24 | 1.24 | 8.14 | 26.75 |
| IAA27$^{BM3}$ | 4.47 | 1.00 | 9.06 | 30.02 |

## 3.2 How is the conformational ensemble of AUX/IAAs in the free and TIR1-bound state?

SAXS results of IAA7$^{BM3}$ enable to lay out a descriptive image of its conformational ensemble in the free state (**Figure 14**, **Table 1**). Based on $R_{ee}^{max}$ results, we established that IAA7$^{BM3}$ has a propensity to adopt expanded conformations. This resonates with Niemeyer et al., (2020) conclusions, where it was proposed an expanded IAA7$^{BM3}$ conformation may facilitate TIR1 binding on three distinctive TIR1-interfaces. While the degron at the center of the IAA7$^{BM3}$ sequence locks auxin into TIR1's auxin-binding pocket, the PB1 domain binds to TIR1 cluster I and the IDR downstream of the AUX/IAA degron binds to TIR1 cluster II. Since TIR1 clusters I and II span a ~7 nm distance in TIR1's 3D structure, I hypothesized that IAA7$^{BM3}$ conformational ensemble may be increase due to TIR1's large size after binding (**Figure 15A**) (Niemeyer et al., 2020). To test this hypothesis and to identify differences in the conformational ensemble of IAA7$^{BM3}$ between the free and ASK1·TIR1-bound state, I performed single-molecule fluorescence

resonance energy transfer (smFRET) experiments. These experiments were carried out in collaboration with Dr. Maria Ott and Twinkle Bathia from MLU, Halle (Saale). For that, IAA7[BM3] was labeled in the PB1 domain and in the IDR with the ATTO488/ATTO594 donor/acceptor pair, targeting the solvent accessible and native C19 and C244 in IAA7[BM3]. Fluorescence labeling was traced by in-gel fluorescence detection combined with LC-MS/MS detection for validation of site-specific conjugation (**Figure S5C-F**). smFRET measures the energy transfer efficiency ($E$) between two adjacent fluorophores, one donor and one acceptor, which is inversely proportional to the average distance between the two dyes. smFRET sensitivity ranges between 2.5 and 10 nm, which is within the range of biomolecular distances (Lerner et al., 2021).

We first performed smFRET on IAA7[BM3] in the absence of auxin or ASK1·TIR1. From here on in the Results section, indole-3-acetic acid (IAA) is referred to as auxin, which was the only form of auxins used in our biochemical experiments. **Figure 15B** shows the Gaussian fits of the $E$ histograms of IAA7[BM3], where $\langle E \rangle$ denotes the mean value of the distribution. The $\langle E \rangle$ was converted to an ensemble and time averaged distances (described in detail in the Materials and Methods section). This procedure yielded inter-dye distances (also referred as to end-to-end distances ($R_{ee}$) in the literature), called hereafter $R_{ee}^{FRET}$. IAA7[BM3] alone showed an $\langle E \rangle$ =0.38±0.002, equivalent to a $R_{ee}^{FRET}$ = 7.0 nm (**Figure 15B**, **Table S2**). Next, we performed smFRET with IAA7[BM3] which had been preincubated with either auxin or the protein complex ASK1·TIR1. Preincubation of IAA7[BM3] with either auxin or ASK1·TIR1 separately, did not impact the $\langle E \rangle$, resulting in values of $\langle E \rangle$ =0.40±0.002 ($R_{ee}^{FRET}$= 6.87 nm) and $\langle E \rangle$ =0.39±0.003 ($R_{ee}^{FRET}$= 6.74 nm), respectively (**Figure 15B**, **Table S2**). This data shows that neither auxin alone, nor the presence of the E3-ligase receptor module ASK1·TIR1, triggered a measurable change in IAA7[BM3] conformational ensemble. Of note, we measured an increased in the width of the $E$ distribution when IAA7[BM3] was incubated with ASK1·TIR1 (**Figure 15B**, **Table S2**). This change in the IAA7[BM3] $E$ distribution width could be attributed to the weak interaction with ASK1·TIR1 in the absence of auxin, as has been previously reported elsewhere (Cao et al., 2022; Niemeyer et al., 2020). When full auxin receptor complex was reconstituted by preincubating ASK1·TIR1, IAA7[BM3] and auxin, the $E$ shifted to values below 0.40 due to a large inter-dye distance. We determined a $E$ decreased for about 73% of the IAA7[BM3] molecules (**Figure 15B**). For this population, the $\langle E \rangle$ =0.21±0.002 was equivalent to $R_{ee}^{FRET}$ of 9.5 nm (**Figure 15B**, **Table S2**) indicating an expansion of IAA7[BM3] ensemble. The remaining 27% of the molecules was fitted to an IAA7[BM3] unbound fraction with a $\langle E \rangle$ =0.39 equivalent to an $R_{ee}^{FRET}$= 6.74 nm. The unbound IAA7[BM3] fraction could be the result of the spontaneous inactivation of IAA7[BM3] degron via *cis* to

*trans* isomerization at W-P peptide bond (Ramans-Harborough et al., 2023). AUX/IAAs *trans* isomers were proposed to occur naturally and to have a reduced binding to TIR1 even in the excess of auxin (Ramans-Harborough et al., 2023). Taken together, the smFRET data coupled with SAXS allow to propose that IAA7[BM3] may extend in the free state to bind TIR1 top surface. Alternatively, TIR1 may induce an extended IAA7[BM3] conformation upon binding. Overall, we conclude that IAA7[BM3] conformational ensemble changes and expands in the ASK1·TIR1-bound state.

We previously observed that IAA7[BM3] has a relative low compactness by DLS/SLS with a CI=0.36. However, based on our smFRET results we expected that the extended IAA7[BM3] conformation also changes the compactness of the auxin receptor. In this way, the compactness of ASK1·TIR1 would be high due to its folded 3D structure, but ASK1·TIR1 compaction would be reduced in complex with IAA7[BM3] due to the expansion recorded by smFRET. To determine changes in compactness of auxin receptor components, we performed fluorescence cross-correlation spectroscopy (FCCS). In FCCS we measured the fluorescence emission of doubly labeled IAA7[BM3] over time. This allows us to determine the diffusion time ($\tau_D$) of IAA7[BM3] in the detection volume, after autocorrelating and fitting the fluorescence signals. The $\tau_D$ is next use to determine the FCCS $R_S$ ($R_S^{FCCS}$), as protein radius are inversely proportional to $\tau_D$. FCCs measurements were performed simultaneously with the smFRET. Both techniques are complementary to each as protein distances recorded by smFRET may also reflect changes in the complex compactness. First, it was performed FCCS on isolated and doubly labeled IAA7[BM3] for which a $R_S^{FCCS}$ = 3.48±0.18 nm was determined (**Figure 15C**, **Figure S7**, **Table S3**). Preincubation of IAA7[BM3] with auxin alone or ASK1·TIR1 in absence of auxin did not cause any considerable change in $R_S^{FCCS}$ either, indicating the absence of binding or stable binding (**Figure S7**, **Table S3**). However, reconstitution of the full ASK1·TIR1·auxin·IAA7[BM3] complex resulted in an increase of $R_S^{FCCS}$ to 7.56± 0.30 nm (**Figure 15C**). To determine the $R_S$ for ASK1·TIR1 its retention time in a pre-calibrated SEC was used and extrapolated in a linear regression of proteins with known $R_S$, mass and mass and retention time (**Figure S8**). We recorded a monomeric $R_S^{SEC}$ = 3.5 nm for ASK1·TIR1 complex (**Figure 15D, Figure S8**). We next determined the CI for each component of the ASK1·TIR1·auxin·IAA7[BM3] complex. We determined that the CI achieved by the ASK1·TIR1·auxin·IAA7[BM3] (CI = 0.167) complex is lower than the CI of IAA7[BM3] (CI=0.36) and ASK1·TIR1 (CI=1). Moreover, the ASK1·TIR1·auxin·IAA7[BM3] CI is even smaller than the expected CI that would result from summing up the $R_S$ of free ASK1·TIR1 and free IAA7[BM3] (expected CI = 0.27). This only suggests that the reduced compactness of the ASK1·TIR1·auxin·IAA7[BM3] complex

is in fact due to an IAA7[BM3] expansion when bound to ASK1·TIR1 in the presence of auxin. Importantly, we observed a good agreement in IAA7[BM3] $R_S$ determined by DLS/SLS and the $R_S^{FCCS}$. This suggests that fluorescent labeling did not change IAA7[BM3] hydrodynamic dimensions nor its compactness. Taken together, by applying two complementary analyses, such as smFRET and FCCS, we have demonstrated that IAA7[BM3] expands when it binds to ASK1·TIR1 in the presence of auxin.
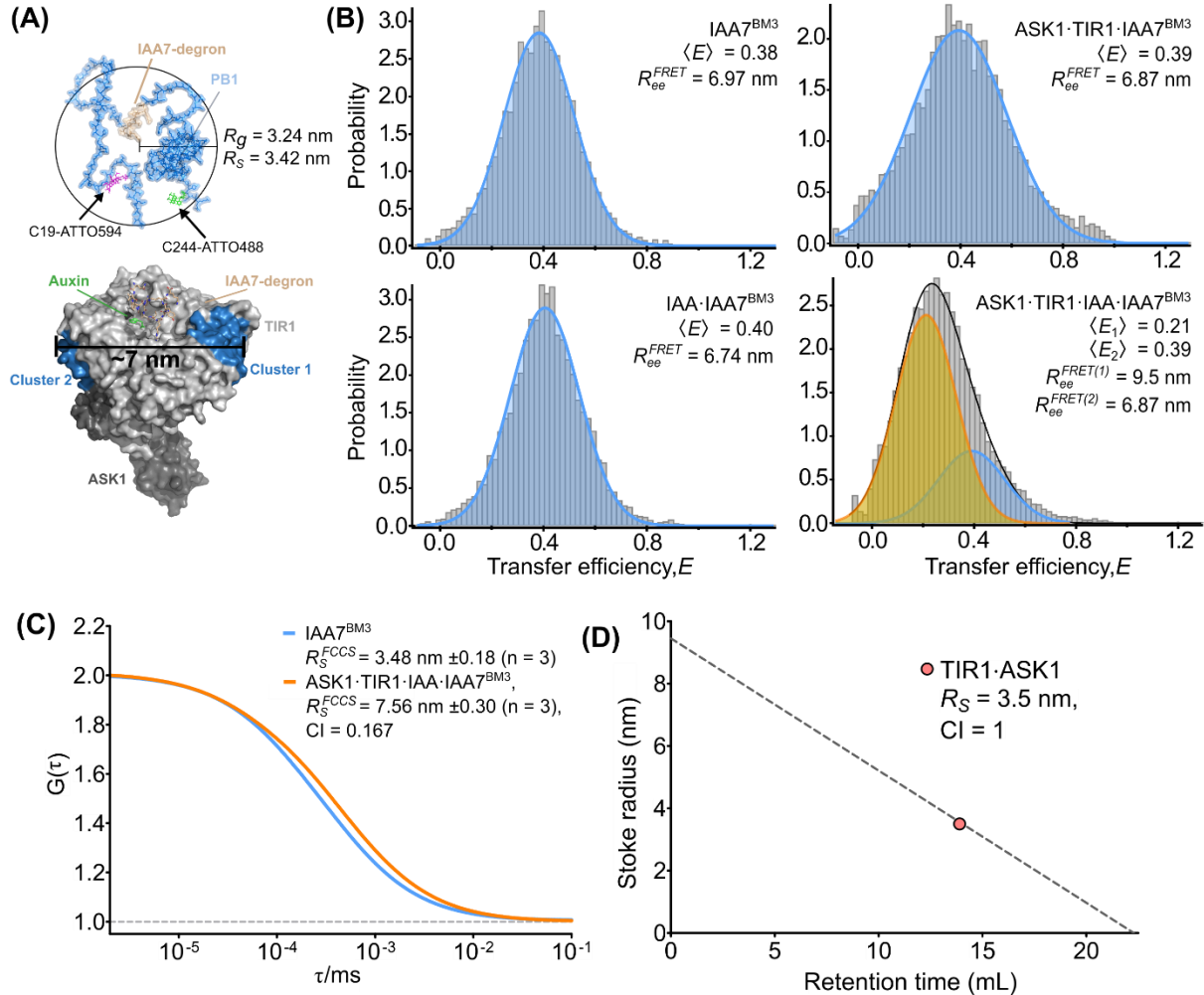


**Figure 15. IAA7[BM3] undergoes an IDR expansion for auxin receptor complex formation.** (A) Alpha fold model of IAA7[BM3] showing modified C19 with ATTO594 (magenta) and C244 with ATTO488 (green) only for depiction, opposite labeling was also possible. IAA7[BM3] average dimensions in the free state by DLS/SLS and SAXS and distance between cluster 1 and 2 binding interfaces are shown. (B) Transfer efficiency histograms of IAA7[BM3] labeled with ATTO488/594 in the presence of IAA, ASK1·TIR1 or ASK1·TIR1·IAA. Blue lines show Gaussian fit of unbound IAA7[BM3], the orange line show Gaussian fit of ASK1·TIR1-bound IAA7[BM3], and the black line is the sum of the distributions. (C) Normalized FCCS fitted curves for IAA7[BM3] labeled with ATTO488/594 in the presence of IAA or IAA·TIR1. The $R_S^{FCCS}$ values correspond to the mean value of three independent experiments ± s.d. (n=3). (D) Determination of ASK1·TIR1 $R_S$ by size exclusion chromatography base on the retention of protein standards of known $R_S$ values (Uversky, 1993).

## 3.3 Do IDRs in AUX/IAAs influence ASK1·TIR1 and AUX/IAAs binding?

After collecting structural and biophysical information of the auxin receptor complex on a global scale, I next focus in understanding the molecular basis of the expanded conformation of IAA7[BM3] when it binds to TIR1. Based on the smFRET data, I hypothesized that if IAA7[BM3] adopts an expanded conformation on top of TIR1, this exposes key contact sites at both ends of the AUX/IAA protein, namely as its IDR and PB1 sides, which allows an enhanced affinity between TIR1 and *At*AUX/IAAs. Previously, Cao et al., (2022) recorded weak affinity between ASK1·TIR1 and IAA7[IDR] ($K_d$ = 18.5 μM) in the absence of auxin. However, this result did not account for the IAA7 PB1 binding contribution towards ASK1·TIR1, as only the IAA7 IDR segment was used. Niemeyer et al., (2020) however, identified residues in IAA7[PB1] that bind to TIR1 by *in silico* protein docking and all-atoms molecular dynamics simulations. But its finding require validation by *in vitro* binding affinity experiments (Niemeyer et al., 2020). In order to provide quantitative *in vitro* data that helps understand the specific contribution of IDRs and PB1 of *At*AUX/IAA to ASK1·TIR1 binding, I carried out microscale thermophoresis (MST) binding assays. The MST assays were performed using ATTO488 labeled IAA7[BM3] and ASK1·TIR1 in the presence of increasing auxin concentrations ranging between 0.001-1000 nM. Here, it is worth mentioning that exhaustive radioligand binding assays (RBA) with [3H]IAA have been previously performed and published by our lab (Calderón Villalobos et al., 2012; B. L. Moss et al., 2015; Niemeyer et al., 2020; Winkler et al., 2017). RBA is paper filter-based system that measures the amount of [3H]IAA retained in the filter that has been captured by ASK1·TIR1·[3H]IAA·AUX/IAAs complexes, while free [3H]IAA diffuses through the filter (Hellmuth & Calderón Villalobos, 2016). Therefore, this method provides a direct measure of auxin binding by auxin receptor complexes. RBA, however, does not reflect the $K_d$ between ASK1·TIR1 and AUX/IAAs directly. For example, the affinity for auxin by RBA may be high by a specific ASK1·TIR1 and AUX/IAA combination because of a strong TIR1·auxin·degron interaction. Nevertheless, this would not reflect the overall binding affinity between the two proteins outside the auxin binding interface.

Using MST experiments I recorded a $K_d$=0.8±0.2 nM of the ASK1·TIR1·auxin·IAA7[BM3] complex (**Figure 16**), which is approximately sixty-fold lower than the reported RBA $K_d$ for auxin of ASK1·TIR1·IAA7[BM3] complex ($K_d$ = ~53 ± 2 nM) (Niemeyer et al., 2020).This data suggest that the extra contacts outside the degron make the affinity between ASK1·TIR1 and IAA7[BM3] greater than the affinity of the same complex for auxin. I next sought to determine the effect of IAA7[PB1] to ASK1·TIR1 binding. Although the PB1 domain exerts highly relevant repression functions in auxin signaling, I sought to determine if it is mechanistically relevant for the ensemble of the auxin

receptor complex. For this, MST analyses with an IAA7 version lacking the PB1 (IAA7$^{\Delta PB1}$) were carried out. I determined an ASK1·TIR1·auxin·IAA7$^{\Delta PB1}$ $K_d$ = 3.7±1.5 nM, which represents a ~four-fold increase in the $K_d$ in comparison with the IAA7$^{BM3}$ variant. This data let us postulate that the PB1 domain enhances the binding affinity between IAA7 and ASK1·TIR1 although is function is not primarily related with auxin sensing (**Figure 16**). Next, I sought to establish whether the IAA7 IDR upstream of the degron influences ASK1·TIR1 binding. The IDR upstream the degron carries the EAR motifs for TPL/TPR interaction and most importantly, the KR motif which has been linked to *At*AUX/IAAs stability *in vivo*. Based on sequence alignment K35 and R36 represent a KR motif in IAA7, which constitutes a conserved NLS for AUX/IAAs (Abel et al., 1995). Previously, thanks to XL-MS data it was proposed that IAA7$^{KR}$ binds to a negatively charged TIR1-interface (*a.k.a.* TIR1 cluster II) (Niemeyer et al., 2020) (**Figure S12**). Therefore, a double charge reversal mutation with K35D and R36D in IAA7$^{IDR}$ was used for MST experiments which may enable to disrupt putative electrostatic interactions between ASK1·TIR1 and IAA7. I recorded an ASK1·TIR1·auxin·IAA7$^{KR \to DD}$ $K_d$ = 16.8±5.5 nM, which represents a twenty-one-fold increase in comparison with the $K_d$ of IAA7$^{BM3}$ (**Figure 16**). This result attests that IAA7$^{KR}$ enhances the affinity to ASK1·TIR1 binding, presumably via electrostatic interactions. Taken together, the MST data shows that regions outside the degron motif allosterically enhance the binding affinity of IAA7 towards ASK1·TIR1 and may underlie the change in IAA7 conformational ensemble when bound to ASK1·TIR1.
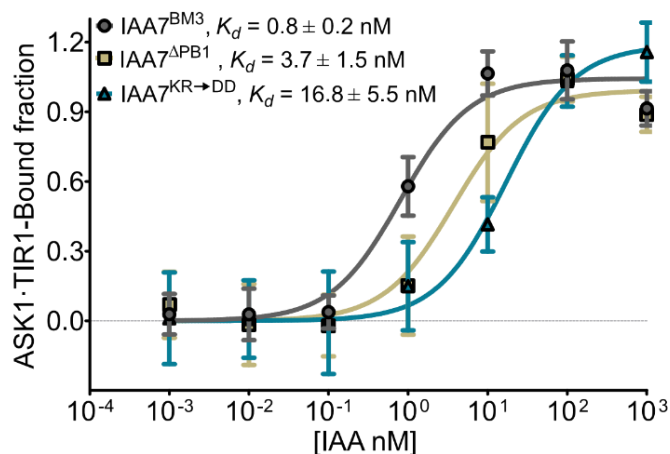


**Figure 16. Binding affinity experiments by MST.** MST experiments were carried out with IAA7 variants (10 nM) and ASK1·TIR1 (10 nM) at increasing concentrations of IAA (0.001-1000 nM). MST experiments were performed in biological triplicates (n=3). Data was evaluated with GraphPad Prism v 5.04 and fitted using "one site total" preset.

## 3.4 How does variability of IDRs in the different AUX/IAAs influence ASK1·TIR1·auxin·AUX/IAAs ensembles?

Considering the aforementioned classification of *At*AUX/IAAs based in length, we have presented ASK1·TIR1 interaction data with IAA7[BM3], a medium length AUX/IAA (**Figure 11**). However, since our structural characterization of *At*AUX/IAAs by DLS/SLS and SAXS revealed that the IDR length changes the overall ensemble of *At*AUX/IAAs structure, we could envision a scenario where the IDR length changes the interaction with ASK1·TIR1. Thus, it is possible that *At*AUX/IAAs with either short (<199 amino acids) or long (>300 amino acids) length differentially change the arrangement or topology of the auxin receptor they are part of. Niemeyer et al., (2020) provided for the first time an overall descriptive topology of the auxin receptor by XL-MS, where it was proposed that IAA7 and IAA12 bind to the top and mushroom shape-like surface of ASK1·TIR1. Specifically, the AUX/IAA KR motif binds to TIR1's cluster II, the degron at the center of the AUX/IAAs locks auxin into the TIR1 auxin binding pocket, and AUX/IAA PB1 binds to TIR1's cluster I (Niemeyer et al., 2020). However, since IAA7 and IAA12 both have a similar IDR content and similar total sequence length (medium length *At*AUX/IAAs), they only provide a limited view of the IDR contribution to ASK1·TIR1 interaction (Niemeyer et al., 2020). In order to understand whether differences in AUX/IAA length and compactness showed previously by DLS/SLS (**Figure 12B**) impact ASK1·TIR1·AUX/IAA complex topologies, I continued applying XL-MS (in collaboration with Dr. Christian Ihling, Dr. Claudio Iacobucci and Prof. Andrea Sinz from MLU, Halle (Saale)). This time two representative short and long length members of the *At*AUX/IAA family were selected.

IAA1[BM3] and IAA27[BM3] were selected as two *At*AUX/IAAs representative members with distinct degrees of compaction and sequence length (**Figure 12B**). The IAA1[BM3] is short length and more compact (CI=~0.49) than the long length IAA27[BM3] (CI=0.27) (**Figure 11**, **Table S1**). I suspected that these differences in IAA1[BM3] and IAA27[BM3] compaction and length might result in different auxin receptor topologies measured by their interprotein XL pattern with ASK1·TIR1. XL-MS experiments were performed using the cleavable crosslinker disuccinimidyl dibutyric acid (DSBU) which covalently crosslinks lysine residues, but are also reactive towards arginine, serine, threonine, and tyrosine residues in proteins  (Ihling, Piersimoni, Kipping, & Sinz, 2021). XL-MS experiments in the absence of auxin resulted in a lower number and less reproducible crosslinks between IAA1[BM3] or IAA27[BM3] and TIR1·ASK1 than reactions containing auxin (**Figure S9**). In the presence of auxin, we observed a similar crosslinking pattern where IAA1[BM3] and IAA27[BM3] mainly crosslink towards TIR1's cluster I and II (**Figure 17A, B**). When focusing on the IAA1[BM3] and

IAA27[BM3] side, it was observed that the N-terminal IDR as well as the PB1 had a bidirectional XL pattern, where both protein regions crosslink in both opposite edges of TIR1. This is indicative of a more dynamic and transient interaction than proposed earlier on Niemeyer et al., 2020, where interactions with TIR1's clusters I and II were shown to be favored in only one direction. XLs outside these two TIR1 cluster interfaces with IAA1[BM3] and IAA27[BM3] were also detected. This might be indicative of additional interactions, albeit weak, taking place within ASK1·TIR1·auxin·IAA1 and ASK1·TIR1·auxin·IAA27 ensembles. This additionally suggests that TIR1 top surface outside the auxin binding pocket may act as platform to bind AUX/IAAs in different conformations. Interestingly, IAA27[BM3] showed a higher diversity in its crosslinking pattern with ASK1·TIR1 than IAA1[BM3]. This diversity in the XL-pattern of IAA27[BM3] with ASK1·TIR1 may be attributed the to its reduced compactness and larger conformational ensemble than IAA1[BM3] (**Figure 17B**, **Figure 12**, **Figure 14**). The larger conformational ensemble of IAA27[BM3] interaction with ASK1·TRI1 is additionally reflected by crosslinks identified between IAA27[BM3] and ASK1 (**Figure 17B**). Taken together, these results suggest that the PB1 domain and N-terminal IDR of AUX/IAAs bind to the same TIR1 cluster I and II interfaces with a bidirectional pattern. These results also indicate that AUX/IAAs carry a common binding mechanism with ASK1·TIR1 regardless of their differences in compactness. Additionally, TIR1 top surface may act as a binding platform which allows AUX/IAAs to land on and establish multiple contacts through their IDR and PB1 domains. This might consequently result in heterogeneous receptor topologies due to structural fluctuations at IDR of AUX/IAAs. The degree of receptor conformational heterogeneity may increase with AUX/IAAs, such as IAA27[BM3], carrying a large IDR and, concomitantly, offering a larger inter- and intraprotein conformational ensemble.
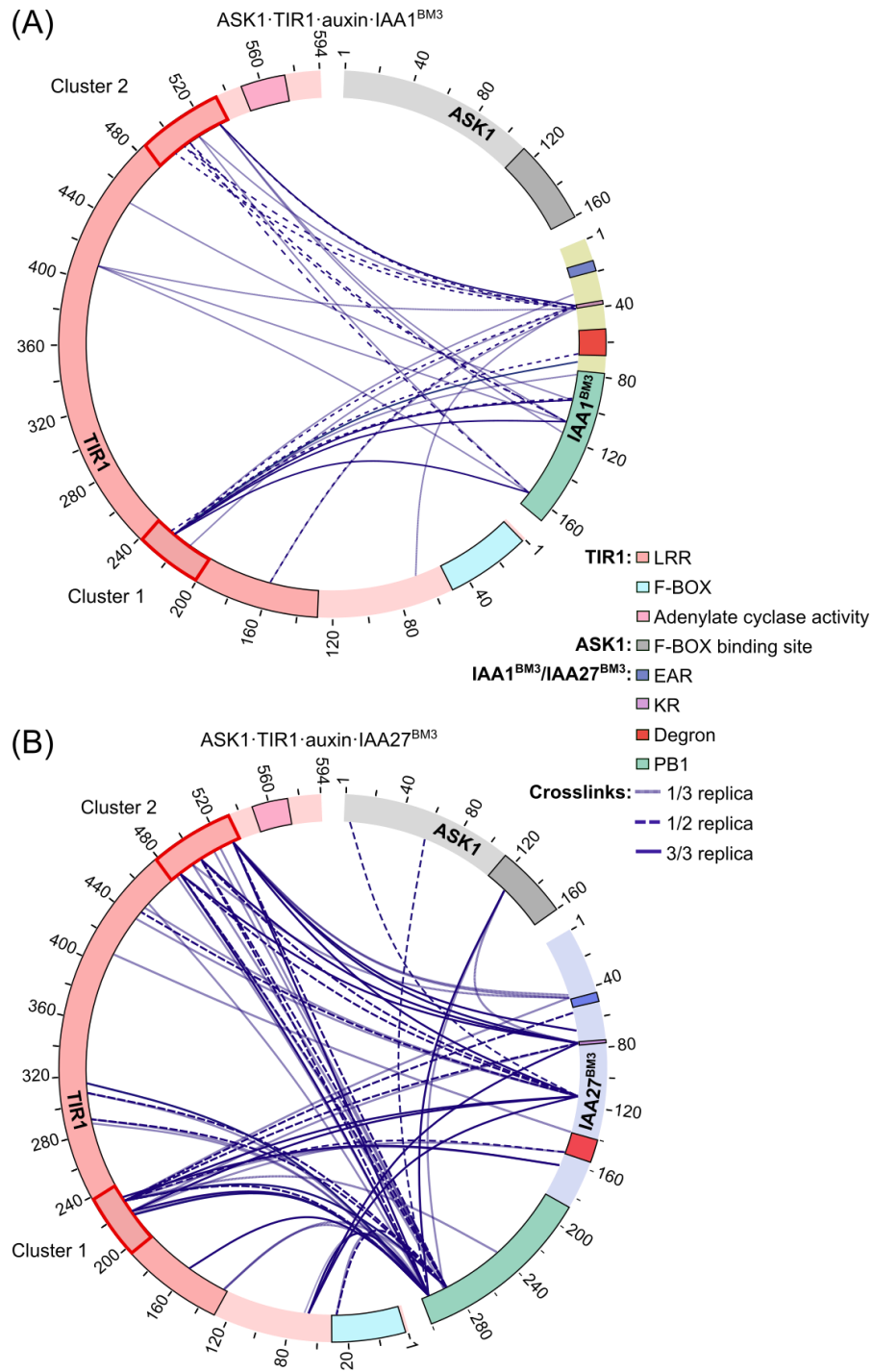
**Figure 17. AUX/IAAs low compactness increases the conformational heterogeneity of auxin receptors.** (A, B) Circular plots showing ASK1·TIR1·auxin·IAA1$^{BM3}$ and ASK1·TIR1·auxin·IAA27$^{BM3}$ inter-protein crosslinks (XLs) in the presence of IAA (n=3). Motifs and protein domains are shown in color code. XL circular plots were generated in: https://xiview.org/.

### 3.4.1 ASK1·TIR1 and AUX/IAAs molecular binding mechanism based on GC-modeling

Although the XL-MS results provide an interaction map between *At*AUX/IAAs and ASK1·TIR1, they are limited by the DSBU reactivity (which targets mainly lysines, threonines and serines) and DSBU linker length (Cα-Cα x̄ = 17.7 Å, Cα-Cα max = 35 Å) (Ihling et al., 2021). To complement these analyses, we reasoned coarse-grained (CG) simulations might provide an additional way to extend molecular modeling and bridge our experimental techniques. Thus, CG could serve to increase orders of magnitude in the time- and length- scales that XL-MS offers. Under that assumption, we carried out one-bead-per-residue CG computational simulations in collaboration with  Dr. Ryan Enemecker and Prof. Alex Holehouse from Washington University in St. Louis (WUSTL), USA using the mPiPi model (Joseph et al., 2021). CG simulations included IAA1, IAA7, IAA12, and IAA27 for which topological conformations on top of TIR1 were previously solved by XL-MS in Niemeyer et al. (2020) and in this work. First, the simulations were carried out where the AUX/IAAs were not fixed to ASK1·TIR1, which resembles an "auxin-free" state.  For the "auxin-free" simulations, we sought to identify residues within AUX/IAA IDRs and PB1 that may play roles in driving interaction between AUX/IAAs and ASK1·TIR1 in the absence of auxin. This is of particular relevance given the fact that ASK1·TIR1 and the IAA7 IDR interact with low affinity in the absence of auxin (Cao et al., 2022). Moreover, auxin-independent interaction between AUX/IAAs and TIR1 have been postulated to drive *in vitro* AUX/IAA ubiquitylation in the absence of auxin (Winkler et al., 2017). It is important to note that due to computational cost, these simulations were not run in a sufficiently large space to accurately compute dissociation constant. Instead, CG simulations were run in a smaller space (500Å-by-500Å) such that we could determine the residues that contribute to AUX/IAA interaction with ASK1·TIR1 (**Figure S10**). Interaction frequencies between AUX/IAAs and ASK1·TIR1 were calculated as inter-protein residue contact frequency. If a residue from AUX/IAA was in contact with a residue from ASK1·TIR1 in a distance ≤10 nm in every frame of our simulation, the frequency would be 100%. Thus, if a residue from AUX/IAA never contacted any residue in ASK1·TIR1, the frequency would be 0%. We found that the most frequent interactions from AUX/IAAs with ASK1·TIR1 were at the core degron motif, GWPPV, and immediate degron neighboring residues for all four AUX/IAAs that we examined, despite any auxin being absent from our simulations (**Figure S10A, C, E and G**). These results agree with the other experimental evidence which supports a strong role for the degron motif in driving AUX/IAAs interaction with ASK1·TIR1 (Tan et al., 2007). In examining other residues driving ASK1·TIR1 AUX/IAA interaction, we noticed that residues just outside of the GWPPV motif in IAA1, IAA7, and IAA27 had higher interaction frequencies with ASK1·TIR1 than the average % frequency driven by each of their respective GWPPV motifs. Although this

could simply be due to their proximity to the GWPPV motif, in the cases of IAA7 and IAA27, these residues included amino acids known to drive relatively strong inter-residue interactions, specifically aromatic and positively charged amino acids. Moreover, the short-predicted IDR that extends past the PB1 domain in IAA7 also had interaction frequencies equal to or greater than the average GWPPV motif interaction frequency. Once again, many of the residues in this short, disordered region are charged or aromatic, suggesting that they may play a role in stabilizing the interaction between IAA7 and ASK1·TIR1 in the absence of auxin.

Apart from the GWPPV motif, each AUX/IAA had a different interaction frequency "signature" highlighting how the differences in AUX/IAA IDRs and PB1 change how they interact with ASK1·TIR1 (**Figure S10**). IAA1 and IAA12 interactions with ASK1·TIR1 are mainly driven by their IDR and to a lesser extent by the PB1 domain. For IAA7 and IAA27 interactions with ASK1·TIR1 occur in similar degree by both IDR and PB1. To evaluate whether these interactions were driven by the sequence of the AUX/IAA IDRs, we also simulated each corresponding AUX/IAA where we replaced the entire IDR with a poly-GS repeat of equivalent length (**Figure S10B, D, F and H**). Replacing the entire IDR with poly-GS in IAA1, IAA7, IAA12 and IAA27 while keeping the native PB1 resulted in either a sharp reduction or complete loss of the IDR and PB1 interactions with ASK1·TIR1. These results support that the interaction frequencies between each of the AUX/IAAs and ASK1·TIR1 was in fact specific to the AUX/IAA IDR sequence, and that both PB1 and IDR cooperatively aid in the interaction with ASK1·TIR1.

After identifying regions of the AUX/IAAs that appear to drive interactions with ASK1·TIR1 independently of auxin, we next sought to determine inter-residues interactions between ASK1·TIR1 and AUX/IAAs in complex. To simulate the AUX/IAAs in the "TIR1-bound" state driven by auxin, we fixed the core degron motif of the selected AUX/IAAs to TIR1's auxin binding pocket. Specifically, the corresponding GWPPV core degron motif of IAA1, IAA7, IAA12 and IAA27 was fixed to where is located in the crystal structure of ASK1·TIR1·auxin·IAA7-degron complex (Tan et al., 2007). We found a large increase in the frequency of interactions with ASK1·TIR1 compared with the "auxin-free" simulations for all simulated AUX/IAAs. This was expected given the degron was fixed relative to the binding pocket (**Figure 18A**). All interaction frequency maps showed a maximum peak centered on the degron motif (**Figure 18A**). For IAA1, IAA7, IAA12 and IAA27, there was a sharp decrease in interaction frequency at the N-terminal region with a low recovery at the KR motif. Moreover, the TIR1-bound simulation showed that the PB1 binds with higher frequency than the IDR upstream the degron to ASK1·TIR1. We observed maximum ASK1·TIR1·PB1 interaction frequency values of 55.91% (L87), 37.39% (L137), 31.22% (R143)

and 38.25% (G226) for IAA1, IAA7, IAA12 and IAA27, respectively (**Figure 18A**). This shows that despite a relatively high PB1 domain conservation (between 60% and 70%) AUX/IAAs differentially bind to TIR1 through their PB1 (**Figure 18A**). When taking a look at the degron tail, the region connecting the degron and the PB1 domain. Our simulations show that flexible degron tails tether the PB1 allowing it to bind in different conformations on TIR1's top surface (**Figure 18B**). Moreover, for each simulated AUX/IAA, the region upstream the degron show low interaction frequency with ASK1·TIR1. This could be due to their structural fluctuations that quickly associate and dissociate with ASK1·TIR1 (**Figure 18A, B**). Based on our simulations, the AUX/IAAs PB1 domain binds in different conformations to TIR1, while being tethered by the degron tail and the IDR upstream of the degron in AUX/IAAs remain highly heterogeneous in conformation. Taken together, this data indicates that TIR1 recognition by AUX/IAAs is cooperatively influenced by both IDRs and PB1, where each AUX/IAA shows differences the binding toward ASK1·TIR1. In the TIR1-bound state the top surface of TIR1 serves as a platform that provides numerous sites for transient interactions which enhance ASK1·TIR1 and AUX/IAA binding. This binding interaction classifies as a fuzzy binding mode, where AUX/IAAs retain their conformational heterogeneity while binding, establishing multiple contacts sites with ASK1·TIR1.

## 3.5 Do IDRs influence AUX/IAA polyubiquitylation?

Our CG-simulations showed a larger conformational space and heterogeneity for AUX/IAAs with longer IDR when bound to ASK1·TIR1 (**Figure 18**). Since ASK1·TIR1 are modules of an SCF – E3 ligase for polyubiquitylation of the AUX/IAAs, I wonder how differences in the conformational ensemble of AUX/IAAs change their ubiquitylation. AUX/IAAs polyubiquitylation dynamics have been observed only *in vitro,* likely due to their short-live and overall low abundance *in vivo* (Niemeyer et al., 2020; Winkler et al., 2017). I envisioned that by reconstituting the AUX/IAAs ubiquitylation *in vitro* we could gain more mechanistically insights in the way that these proteins are polyubiquitylated for targeted-proteasomal degradation. Since SCF – E3 ligases are folded protein complexes with a rigid 3D structure, I anticipated that structural fluctuations at AUX/IAAs IDRs may facilitate ubiquitin transfer to different residues within the AUX/IAAs (**Figure S13**). In fact, the active site of SCF –E3 ligases was estimated to be circa 2.2 nm distance between the lysine acceptor of the ubiquitylation substrate, and the E2~Ub active site (Baek et al., 2020). In this regard, the previous "clusters I and II" (**Figure 6**) binding model for AUX/IAAs and ASK·TIR1 assembly could not explain why *in vitro* ubiquitylation sites are spread out throughout the AUX/IAA primary sequences, as only the PB1 will be in the 2.2 nm range of the E3 active site (**Figure S13**) (Baek et al., 2020; Niemeyer et al., 2020; Winkler et al., 2017). I therefore carried out *in vitro*

ubiquitylation assays for IAA1 and IAA27 by incubating ubiquitin (Ub), E1-Ub activating enzyme, E2-Ub conjugating enzyme, SCF$^{TIR1}$-E3 ligase, auxin (1 µM) and AUX/IAAs. I selected IAA1 and IAA27 as they show contrasting compactness due to their short and long IDR, respectively. The determination of ubiquitylation sites was carried out after AspN and tryptic digestion followed by LC-MS/MS detection in collaboration with Dr. Wolfgang Hohenwarten and Domenika Thieme at the Leibniz Institute of Plant Biochemistry (IPB), Halle (Salle) (Winkler et al., 2017). Ubiquitylation was detected in IAA1 in four lysines (from a total of sixteen lysines), and in IAA27 we identified ten ubiquitylated lysines (from a total of twenty-six lysines) (**Figure 19**). The location of ubiquitylation sites in IAA1 was also limited in distribution between the degron and the EAR motif (at location K39 and K53) and at the PB1 (at location K96 and K110). In the case of IAA27, the ubiquitylation sites distribution is wide and extends up and downstream of the degron. We found seven ubiquitylated lysines at the IDR of IAA27 (at location K67, K76, K117, K123, K141, K155 and K165) and at the PB1 only three ubiquitylated lysines (at location K189, K207 and K286) were identified. The data allows to propose that the observed differences in IAA1 and IAA27 number and patterns of ubiquitylation sites are given due to their conformational ensemble size when bound to TIR1. In this sense, long AUX/IAAs such as IAA27 may have a higher probability of multisite ubiquitylation due to their greater number of lysines and their larger conformational ensemble size when bound to the SCFTIR1-E3 ligase. Conversely, short AUX/IAAs such as IAA1 may have a reduced probability of multisite ubiquitylation not only because of their lower number of lysines but also due to their smaller conformational ensemble size when bound to the SCFTIR1-E3 ligase compared to medium and long-length AUX/IAAs.
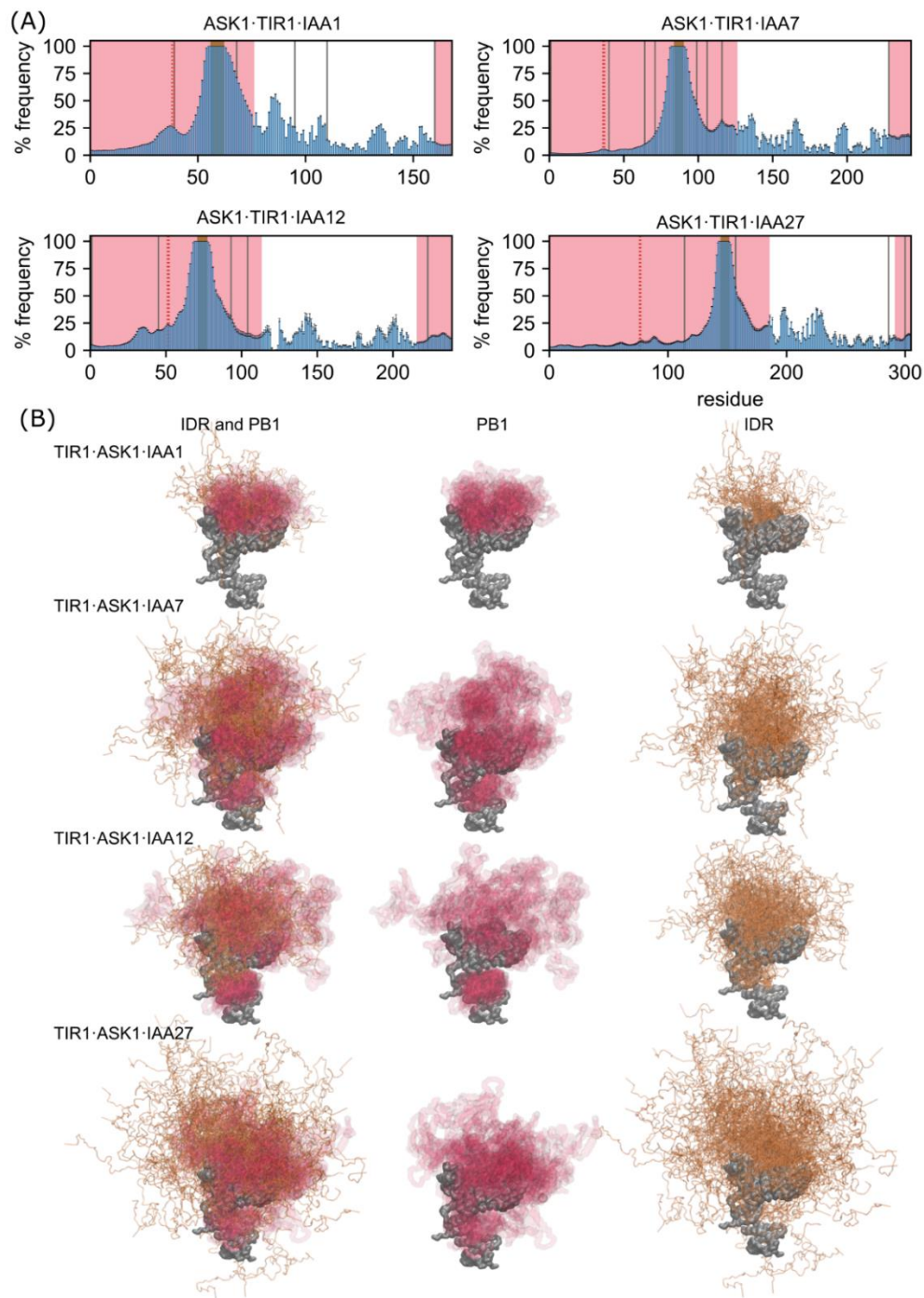
**Figure 18. Mechanism of ASK1·TIR1·AUX/IAA interaction by coarse-grained simulations.** (A) Interaction frequencies of IAA1, IAA7, IAA12, and IAA27 with ASK1·TIR1 are shown in the "TIR1-bound" state. Here, the "GWPPV" core degron motif was fixed at the TIR1 auxin binding pocket as found in the ASK1·TIR1·auxin·IAA7-degron crystal structure (Tan et al., 2007). For all graphs, pink shaded areas denote the IDRs, the brown shaded region is the GWPPV motif, and the red dashed lines signify the location of the KR motif. (B) Conformational heterogeneity of IAA1, IAA7, IAA12, and IAA27 on the top surface of TIR1 by coarse-grained modeling. The multiplicity of *At*AUX/IAAs conformational states in the ASK1·TIR1-bound is accomplished due to the flexible regions flanking the degron and fuzzy binding to ASK1·TIR1.

47

| Position | IAA1 peptide | Replica | Max ion score |
|---|---|---|---|
| 39 | KNNDSTEESAPPPAK | 2/3 | 45 |
| 53 | NDSTEESAPPPAKTQIVGWPPVR | 3/3 | 54 |
| 96 | MYKNYPELLK | 3/3 | 38 |
| 110 | ALENMFKFTVGEYSER | 2/3 | 32 |

| Position | IAA27 Peptide | Replica | Max ion score |
|---|---|---|---|
| 67 | FLALNKSSCPVSGAK | 3/3 | 74 |
| 76 | FLALNKSSCPVSGAKR | 2/3 | 64 |
| 117 | DGKSTTFTKPAVPVK | 3/3 | 39 |
| 123 | STTFTKPAVPVKEKK | 3/3 | 32 |
| 141 | KSSATAPASKAQVVGWPPIR | 3/3 | 57 |
| 155 | KNSMASSQSQKPGNNSETEEAEAK | 1/3 | 50 |
| 165 | KNSMASSQSQKPGNNSETEEAEAK | 3/3 | 62 |
| 189 | SGPEQPCLYVKVSMEGAPYLR | 1/3 | 75 |
| 207 | TYKSYLELSSALEK | 3/3 | 82 |
| 286 | IMKSSEAIGLAPR | 2/3 | 67 |

**Figure 19. *In vitro* ubiquitylation sites of IAA1 and IAA27 detected by LC-MS/MS.** IVU assays with recombinant GST-IAA1 and GST-IAA27, E1 (*At*UBA1), E2 (*At*UBC8), reconstituted SCF[TIR1] (*At*SKP1·TIR1, *Hs*CUL1 and *Mm*RBX1), ubiquitin (*At*Ub) and IAA (auxin, 1 μM). Reactions were stopped with urea after 30 min incubation at room temperature. Samples were doubled digested with AspN and trypsin before LC-MS/MS analysis. IVUs were performed in three independent replicas (n=3). As a negative control, reactions without ubiquitin were also analyzed by LC-MS. Ubiquitylation was not detected in negative control reactions. (A) Depiction of ubiquitylation sites in IAA1 and IAA27 sequence in bar representation. (B) Peptides identified by LC-MS/MS with their ubiquitylation site location in red, times identified in each replica and MASCOT max ion score.

## 3.6 Do AUX/IAAs share a common binding mechanism across plant species for auxin receptor complex formation?
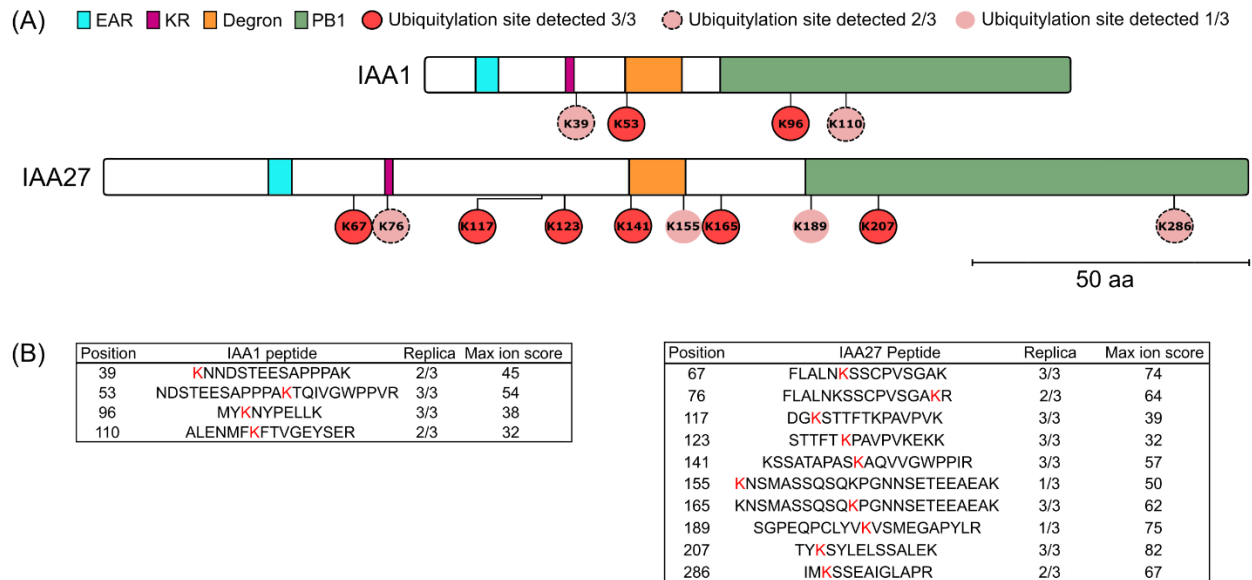
The AUX/IAA family underwent a large evolutionary diversification from early colonizing plants such as *Marchantia polymorpha* with one AUX/IAA to flowering plants such *Arabidopsis thaliana* with twenty-nine members (**Figure 9**) (Mutte et al., 2018). Studies on evolution of AUX/IAAs focused on sequences changes at their functional domains such as the EAR, degron and the PB1 (Mutte et al., 2018; Mutte & Weijers, 2020; Paponov et al., 2009; Wu et al., 2017). However, little is known about the IDRs that interconnect these functional domains as it was generally assumed that they do not carry any binding function. Divergence at AUX/IAAs IDR has also hindered sequence alignment analysis as these regions show a low percentage of sequence identity. From the structural point of view, it is also unknown how AUX/IAAs intrinsic disorder changed across land plant species. Based in our biophysical, biochemical and computational results, we found that variable IDRs indeed affect the binding to ASK1·TIR1 and AUX/IAAs ubiquitylation. Our CG-

simulations also let us postulate that AUX/IAAs degron tail carries tethering functions allowing its PB1 domain to bind to TIR1 top surface in different conformations. Recently, it was shown that a degron tail deletion in deletion of *Sisymbirum orientale* (*Os*) IAA2 reduced the binding affinity towards *At*TIR1 and *At*AFB5 compared to *Os*IAA2 wild-type (Figueiredo et al., 2022). The letter work also supports the hypothesis that IDRs that connect domains of AUX/IAAs are important for their functionality. Growing evidence has also shown that IDRs that function as flexible tethers are essential for kinase signaling, gene silencing, enzyme catalysis, transcriptional regulation, and the formation of biomolecular condensates (Beh, Colwell, & Francis, 2012; Brodsky et al., 2020; Das, Huang, Phillips, Kriwacki, & Pappu, 2016; Dyla & Kjaergaard, 2020). Flexible tethers are thought to encode IDR's size and to carry functions based on their length, composition, and pattering (González-Foutel et al., 2022). An ongoing hypothesis in the intrinsic disorder community is that evolutionary selective pressure preserved length over sequence similarity in tethering linkers (González-Foutel et al., 2022).

Noticing the gap in knowledge of AUX/IAAs flexible linkers and their importance for IDRs functionality, we sought to study interspecies changes in these regions that could hint to functionality for auxin receptor complex formation. Although divergent IDRs cannot be studied under the basis of sequence alignment, features such as the IDR length could provide information about their compactness and conformational ensemble size as we proposed before based in our DLS/SLS and SAXS results. We speculated that selective pressure at the degron tail may have constrained its length for its tethering of the PB1 domain when assembling the auxin receptor complex. Furthermore, our CG-simulations showed that a region upstream of the AUX/IAA degron is highly heterogeneous in conformation when AUX/IAAs are bound to TIR1; and, that larger AUX/IAAs IDRs may favor ubiquitylation. Therefore, I also wonder if there any constrain at their IDR upstream of the degron that could hint to a conserved structural role for the formation of the auxin receptor complex in land plants (**Figure 20A**). In collaboration with Jana Trenner and Prof. Marcel Quint from MLU, Halle (Saale), we first built a dataset of 1534 AUX/IAA canonical sequences. We included sequences from 73 land plants covering all major seven land plant species groups *i.e.* bryophytes, lycophytes, ferns, gymnosperms, angiosperms basal, angiosperms monocots and angiosperms dicots (**Table S4**).

Next, IUPRED2A (https://iupred2a.elte.hu/) disorder predictions were performed to the whole dataset and their predicted percentage (%) of disorder was calculated. The % of disorder was defined as the % of normalized number of residues with IUPRED2A scores >0.5. We observed that the % of disorder in the data set ranges from 0 to 83.15%, indicating a large disorder variability

among AUX/IAAs from land plants (**Figure 20B**). Since we also noticed that AUX/IAAs from different land plants carry different sequence length, we wondered if AUX/IAAs length correlates with their % of intrinsic disorder. We performed a correlation analysis between these two variables and found a positive correlation with a moderate Pearson correlation coefficient value (*r* = 0.56) (**Figure 20B**). This result indicates that the % of disorder in land plant AUX/IAAs increases with larger sequence length. We then determined which part of the AUX/IAAs sequence in the dataset is responsible for their length differences. To simplify the charting of AUX/IAA, we split AUX/IAAs sequences in the dataset in two parts based on the origin of the PB1. Here, everything upstream of the PB1 is referred as the N-terminal region and everything downstream of the beginning of the PB1 is considered as PB1 domain. We counted the number of residues of each region and calculated their average sequence length and coefficient of variation (CV). We observed that the N-terminal IDR is in average larger ($\bar{x}$=145.5±59.86 amino acids) than the PB1 ($\bar{x}$=109.4±14.73 amino acids) (**Figure 20C**). We used the CV as a parameter to determine the degree of length variation within each AUX/IAA region. With this analysis, we observed that the AUX/IAA sequence length variability is 9.2% higher at the IDR compared to the length of PB1 (**Figure 20C**). We concluded that differences in AUX/IAAs length come mainly from their N-terminal region, which is then responsible for their % of IDR content.

Next, we sought to study how sequence length and % of intrinsic disorder changed across land plant groups. Specifically, we wanted to establish if intrinsic disorder may have a more prominent structural role in some plant groups over others. First, we grouped AUX/IAAs sequences according to their species group and calculated each group average % of disorder and sequence length (**Figure 20D**). We found that the bryophytes group contains the longest ($\bar{x}$=575.75±166.35 amino acids) and most disordered ($\bar{x}$=68.71%±10.13) AUX/IAAs in our dataset. Bryophytes were followed by lycophytes which in average were $\bar{x}$=367.47±81.69 amino acids long and $\bar{x}$=62.72%±9.64 disordered, although these differences were not statistically significant (**Figure 20D**). The group of ferns seems significantly shorter in sequence length and % of disorder compared with bryophytes and lycophytes with values of $\bar{x}$=341.38±89.35 amino acids and $\bar{x}$=43.12%±17.86, respectively (**Figure 20D**). Gymnosperms were in average longer and more disordered than ferns, that but not than bryophytes and lycophytes, with length and % of disorder values of $\bar{x}$=379.29±117.22 amino acids and $\bar{x}$=52.28%±18.60, respectively (**Figure 20D**). All angiosperms' groups were significantly shorter and less disordered than bryophytes and lycophytes. Angiosperms basal, monocots and dicots showed overall a similar amino acids length with values of $\bar{x}$=239.36±83, amino acids, $\bar{x}$=247.82±59.69, and $\bar{x}$=244.35±67.51, respectively. In terms of % of disorder angiosperm basal, monocots and dicots were $\bar{x}$=38.40±20.04,

x̄=39.46±13.43, and x̄=30.27±14.96, respectively (**Figure 20D**). The data points out a larger role of intrinsic disorder in early colonizing land plants, particularly those belonging to the group of bryophytes and lycophytes as they show the largest % of disorder. Nevertheless, angiosperms have a larger number of AUX/IAAs copies in their genome, therefore the total contribution of AUX/IAAs disorder in relationship to their overall proteome may be larger in angiosperms. Altogether, the data shows a progressive decrease in the total sequence length and % of intrinsic disorder in AUX/IAAs of plants with larger complexity.

After obtaining a general view of AUX/IAAs in terms of length and % of disorder of the dataset, we next focused on the length of the IDR upstream the degron and the degron tail based in our sequence alignment. In this dissertation we showed that the N-terminal IDR upstream the degron is highly heterogeneous in conformation when AUX/IAAs bind to ASK1·TIR1. While the degron tail tethers the PB1 so it binds to ASK1·TIR1. We hypothesize that selective pressure may have preserved the length at these two regions to retain AUX/IAAs ensemble/function features. We measured the length at the IDR upstream the degron (called hereafter IDR upstream) and the degron tail based on sequence alignment of the dataset. The results showed that the IDR upstream are in average longer than degron tails, with mean values of 112.0±55.40 and 30.44±12.02 residues, respectively (**Figure 20E**). The IDR upstream also show a 27.6% larger variation compared to the degron tail based in their CV values (**Figure 20E**). Altogether this data hints towards a length conservation, especially at the degron tail for tethering function. The IDR upstream shows greater length variability which points out a less conserved structural role across land plant species.

To experimentally test whether the differences in sequence length and % of disorder also change AUX/IAAs ensembles, we recombinantly expressed two *Physcomitrium patens* (*Pp*) AUX/IAAs. *Pp*AUX/IAAs belong to the group of bryophytes, which contain the longest and most disordered AUX/IAAs in our dataset. To evaluate *Pp*IAA/IAAs average ensemble we performed DLS/SLS on *Pp*IAA1A and *Pp*IAA1B and compared their $R_S$ and CI with *At*AUX/IAAs. Our results show that both *Pp*IAA1A and *Pp*IAA1B have larger dimensions than all *At*AUX/IAAs, which correlates with their larger content of predict disorder length (**Figure 21A**). We next calculated *Pp*IAA1A and *Pp*IAA1B CI. Surprisingly, their compactness was greater than IAA8 and IAA27, two of the longest *At*AUX/IAAs (**Figure 21B**). These results suggest that, although their overall dimensions are larger than average, *Pp*IAA1A and *Pp*IAA1B may sustain transient and/or stable intramolecular interactions at their long IDRs, which might compact their structure.

Altogether, our *in silico* analyses coupled with DLS/SLS measurements of *Pp*IAA1A and *Pp*IAA1B show how IDRs linkers directly change AUX/IAAs average ensemble size. It is likely that longer IDRs may as well change AUX/IAAs functionality and regulation *i.e.*, posttranslational modification, turnover and way of interaction with other protein partners. Future studies should aim to elucidate the roles of interspecies IDRs flexible linkers for AUX/IAAs interaction and auxin receptor formation. This should reveal the additional functions of AUX/IAAs divergent IDR linkers in land plants.
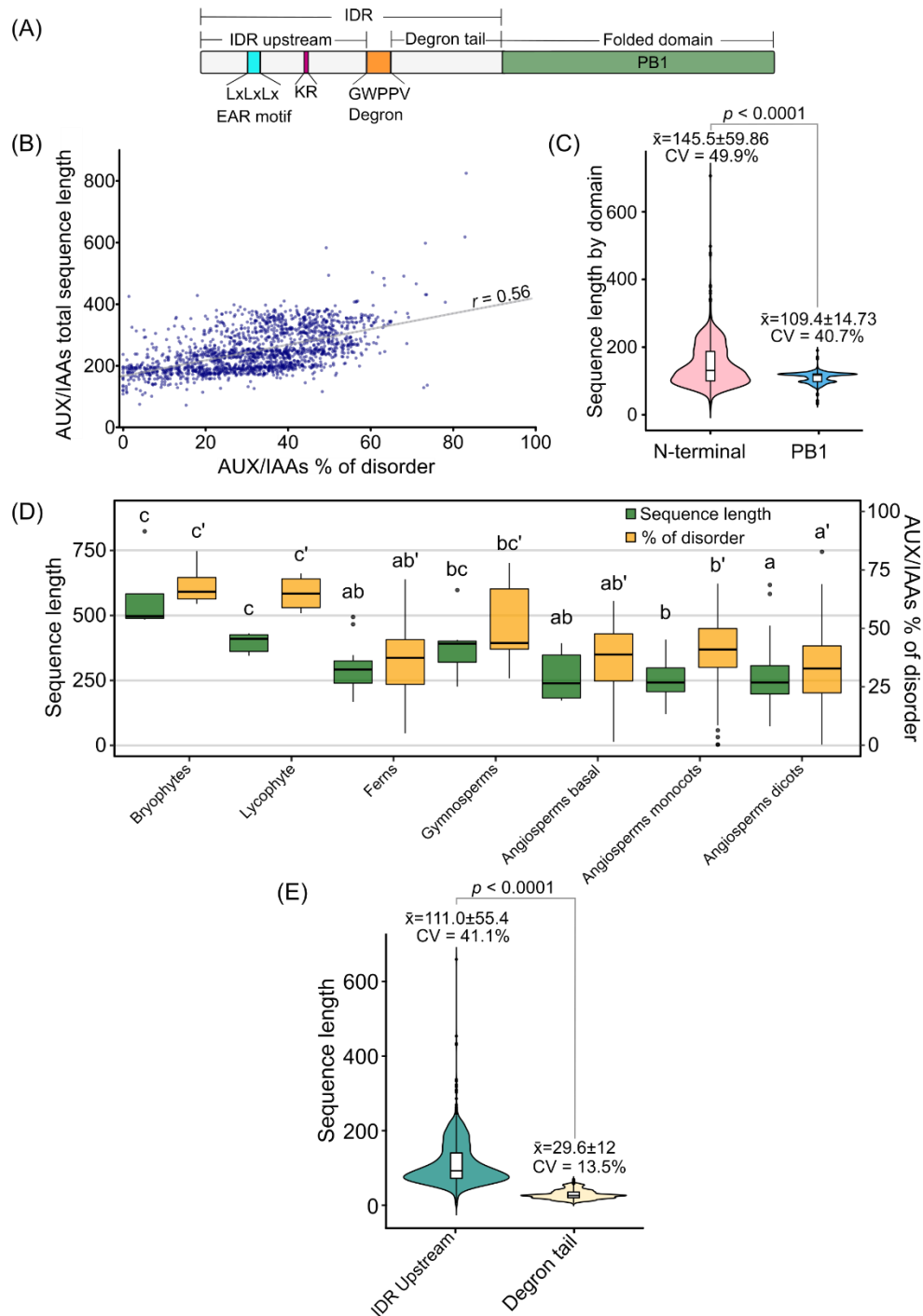
**Figure 20. AUX/IAAs sequence features across land plant species.** (A) Bar representation of AUX/IAAs depicting sequence motifs at the IDR and the PB1. (B) Correlation between sequence length and % of intrinsic disorder in land plants AUX/IAA sequences (n = 1535). Results show a positive intermediate correlation with a Pearson correlation score of $r$ = 0.56. (C) Sequence length variability of AUX/IAAs PB1 and N-terminal IDR (n = 1535) ($p<0.001$ was calculates using two-tailed Student's t-test). (D) AUX/IAAs sequence length and % of disorder variability across the major land plant groups; bryophytes n = 4, lycophytes n = 6, ferns n= 15, gymnosperms 7, angiosperms basal n = 9, angiosperms monocots n = 253

53

and angiosperms dicots = 1240 (one-way ANOVA was followed by multiple comparison Tukey's significant difference test). (E) Sequence length of degron tail and linker region of AUX/IAAs across land plant species (n = 1535) ($p<0.001$ was calculates using two-tailed Student's t-test).
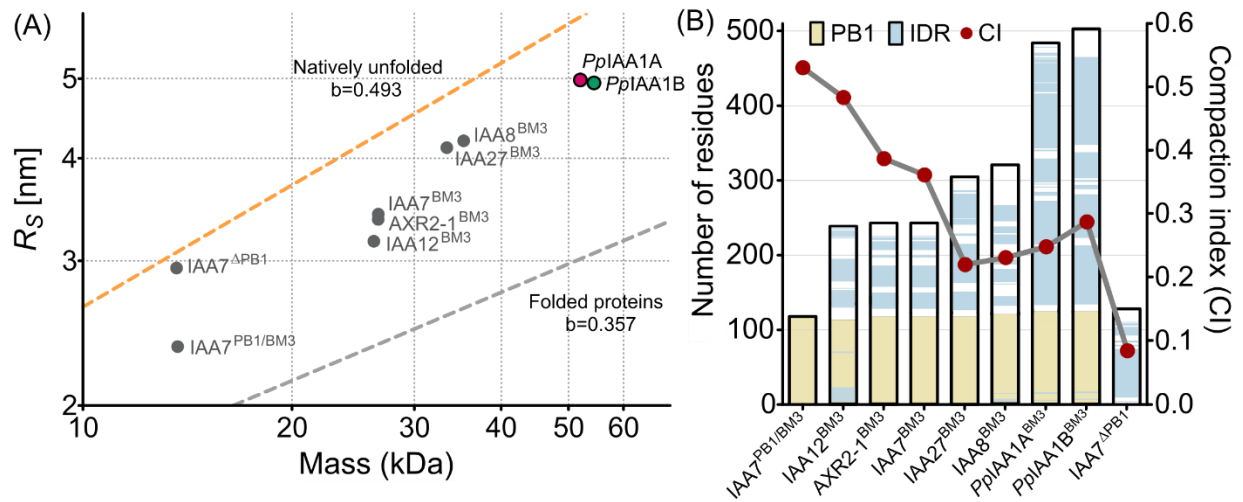


**Figure 21.** *Physcomitrium patens* (*Pp*) **AUX/IAAs show larger dimensions than** *At***AUX/IAAs but greater compactness.** (A) $R_s$ vs. Mass highlighting the dimensions of *Pp*IAA1A and *Pp*IAA1B in relationship to their respective masses. (B) Relationship of sequence disorder length and compaction (CI) of AUX/IAAs. Compaction indices (CI) were calculated as compactness relative to the scaling behavior of IDRs and folded reference proteins, where a CI=0 represents a complete IDR and a CI=1 represents a globular protein. Bar representation of AUX/IAAs show the PB1 and the N-terminal region with IUPRED value scores ≥0.5 in blue.

# 4. Discussion

## 4.1 AUX/IAAs conformational ensemble changes from compact to expanded for auxin receptor complex formation

smFRET results showed that the average conformational ensemble of IAA7[BM3] changes from compact in the free state to expanded in the TIR1-bound state (**Figure 15B**). This change in IAA7[BM3] average conformational assembly is relatively large with an experimental distance difference from C19 to C244 of ~26 Å between the free and ASK1·TIR1-bound state (**Table S2**). An expanded conformation was also found for the Cdc4-phosphodegron (CPD) in pSic when is bound to the F-BOX protein Cdc4 at the substrate recognition binding site (Orlicky, Tang, Willems, Tyers, & Sicheri, 2003). Further, *in silico* ensemble experiments with pSic showed that 75% of the free pSic conformers have accessible conformations in at least one CPD that are consistent with the bound conformation to Cdc4 (Mittag et al., 2010). The relative fraction of different CPDs adopting binding-competent conformations reflects their propensity for extended structures and the importance of the flexibility of disordered states for its binding function (Mittag et al., 2010).

In the case of AUX/IAAs, our SAXS experiments coupled with the EOM analysis evidenced that IAA7[BM3] explores expanded conformations in the free state. In fact, the EOM results showed that a $R_{ee}^{max}$ = 26.75 nm for IAA7[BM3] suggesting a propensity to expanded conformations in the free state (**Table 1**, **Figure S4**). Therefore, during the ensemble of the auxin receptor complex, a conformational selection mechanism could occur. Here, the IAA7[BM3] may spontaneously expand in the free state, and TIR1-binding occurs when the IAA7[BM3] expanded conformation is available. Alternatively, ASK1·TIR1 may bind to IAA7[BM3] at different contact points and induce the expanded conformation observed by smFRET, a mechanism called "induced fit". In the induced fit mechanism, the expanded IAA7[BM3] conformational ensemble will be induced and sustained by intermolecular contacts between ASK1·TIR1 and IAA7[BM3]. Some of the IAA7[BM3] intermolecular contacts with ASK1·TIR1 occur at the AUX/IAA PB1 domain and the KR motif, since when truncated or exchanged, they altered ASK1·TIR1- IAA7[BM3] binding affinity as shown in MST experiments. Our CG-simulations also showed that both AUX/IAA IDR and PB1 cooperatively bind to ASK1·TIR1 in an auxin-dependent and -independent manner. Both conformational selection and induced fit mechanisms may be equally plausible and would depend on the initial conformational state of IAA7[BM3] during binding.

## 4.2 Structural and functional implications of AUX/IAAs compactness and conformational ensemble

In *Arabidopsis*, 23 canonical AUX/IAAs respond to the intracellular levels of auxin by engaging in the formation of auxin receptor complexes together with TIR1/AFBs. Outside the ASK1·TIR1·auxin·IAA7-degron, TPL·EAR and the *Ps*IAA4[PB1] solved structures, no structural data was available for full length AUX/IAAs (Dinesh et al., 2015; Tan et al., 2007). Therefore, the functional roles of variable regions outside canonical domains were unknown. Recent work proposed that AUX/IAAs are intrinsically disordered at the N-terminal region by applying CD spectroscopy and hydrodynamic techniques, but these results were limited to IAA7 and IAA12 (Niemeyer et al., 2020). In this dissertation, the biochemical, biophysical, and *in silico* modeling work sought to expand the structural characterization of *At*AUX/IAAs to four canonical members and two *Pp*AUX/IAAs. By analyzing representative *At*AUX/IAAs members of short, medium and long amino acid sequence length (**Figure 11**), the DLS/SLS results showed that the length of *At*AUX/IAAs N-terminal IDR is inversely proportional to their compactness in solution (**Figure 12 A, B**, **Table S1**). Moreover, the SAXS analysis coupled with the EOM results showed that the conformational space of IAA27[BM3] is larger than IAA7[BM3], as IAA27[BM3] carries a longer IDR than IAA7[BM3] (**Figure 14**, **Figure S4**). It is likely that the reduced compactness may increase the exposure of AUX/IAAs binding sites allowing them to simultaneously carry transcriptional repression and auxin sensing functions. In this sense, AUX/IAAs may be simultaneously bound to TPL/TPRs and to the PB1 of ARFs as the EAR and the PB1 domain are located at the N- and C-terminal edges of the AUX/IAAs. These two repression interactions should at the same time allow the degron to be exposed for auxin driven- SCF[TIR1/AFBs] interaction depending on the cellular requirements.

Moreover, reduced compactness of the longest *At*AUX/IAAs such as IAA8[BM3] and IAA27[BM3] may increase the potential number of protein-protein interactions and/or posttranslational modifications in comparison with the shorter and/or medium length AUX/IAAs. Recently, it was reported that mitogen-activated protein kinase 3 (MPK3) strongly phosphorylates *in vitro* IAA4, IAA7, IAA8, IAA12, IAA14, IAA15, IAA18 and IAA34 (Sun H. Kim et al., 2022). These results do not show any length dependency as phosphorylation occurs in short, medium and long sequence length AUX/IAAs. However, the same authors showed that IAA15 phosphorylation occurs at the N-terminal IDR at position S2 and T28 (Sun H. Kim et al., 2022). This highlights the regulatory functions that are encoded in AUX/IAA IDRs for MAPK3 recognition and phosphorylation. Moreover, it was recently shown that nitric oxide (NO) mediates the S-nitrosylation of IAA17 at

C70 in the IDR *in vivo,* and that this stabilizes IAA17 by reducing the interaction with ASK1·TIR1 interaction (Jing et al., 2023). It is likely that reduced compactness and a large conformational ensemble increase exposure of not only canonical domains, but also recognition and binding sites for other regulatory proteins such as kinases and S-nitrosylases. This may add an additional layer of regulation to AUX/IAAs expanding their role in cellular signaling.

Our DLS/SLS results with the moss *Pp*IAA1A$^{BM3}$ and *Pp*IAA1B$^{BM3}$ showed larger dimensions via $R_S$ values than the largest *At*AUX/IAA, which we attributed to their longer IDR (**Figure 21A**). Despite their larger dimensions, *Pp*IAA1A$^{BM3}$ and *Pp*IAA1B$^{BM3}$ showed more compactness than that the long length *At*IAA8$^{BM3}$ and *At*IAA27$^{BM3}$ (**Figure 12B**, **Figure 21B**). It is likely that transient and/or stable secondary structural elements at the N-terminal IDR may be compacting *Pp*IAA1A and *Pp*IAA1B structure, although this hypothesis should be further validated as well as its functional implications for auxin receptor complex formation. Secondary structural elements were also found by NMR studies with *At*IAA17, where the EAR motif (from E11 to G20) showed helical propensity while the degron motif (from Q82 to K94) showed β-sheet propensity (Sigurd Ramans et al., 2019) . Transient secondary structures were also found for human Sic1, a ubiquitylation substrate of Cdc4. Sic1 and its phosphorylated form pSic showed a significant amount of transient secondary and tertiary structure according to chemical shifts and relaxation rates by NRM although they are IDRs (Mittag et al., 2010). Although our results provide structural information in low resolution scale by DLS/SLS and CI values, high resolution techniques such as NMR coupled with ensemble modeling methods could provide per-residue information about the structural content and self-interaction of AUX/IAAs IDRs.

Altogether, the results presented in this dissertation show how *At*AUX/IAAs IDRs length is inversely proportional to *At*AUX/IAAs compactness and directly proportional to their conformational ensemble size. Together, reduced compactness and larger conformational ensemble of AUX/IAAs may simultaneously expose their canonical binding sites providing binding platforms for different protein partners depending on the cellular requirements.

## 4.3 AUX/IAAs reduced compactness and large conformational space increases the conformational heterogeneity ASK1·TIR1·auxin·AUX/IAAs complexes

The results by XL-MS coupled with molecular dynamic simulations showed that AUX/IAAs establish multiple contacts with ASK1·TIR1 during auxin sensing. AUX/IAAs contacts include, but are not limited to, TIR1's cluster I and II (**Figure 17B**). In this way, the top surface of TIR1 may

act as a platform to bind AUX/IAAs in different conformations hinting at a fuzzy binding mode at the AUX/IAAs IDR and PB1 domains, while its degron locks auxin into TIR1 auxin binding pocket (**Figure 18B**). From a functional point of view, this multiplicity of interactions might lead to two outcomes. On one hand, these multiple transient interactions enhance the binding affinity towards ASK1·TIR1, while strengthening the auxin receptor binding stability. However, the IDR and PB1 sequence variability among the 23-degron containing AUX/IAAs may change the binding strength of these transient interactions towards TIR1/AFBs. This would result in different TIR1/AFBs and AUX/IAA affinities among the 134 potential auxin receptor complexes. On the other hand, a fuzzy binding facilitates the polyubiquitylation of AUX/IAAs in different lysine residues across the primary sequence of AUX/IAAs. This occurs by AUX/IAAs flexibility at their IDRs when bound to the SCF$^{TIR1}$ –E3 ligase. In fact, when taking a look at AUX/IAAs ubiquitylation sites, we observe that they are spread out through the primary sequence (**Figure 8B**). Therefore, a static interaction of AUX/IAAs with TIR1 in the proposed cluster I and II model, would only make accessible the PB1 to the active site of the SCF$^{TIR1}$ –E3 ligase (**Figure S13**). The active site of SCF E3-ligases has been measured to have a distance of 22 Å between the E2~Ub active site and the lysine acceptor of the substrate (Baek et al., 2020). Therefore, the mechanism of ubiquitin transfer by an E3-ligase may partly relay on the conformational dynamic of the E3- substrate (Mittag et al., 2010; Mittag et al., 2008). In fact, when looking at other ubiquitylation substrates, degrons tend to be located within segments that are predicted to be intrinsically disordered as compared with the overall substrate structure (Guharoy et al., 2016). Degron flanking regions are often IDRs as well (Tompa & Fersht, 2009). It is likely that the mechanisms that we observed in this work, which include: *i*) IDR expansion, *ii*) allosteric modulation by IDRs and *iii*) fuzzy binding mode, may apply as well to other ubiquitylation substrates with IDRs as AUX/IAAs.

We also observed that the conformational heterogeneity of the auxin receptors is enhanced by the IDR length as shown by our CG-modeling. Here, the conformational space that IAA27 occupies when it binds to ASK1·TIR1 is obviously larger than that of IAA7, IAA12 and IAA1 due to its larger IDR region (**Figure 18B**). These results also put into perspective the conformational ensemble appearance of auxin receptors with other *At*AUX/IAAs that vary in sequence length going short (<199 amino acids), medium (200-300 amino acids) and long (>300 amino acids). The conformational heterogeneity of the auxin receptor complexes may further increase in bryophytes such as *Marchantia polymorpha* and *Physcomitrium patens* which carry AUX/IAAs with larger IDRs.

Overall, this study has evidenced that the conformational heterogeneity of auxin receptor complexes increases with larger disorder length having functional implications in binding strength, polyubiquitylation and complex topology (**Figure 16**, **Figure 17**, **Figure 18**).

## 4.4 The N-terminal IDR and PB1 of AUX/IAAs allosterically modulates auxin receptor complex ensemble

Our MST experiments showed that either truncation of the PB1 or a charge reversal mutation of the KR motif (K35D and R36D) in IAA7[BM3] reduces the binding affinity with ASK1·TIR1 (**Figure 16**). These results answer a long-standing question in auxin biology about how regions outside the degron motif influence the ensemble of the auxin receptor complex. Traditionally, RBA with [3H]-IAA were used to show how different combinations of auxin receptor change the affinity to auxin (Calderón Villalobos et al., 2012; Hellmuth & Calderón Villalobos, 2016). One limitation of this assay is that it only traces the affinity for [3H]-IAA directly and not the affinity between AUX/IAAs and TIR1/AFBs. The results presented in this dissertation show for the first time that the IDR upstream the degron and the PB1 of IAA7 allosterically enhance its interaction with TIR1. Thus, regions outside the degron interface potentiate the binding affinity towards ASK1·TIR1 and could also explain why the combination of IAA7 and ASK1·TIR1 show such a strong affinity to [3H]-IAA with a $K_d$ = 17±7.81 nM (Calderón Villalobos et al., 2012). Contrary to IAA7, IAA12 has a sixteen-fold lower binding affinity to [3H]-IAA with a $K_d$ = 270±54.09 nM (Calderón Villalobos et al., 2012). It has been long hypothesized that the differences in binding affinity observed between *e.g.* IAA7 and IAA12 depend on the flanking regions to the degron which are divergent in amino acid sequence composition. Since TIR1 top surface is highly electronegative (**Figure S12**), it is likely that positively charged residues may influence the binding affinity of AUX/IAAs with ASK1·TIR1, and consequently the affinity for auxin. However, sequence analyses do not reveal any clear difference in the physicochemical properties between IAA7 and IAA12. Both AUX/IAAs show a similarities general sequence parameters such as: in charge segregation, fraction of positively charged residues, fraction of negatively charged residues and hydropathy (Niemeyer et al., 2020). Nevertheless, our auxin-free CG-simulations showed that in the case of IAA7 both the IDR and PB1 contribute to ASK1·TIR1 binding, whilst IAA12 binding to ASK1·TIR1 occurs only at the IDR region. This highlights how sequences divergence not only at the IDR, but as well at the PB1 influence how AUX/IAAs bind to ASK1·TIR1. Additionally, it is likely that the AUX/IAA ensemble in the free state at the IDR region, may also influence how AUX/IAAs establish interactions with ASK1·TIR1. Interestingly, IAA12[BM3] is more compacted (CI=0.48) than IAA7[BM3] (CI=0.36) despite both having a similar sequence length and predicted disorder. Therefore, less

compacted AUX/IAAs like IAA7[BM3] with a larger exposed surface may facilitate the interaction with ASK1·TIR1 by exposing multiple binding interfaces including the KR motif, PB1 and the degron. Conversely, increased compaction may occlude or shield AUX/IAAs binding motif such as the degron, the KR and the PB1 decreasing the affinity with ASK1·TIR1.

## 4.5 AUX/IAAs intrinsic disorder across plant species

Our *in silico* sequence analysis across land plant species showed that AUX/IAAs length positively correlates with the number of predicted disorder residues (**Figure 20B**). Surprisingly, plant groups of lower complexity contain the longest AUX/IAAs, and as a result larger content of predicted disorder (**Figure 20D**). This opposes to the general trend in eukaryotes, where was proposed that long disorder regions are more abundant in organism of higher complexity (Pancsa & Tompa, 2012). A low level of IDR content may reflect adaptation to extreme conditions, or a nutrient-rich, stress-free intracellular environment, whereas an elevated IDR content indicates that the organism leads a varied lifestyle in which can change between habitats (e.g. host changing pathogens) (Pancsa & Tompa, 2012). Interestingly, the bryophytes group, which contains the longest AUX/IAAs exhibit a high environmental adaptability as habitats span from marked water (desert to aquatic) and temperature (tropical to artic) gradients being only behind the flowering plants (Rice, 2009). It is worth mentioning that the overall contribution of disorder of AUX/IAAs to the proteome is still larger in plants of higher complexity such as angiosperms as they carry multiple AUX/IAAs copies. Proteome-wide analysis with disorder prediction tools would be useful to establish if the trend observed in AUX/IAAs % of disorder is also true to the whole proteome of all land plants groups. This would allow to determine if overall the % of disorder in plants proteome correlates with their complexity, as is generally assumed for other higher eukaryotes.

The *in silico* analyses of AUX/IAAs across land plant species showed a larger content of predicted IDRs in plants of low complexity (**Figure 20D**). Low complexity plants typically contain a small set of AUX/IAA proteins. For example, in the bryophyte *Marchantia polymorpha* auxin controls multiple morphogenetic processes with one single *Mp*IAA (825 amino acids, 83.15% disordered) protein and one single *Mp*TIR1/AFB1 (Eklund et al., 2015; Flores-Sandoval, Eklund, & Bowman, 2015; Suzuki, Kato, Iwano, Nishihama, & Kohchi, 2023). An open question in the field is how a simplified auxin signaling pathway *e.g.* in *Marchantia polymorpha* can still control multiple cellular processes? It is likely that a tight protein regulation which is able to respond to multiple stimuli may optimize auxin response in *Marchantia polymorpha*. In this case, intrinsic disorder may have a more important role in *Mp*IAA regulation compared with AUX/IAAs in other species. Therefore,

a larger IDR content in *Mp*IAA may also increase the number of protein partners in enabling additional functions and regulation *in vivo*.

We observed that the region upstream the degron is highly variable in sequence length while the degron tail length is more preserved in AUX/IAAs of different land plant groups. This may indicate that selective pressure has constrained the degron tail length due to its tethering function of PB1 domain for binding to TIR1/AFBs. Previously, it was shown that an in-frame deletion of *Sisymbrium orientale* (*So*) IAA2 resulting in the loss of its nine residues degron tail decreased the binding affinity to *At*TIR1 and *At*AFB5 *in vitro* compared with *Os*IAA2 wild-type. This mutation also conferred resistance to the synthetic auxins 2,4-Dichlorophenoxyacetic acid (2,4-D) and dicamba *in vivo* (Figueiredo et al., 2022). It is likely that short degron tails will bring closer the degron to the PB1 domain, reducing degron exposure for TIR1 and auxin binding. Alternatively, too long degron tails would increase the distance between AUX/IAAs degron and the PB1 reducing the probability of the PB1 binding to TIR1. Taking all together, we propose that conservation of the degron tail length may be important for tethering functions of the PB1 during auxin receptor complex ensemble across different land plants.

# 5. Conclusion

The structural and molecular auxin binding mechanism has been dominated for more than a decade by the ASK1·TIR1·auxin·IAA7-degron crystal structure model (Tan et al., 2007). However, building evidence showed that the context of the degron within AUX/IAAs matters and it is the main reason of the difference auxin sensitivities and different AUX/IAAs degradation rate observed *in vitro* and *in vivo* (Calderón Villalobos et al., 2012; B. L. Moss et al., 2015; Niemeyer et al., 2020; Winkler et al., 2017). Given the fact that the degron of AUX/IAAs is located in an IDR, traditional structural techniques were unable to provide a complete understanding of the mechanism of auxin perception and the way that AUX/IAAs are polyubiquitylated. In this dissertation by applying integrative structural techniques, I unveiled different structural behaviors of AUX/IAAs that drive TIR1 binding for auxin perception and that drive AUX/IAAs polyubiquitylation. By structural characterizing AUX/IAAs with different IDRs length I could established that the IDR length of AUX/IAAs is inversely proportional to their compactness and to directly proportional to the size of their conformational ensemble. Moreover, I obtained data that provides experimental evidence about how IAA7 conformational ensemble changes from compact in the free state to expanded in the ASK1·TIR1-bound state. This expanded conformational ensemble of IAA7 allows multiple and transient interactions with ASK1·TIR1, which I propose to allosterically enhance the affinity between the three proteins. This was further supported by *in silico* simulations, which showed transient interactions of IAA7 with TIR1 top surface. Based on the literature this binding mode between IAA7 and ASK1·TIR1 can be classified as fuzzy. Furthermore, based on the *in silico* modeling, the N-terminal IDR upstream the degron remains highly heterogeneous in conformation. While the degron tail tethers the PB1 so it binds in different conformations to TIR1's top surface. Here, it is proposed that this binding mode may be common among AUX/IAAs of different plant land groups, which are also predicted to have an N-terminal IDR. Additionally, evolutionary constraints may have preserved the length of AUX/IAAs degron tail for its PB1 tethering function when AUX/IAAs are bound to TIR1. My work additionally allows to propose that the conformational heterogeneity of AUX/IAAs during auxin perception facilitates their polyubiquitylation by an SCF[TIR1]-E3 ligase in multiple lysine residues across the primary sequence. The IDR expansion combined with the IDR conformational heterogeneity in AUX/IAAs may bring closer multiple ubiquitylation sites to the active site of the SCF[TIR1]-E3 ligase. Finally, my results suggest that the binding mode proposed in this dissertation may be common for other ubiquitylation substrates in plants and other species which carry degrons flanked by IDRs. Overall, the binding mechanisms proposed in this dissertation bring a new biophysical and

biochemical understanding to the field about the mechanism that drive the formation of the auxin receptor complexes and the mechanisms of polyubiquitylation of disordered substrates.

# 6. Materials and methods

## 6.1 Protein cloning

All constructs of *At*AUX/IAAs were provided by the host lab in pGEX-4T-3 vector. Additionally, the *Pp*IAA1A and *Pp*IAA1B were cloned from cDNA donated by Annika Griess-Osowski at the IPB and extracted from *Physcomitrium patens* "Gransden" strains. *Pp*IAA1A and *Pp*IAA1B coding sequence were amplified with attachment (*att*) sites for insertion into a pDONR vector using BP clonase enzyme (Thermo Scientific). Subsequently, pDONR inserts were subcloned into a pGEX-4T-3 Gateway version using an LR clonase enzyme (Thermo Scientific).  For *At*IAA4, *At*IAA8, *At*IAA27, *Pp*IAA1A and *Pp*IAA1B the pGEX-4T-3 thrombin cleavage site was exchanged by Tobacco Etch Virus (TEV) cleavage site using a deletion PCR protocol (Pérez-Pinera, Menéndez-González, & Vega, 2006). Briefly, reverse and forward primers were designed to amplify the whole vector avoiding the thrombin cleavage site but containing the TEV cleavage site as overhangs. This cleavage site exchange was performed to avoid thrombin miscleavage observed in these set *At*AUX/IAAs. Gateway 5' *att* sites were also deleted using this protocol resulting in seamless *Pp*IAA1A and *Pp*IAA1B inserts.

## 6.2 Protein purification

ASK1·TIR1 complex was purified from Sf9 cells as described earlier (Tan et al., 2007) with minor changes. In brief, ASK1 was co-purified with GST-TIR1 using GSH affinity chromatography and anion chromatography in a Mono Q 5/50 GL followed by tag-removal and a final SEC step in an Increase 10/300 Superdex 200 pg using an ÄKTA FPLC system.

AUX/IAA proteins were expressed as GST-tagged proteins in *E. coli* and purified using GSH-agarose beads (SERVA) as described elsewhere (Niemeyer et al., 2020; Winkler et al., 2017). Briefly, GST-AUX/IAAs were immobilized in GSH-agarose beads for 30 min followed by GST tag removal applying an in-resin thrombin or TEV digestion step in 20 mM Tris-HCl pH 8.0, 200 mM NaCl. The supernatant containing the untagged AUX/IAA fractions were pooled and loaded either to a HiLoad™ 16/60 Superdex™ 75 pg or 200 pg SEC column with an ÄKTA FPLC system, pre-equilibrated and eluted with 10 mM KPi pH 7.8, 150 mM KF, 0.2 mM TCEP. For *At*IAA8 a cation exchange chromatography step was performed prior SEC to remove additional impurities, as follows; *At*IAA8 was eluted in 20 mM KPi pH 6.0, 5 mM DTT buffer with a linear gradient from 0.02 to 1 M of NaCl in a HiTrap SP HP column. Similarly, for *Pp*IAA1A and *Pp*IAA1B an anion exchange chromatography step was performed prior to the SEC to increase protein purity. Briefly,

*Pp*IAA1A and *Pp*IAA1B were eluted in 20 mM Tris-HCl pH 8.0, 0.5 mM DTT buffer applying a linear gradient from 0.02 to 1 M of NaCl in a Mono Q 5/50 GL column.

## 6.3 Protein fluorescent labeling and purification for smFRET and MST

Proteins were labeled with ATTO488 and ATTO594 as donor and acceptor pair following supplier's protocol (ATTO-TEC). Briefly, untagged GSH-agarose affinity purified IAA7[BM3] was concentrated to 1-1.5 mM in a 250-300 µL in solution C (20 parts of solution A [phosphate-buffered saline, pH 7.4] and 1 part of solution B [0.2 M sodium bicarbonate, pH 9.0]). The protein solution was mixed with 0.7 molar excess of maleimide-ATTO488 (ATTO-TEC) and incubated for one hour at room temperature. Free ATTO448 dye was removed by applying a cation exchange chromatography step in a HiTrap™ SP HP with an ÄKTA FPLC system. Fractions containing IAA7[BM3]-ATTO488 conjugates were pooled and concentrated to 250-300 µL volume in solution C and 1.0 molar excess of ATTO594 (ATTO-TEC) was added, followed by incubation for one hour at room temperature. Excess of ATTO594 was removed by applying a second cation chromatography step in a HiTrap SP HP with an ÄKTA FPLC system. For MST experiments, IAA7[BM3] was incubated with 1.5-2 molar excess of maleimide-ATTO488 and purified as described above. Detection of single and/or double-labeled IAA7[BM3] fractions was performed with a Typhoon FLA 9500 system using a 473 nm excitation wavelength and LPB filter for ATTO488 conjugates and 635 nm excitation wavelength and LPR filter for ATTO594 conjugates.

## 6.4 Liquid chromatography–mass spectrometry (LC-MS) for labeling detection

For the identification of labelled residues with targeted MS-analysis (parallel reaction monitoring, PRM), fluorescently labelled IAA7[BM3] protein was separated by SDS-PAGE and subjected to in-gel digestion with either Trypsin or GluC or both. Extracted and dried peptides were dissolved in 5% acetonitrile, 0.1% trifluoric acid and injected into an EASY-nLC 1200 liquid chromatography system (Thermo Fisher Scientific). Peptides were separated using liquid chromatography C18 reverse phase chemistry employing a 240 min gradient increasing from 1% to 38 % acetonitrile in 0.1% FA, and a flow rate of 250 nL/min. Eluted peptides were electrosprayed on-line into a Fusion Lumos Tribrid mass spectrometer (Thermo Fisher Scientific). The spray voltage was 2.0 kV and the capillary temperature 305°C. A full MS survey scan was carried out with chromatographic peak width set to 15 s, resolution 60,000, automatic gain control (AGC) set to standard and a max injection time (IT) of 100 ms. MS/MS peptide sequencing was performed

using a PRM scan strategy (without retention time scheduling) with HCD fragmentation containing target peptide m/z. Top 15 MS/MS scans were acquired in the Orbitrap with resolution 15,000, mass to charge ratios (m/z) between 150 and 2000, AGC target set to 300%, Maximum IT 22 ms, isolation width 1.6 m/z, and normalized collision energy 28%. MS/MS spectra were used to search the TAIR10 database (ftp://ftp.arabidopsis.org) amended with the protein sequence of the modified BM3 protein by the Mascot software v.2.7 linked to Proteome Discoverer v.2.1. The enzyme specificity was set to the respective enzyme(s) and up to five missed cleavages were tolerated. Carbamidomethylation of cysteine was set as a fixed modification and oxidation of methionine and Atto-488 or Atto-594 modification of cysteine were set as variable modifications. The precursor tolerance was set to 10 ppm and the product ion mass tolerance was set to 0.02 Da. A decoy database search was performed to determine the peptide spectral match (PSM) and peptide identification false discovery rates (FDR). The ptmRS module was used to specifically map ATTO modifications to amino acid residues within the primary structure of peptides, with standard settings except that PhosphoRS Mode was set to False.

## 6.5 Dynamic and static light scattering (DLS/SLS)

Simultaneous static and dynamic light scattering measurements were at a scattering angle of 90° in a custom-built apparatus, equipped with a diode-pumped continuous wave laser (Millennia IIs, Spectra-Physics) and a high quantum yield avalanche photodiode, has been described in detail (Gast, Nöppert, Müller-Frohne, Zirwer, & Damaschun, 1997). Instead of using a commercially available stopped-flow mixing device (Gast et al., 1997), manual mixing (dead time about 10 s) was preferred in the present work. Manual mixing ensures stable solution composition, particularly during long-term experiments. A primary data accumulation interval $T_{acc}$ = 8 s was used for all SLS and DLS experiments. $T_{acc}$ defines the time resolution that is consistent with the dead time and yields reasonable (short) time averages of the mean scattering intensity $I(T_{acc})$ and the time-autocorrelation function $ACF(T_{acc})$ of the fluctuations in the instantaneous scattering intensity. Hundreds of pairs of $I(T_{acc})$ and $ACF(T_{acc})$ were stored transiently before calculating kinetic and equilibrium. Translational diffusion coefficients D were obtained from the measured autocorrelation functions using the program CONTIN (Provencher, 1982). CONTIN yields intensity distribution functions I(D), which can be calculated without further assumptions concerning the morphology of the particles. Diffusion coefficients were converted into Stokes radii ($R_s$) via the Stokes-Einstein equation $Rs = k_B T/(6\pi\eta D)$, where $k_B$ is Boltzmann's constant, T is the temperature in Kelvin, and $\eta$ is the solvent viscosity. Viscosities were measured using an Ubbelohde-type viscometer (Viscoboy-2, Lauda, Germany).

Apparent molecular masses, $M_{app}$, were calculated from the relative excess scattering intensity, $I_{exc, rel}$ defined as $I_{exc, rel} = (I_{solution} - I_{solvent})/I_{reference}$, where $I_{solution}$, $I_{solvent}$ and $I_{reference}$ are the scattering intensities of solution, solvent, and reference scatterer (toluene, in our case), respectively. $M_{app}$ is related to $I_{exc,rel}$ by $M_{app} = k_{opt} \cdot I_{exc, rel}/c$, where c is the peptide concentration and $k_{opt}$ is an optical constant depending on physical quantities of the scattering experiment as scattering angle, wavelength, reference sample, refractive index n of the solution and refractive index increment (dn/dc) of the proteins. A (dn/dc) of 0.19 ml/g was used for all AUX/IAAs in their individual solvents. The size distribution obtained with CONTIN was additionally used to separate the scattering intensities in the association equilibrium from that of other scattering particles. To determine the oligomeric state of the AUX/IAA, we expressed the relative apparent molecular masses $M_{rel} = M_{app}/M_{mon}$. Where $M_{mon}$ is the monomer theoretical mass calculated from the amino acid sequence. The apparent molecular masses and $R_s$ were extrapolated to 0 dilution to obtain the relative molecular mass and $R_s$ respectively.

## 6.6 Crosslinking (XL) reactions and LC-MS analyses

Crosslinking reactions were carried out as described before in (Niemeyer et al., 2020) with minor modifications. Briefly, reactions containing 5 µM of ASK1·TIR1 and either 5 µM of IAA1[BM3] or IAA27[BM3] were pre-incubated at room temperature for 15 min in the presence or absence of 10 µM auxin (IAA) before addition of 1 mM DSBU (100 molar excess) (CF Plus Chemicals). Reactions were quenched by the addition of $NH_4HCO_3$ and urea. Samples were sonicated after addition of DTT and iodoacetamide, followed by overnight trypsin digestion at 37ºC stopped with 10% TFA. Upon centrifugation (5 min 14,000 x $g$), proteolytic peptide mixtures were analyzed by LC/MS/MS on an UltiMate 3000 RSLC nano-HPLC system coupled to an Orbitrap Q-Exactive Plus mass spectrometer (Thermo Fisher Scientific). Peptides were separated on reversed phase C18 columns (trapping column: Acclaim PepMap 100, 300 µm × 5 mm, 5 µm, 100 Å (Thermo Fisher Scientific); separation column: self-packed Picofrit nanospray C18 column, 75 µM × 250 mm, 1.9 µm, 80 Å, tip ID 10 µm (New Objective)) or µPAC™ 200 cm C18 (Pharmafluidics). After desalting the samples on the trapping column, peptides were eluted and separated using a linear gradient from 3% to 40% B (solvent A: 0.1% (v/v) formic acid in water, solvent B: 0.08% (v/v) formic acid in acetonitrile) with a constant flow rate of 300 nL/min over 90 min. Data were acquired in data-dependent MS/MS mode with stepped higher-energy collision-induced dissociation (HCD) and normalized collision energies of 27%, 30%, and 33%. Each high-resolution full scan ($m/z$ 375 to 1799, $R = 140,000$ at $m/z$ 200) in the orbitrap was followed by high-resolution product ion scans ($R = 17,500$) of the ten most intense signals in the full-scan mass spectrum (isolation window 2

Th); the target value of the automated gain control was set to 3,000,000 (MS) and 200,000 (MS/MS), maximum accumulation times were set to 100 ms (MS) and 250 ms (MS/MS) and the maximum cycle time was 5 s. Precursor ions with charge states <3+ and >8+ or were excluded from fragmentation. Dynamic exclusion was enabled (duration 60 s, window 3 ppm).

## 6.7 Data analysis of crosslinked (XL)-peptides

Data analysis was performed as before in (Niemeyer et al., 2020) with minor modifications. Mass spectrometric *.raw files were converted to mzML using Proteome Discoverer 2.0. MeroX analysis was performed with the following settings: Proteolytic cleavage: C-terminal at Lys (blocked as XL site) and Arg with max. 3 missed cleavages, peptides" length: 5 to 30, static modification: alkylation of Cys by IAA, variable modification: oxidation of M, crosslinker: DSBU with specificity towards Lys, Ser, Thr, Tyr, and N-termini, analysis mode: RISE-UP mode, precursor mass accuracy: 8 ppm, product ion mass accuracy: 12 ppm, signal-to-noise ratio: 1.5, precursor mass correction activated, prescore cutoff at 10% intensity, FDR cutoff: 1.0%, and minimum score cutoff: 50. All analyses included the cRAP database sequences. Decoy database was generated using shuffled sequences with kept protease sites.

## 6.8 Microscale thermophoresis (MST)

ASK1·TIR1 and IAA7$^{BM3}$/IAA7$^{K35D\_R36D}$/IAA7$^{\Delta PB1}$ binding affinities at increasing concentrations of IAA were analyzed by MST. IAA7$^{BM3}$, IAA7$^{K35D\_R36D}$ and IAA7$^{\Delta PB1}$ were labeled with maleimide-ATTO488 (ATTO-TEC) and purified as described above. MST experiments were carried out on a Monolith NT.115 Blue/Red system (NanoTemper Technologies). ASK1·TIR1 and IAA7-ATTO488 variants conjugates were incubated at 10 nM final concentration, respectively, at room temperature for 30 min in 20 mM Tris-HCl, pH 8.0, 200 mM NaCl, 0.05% (w/v) Tween 20 buffer with increasing concentrations of IAA and loaded into premium glass capillaries (MO-K025, NanoTemper Technologies). MST measurements were carried out with 40% MST power and 50% blue excitation power in three independent biological replicas (n=3). MST traces were analyzed in a MO.Affinity Analysis software (NanoTemper Technologies) at time point 5 s on time. Binding kinetic curves were expressed as fraction bound (FB):

$$FB = \frac{\Delta F_{\ norm}^{\ sample} - \Delta F_{\ norm}^{\ unboaund}}{\Delta F_{\ norm}^{\ bound} - \Delta F_{\ norm}^{\ unbound}}$$

68

where, $\Delta F\,^{sample}_{norm}$ is the normalized fluorescence value of each respective mix, $\Delta F\,^{unboaund}_{norm}$ is the normalized fluorescence value at the lowest concentration of the IAA, and $\Delta F^{bound}_{norm}$ is the normalized fluorescence value at highest concentration of the IAA (Plach, Grasser, & Schubert, 2017). Data was evaluated with GraphPad Prism v 5.04 and fitted using "one site total" preset.

## 6.9 Confocal fluorescence microscope

Fluorescence correlation spectroscopy (FCS) and single-molecule fluorescence burst experiments were conducted on a home-built confocal microscope equipped with a pulsed fiber laser (FemtoFiber pro TVIS, Toptica Photonics AG) operating at 488 nm and a repetition rate of 80 MHz, with the pulses being synchronized with a diode-based laser (LDH P-C-485B, Picoquant GmbH) operating at 485 nm and 20 MHz. A single-mode fiber (LMA-8, NKT Photonics) was used for spatial filtering and a 60X microscope objective (UPlanApo 60x/1.20W, Olympus) for excitation and fluorescence light collection. Dichroic beam splitters (ZT405/488/594/647rpc, ZT594rdc, Chroma Technology Corp.) and a polarizing beam splitter (CVI Laser Optics) were used to split the emission light and to guide it onto single-photon avalanche diodes (SPCM-AQRH-14-TR, Excelitas Technologies Corp.) with their active areas serving as confocal pinholes. Spectral filters allowed to set the spectral range for the donor channel (LP496, BP25/50) and the acceptor channel (LP615, BP629/56), all filters from Semrock Inc (IDEX Corp.). Pulses from the detectors were fed into a TCSPC board (MultiHarp 150, Picoquant GmbH) operating in the time- tagged time-resolved mode with 80 ps time resolution.

## 6.10 Single-molecule FRET measurements (smFRET)

The measurements were carried out with 50-100 pM of doubly labeled IAA7 either in the presence or absence of 10 μM IAA and/or 1 μM of ASK1·TIR1. For burst experiments, a pulsed-interleaved excitation scheme was used with the donor molecule being excited with 80 MHz and 50 μW and the acceptor with 20 MHz and 10 μW. Detected photons were sorted by their arrival times and with respect to a synchronization signal of 20 MHz. Fluorescence bursts were identified using two threshold criteria—one threshold for the integrated emission after donor excitation and one for emission on direct excitation of the acceptor—to select for molecules bearing both a donor and acceptor. The first threshold was applied to a sliding photon density average detected by either of the two detection channels, with consecutive positively selected photons combined into bursts. Photon bursts above a minimum threshold of 100 photons in total were chosen for FRET analysis and corrected for background counts, quantum yields of fluorescence, and quantum efficiency of

detection (including collection efficiency, filter transmission, spectral cross talk and detector efficiency). Averaging owing to conformational flexibility during transit through the focus was taken into consideration in the calculation of distances from energy transfer histograms using the integral

$$\langle E \rangle = \int P(r)E(r)dr,$$

Where $E(r) = 1/(1 + (r/R_0)^6)$ is the distance dependence of the energy transfer and $P(r)$ an excluded-volume probability distribution of the end-to-end distance given by (cite Edwards)

$$P(r) \sim 4\pi r^2 exp\left[-\frac{\left(r - \left(\frac{5}{3}\right)^{\frac{3}{3}}\left(\frac{v}{3\pi l}\right)^{\frac{1}{5}}L^{\frac{3}{5}}\right)^2}{\frac{20Ll}{27}}\right]$$

The values $v$ and $l$ were deduced from the distribution $p(R_{ee})$ by EOM modelling of the X-ray scattering profile of IAA7 with $v=0.01$ and $l =6.7$A for IAA7[BM3], see X-ray scattering section. The parameter L describes the contour length, L, with L=Nb where N the number of residues between the fluorescent markers and b the distance between two Cα atoms (b=0.38 nm). Finally, the obtained values of $R_{ee}^{FRET}$ were corrected for the lengths added by the linker at which the dye molecules are attached considering their length 10.7*b in total: $N = N_{protein} + N_{linker}$.

## 6.11 Fluorescence cross-correlation spectroscopy (FCCS) analysis for $R_S$ determination

The characteristic decay time of the translational diffusion was determined from the cross-correlation functions of the donor and the acceptor channel, $G(\tau)$, using the fitting function:

$$G(\tau) = \frac{1}{N}[1 - T + Texp(-\tau/\tau_T)]\left(1 + \left(\frac{\tau}{\tau_D}\right)^a\right)^{-1}\left(1 + S^2\left(\frac{\tau}{\tau_D}\right)^a\right)^{-1/2}$$

where $S$ and $a$ are system parameters describing the shape of the focal volume, $N$ is the average number of labeled molecules in the focal volume, and $\tau_D$ the average dwell time in the focus volume, being related to the inverse translational diffusion coefficient, $D$. Triplet blinking was parameterized by the triplet fraction, $T$, and triplet time, $\tau_T$. The hydrodynamic radius, $R_S^{FCCS}$ was determined using the Stokes-Einstein equation with: $R_S^{FCCS} = \frac{k_B T}{6\pi\eta D}$. $G(\tau)$ was normalized with respect to the average number of molecules in the focus volume, $G_n(t) = G(\tau) \times N$. The reference measurements were conducted with ATTO488 and ATTO594.

## 6.12 Small angle X-ray scattering (SAXS)

X-ray scattering experiments were performed in transmission mode using a SAXSLAB laboratory setup (Retro-F) equipped with an AXO microfocus X-ray source. The AXO multilayer X-ray optic (AXO Dresden GmbH, Dresden, Gemany) was used as a monochromator for Cu-$K_\alpha$ radiation ($\lambda$ = 0.154 nm). A two-dimensional detector (PILATUS3 R 300K; DECTRIS) was used to record the 2D scattering patterns.

SAXS experiments were conducted using refillable capillaries with an outer diameter of 1 mm (BioSAS JSP stage, SAXSLAB/Xenocs). The intensities were angular-averaged and plotted versus the scattering angle $q$. The measurements were performed at room temperature and corrected for background, transmission and sample geometry. The measurement times were 10 h. Subsequent EOM analysis (GAJOE - version 2.1) using default parameters of a pool size of 10000 conformations generated in disordered mode, ensemble size of max. 20 conformations and 100 iteration cycles, revealed the most probable distributions of the radius of gyration, $p(R_g)$, and the end-to-end distances, $p(R_{ee})$ (Tria et al., 2015)

## 6.13 *In vitro* reconstitution of Ub-conjugation (IVU) and LC-MS analyses of IVU reactions

*In vitro* ubiquitylation (IVU) reactions34 were prepared as follows: Two protein mixtures (mix A and mix B) were prepared in parallel. Mix A contained 50 µM ubiquitin (Ub; fluorescein-labeled UbS20C: UbK0; 4:1 mix), 0.2 µM 6xHis-UBA1 (E1) and 2 µM 6xHis-AtUBC8 (E2) in reaction buffer (30 mM Tris-HCl, pH 8.0, 100 mM NaCl, 2 mM DTT, 5 mM MgCl2, 1 µM ZnCl2, 2 mM ATP). Mix B contained 1 µM Cul1·RBX1, 1 µM ASK1·TIR1, and 5 µM AUX/IAA protein in reaction buffer. Mix B was aliquoted and supplemented with IAA to reach the indicated final concentration. Mixtures A and B were separately incubated for 5 or 10 min at 25 °C, respectively. Equal volumes of mix A and B were combined, aliquots were taken at specified time points, and reactions were stopped by denaturation in Laemmli buffer.

Three sets of IVUs, corresponding to three biological replicates, were performed on consecutive weeks using AUX/IAA proteins from different batch preparations. After 30 min, IVUs were stopped by denaturing with urea, reduced with DTT and alkylated with iodoacetamide. Trypsin digestion was carried out overnight at 37 °C. Upon quenching and desalting, peptides were separated using liquid chromatography C18 reverse phase chemistry and later electrosprayed on-line into a QExactive Plus mass spectrometer (Thermo Fisher Scientific). A Top20 DDA scan strategy with

HCD fragmentation was used for MS/MS peptide sequencing. Ubiquitylated residues on identified peptides were mapped using GG and LRGG signatures (as tolerated variable modifications) from using both the Mascot software v2.5.0 (Matrix Science) linked to Proteome Discoverer v1.4 (Thermo Fisher Scientific), and the MaxQuant software v1.5.0.0.

## 6.14 Circular dichroism (CD) measurements

CD spectra were recorded with a Jasco-815 spectropolarimeter (Jasco Instruments). AUX/IAAs variants were concentrated and adjusted to 2–5 µM in 10 mM $K_2HPO_4$/$KH_2PO_4$ pH 7.8, 150 mM KF, 0.2 mM TCEP. Protein solutions were measured in a 0.1 mm pathlength quartz cuvette at 25 °C. Thirty-two spectra were accumulated with a response of 8 s, 0.5 nm data pitch, 1 nm band width from 260 nm to 185 nm. Buffer signals were substrate and raw data was corrected by the protein concentration and number of peptide bonds. Data was expressed in terms of mean residual ellipticity.

## 6.15 AUX/IAAs protein sequence search

The AUX/IAA protein search was performed using hmmsearch locally (available at: http://hmmer.org/) or within the HMMER web service (Finn, Clements, & Eddy, 2011), in both cases with default parameters. The HMM profiles were built from alignments of AUXIAA protein sequences from *A. thaliana*, *Amborella trichopoda*, *Marchantia polymorpha* and used for the hmmsearch approach. The protein sequences were obtained from Phytozome (Goodstein et al., 2012), Ensembl (Howe et al., 2021), Fernbase (https://fernbase.org/), GigaDB (http://gigadb.org/), NCBI (Schoch et al., 2020) and UniProtKB (Consortium, 2022). To further expand our list of AUX/IAA protein sequences we also included sequences from the KEGGS Orthology list K14484 (Kanehisa, Sato, Kawashima, Furumichi, & Tanabe, 2016). All hits were filtered for the presence of a PB1 domain and, and sequences containing a B3 DNA-binding domain were excluded using the InterProScan 5 software package (version 5.52-86.0, 19) in order to eliminate ARF proteins who also share a PB1. The remaining sequences were further curated manually in order to avoid duplicated sequences due to the occurrence of splicing variants or partial sequences in the genome databases.

Within the bryophytes, lycophytes, ferns, gymnosperms, basal angiosperms as well as monocotyledons and eudicotyledons we chose the following 21 species as representatives of the major branches of the plant kingdom: *Marchantia polymorpha L.*, *Physcomitrium patens* (Hedw.) Mitt., *Selaginella moellendorffii* (Hieron.), *Azolla filiculoides* Lam., *Salvinia cucullata*, *Ceratopteris richardii* Brongn., *Ginkgo biloba* L., *Picea abies* (L.) H. Karst., *Amborella trichopoda* Baill., *Oryza*

*sativa* L. ssp. japonica, *Musa acuminata* Colla. subsp. malaccensis, *Nicotiana attenuata* Torr. ex S. Watson, *Solanum lycopersicum* L., *Glycine max* (L.) Merr., *Populus trichocarpa* Torr. & A. Gray ex. Hook., *Cleome violacea* L., *Carica papaya* L., *Brassica oleracea* L. var. oleracea, *Brassica rapa* L., *Eutrema salsugineum* (Pall.) Al-Shebaz & Warwick, *Capsella rubella* Reut., *Arabidopsis lyrata* (L.) O'Kane & Al-Shehbaz subsp. lyrata and *Arabidopsis thaliana* (L.) Heynh.

## 6.16 Course-grain (CG) simulation.

Simulations were carried out using the LAMMPS simulation engine using the default Mpipi parameters (Joseph et al., 2021). The Mpipi model is a coarse-grained, one-bead-per-residue model that was optimized explicitly for simulating intrinsically disordered regions (IDRs). The primary reason that we used one-bead-per-residue simulations was the sheer size of the system simulated (754 amino acids for ASK1·TIR1 and 168 or more residues for the AUX/IAAs). For our simulations, IDRs were modeled as flexible chains, while folded domains were modeled as fixed rigid bodies. To convert the atomistic structures to coarse-grained models, the location of the alpha carbon atoms was used to place each bead for each amino acid. Folded domain structures were determined as follows: AUX/IAA PB1 structures were predicted using AlphaFold2 using ColabFold with the following specifications: structures were ranked by pLDDT score, max_msa was set to 512:1024, use_turbo was set to True, num_models was set to 5, use_ptm was set to True, num_ensembles was set to 8, max_recycles was set to 3, is training was set to False, and num_samples was set to 1. For the AUX/IAA predicted IDRs, simulations started the IDRs such that amino acids were non-overlapping. For the ASK1·TIR1 structure, the structure was primarily based off of the previously reported crystal structure (Tan et al., 2007). However, this crystal structure lacked parts of ASK1 and TIR1. To fill in the missing amino acids, we generated a structure of ASK1·TIR1 using colabfold with parameters as described above for the AUX/IAAs. We then aligned the AF2-generated structure with the crystal structure in VMD and saved the coordinates of the missing amino acids such that we were able to include them in our final simulations. For all simulations, a 500Å-by-500Å box with periodic boundary conditions was used and the temperature was set to 300. For the 'auxin-free' simulations, twenty replicates of each simulation were carried out to reduce the variablity that results from the random placement of the AUX/IAA and ASK1·TIR1 in the box. For each replicate, 100,000,000 steps at 10 femtoseconds per step was simulated. The first 500,000 steps of every simulation were discarded to allow for simulation equilibration resulting in 99,500,000 steps used for analysis of each replicate. Coordinates from the simulation were saved at intervals of 10,000 steps. For the 'auxin-bound' simulations, the AUX/IAA GWPPV motif was fixed in same position as for IAA7-degron in the

ASK1·TIR1·auxin·IAA7(degron) crystal structure (Tan et al., 2007). Apart from these 5 residues, all other AUX/IAA residues were allowed to move freely as in the 'auxin-free' simulations. For the auxin-bound simulations, because there was minimal variability in the relative position of the AUX/IAA relative to the ASK1·TIR1 due to the constraints introduced for fixing the AUX/IAA GWPPV motif to ASK1·TIR1, only 3 replicates were carried out. For auxin-bound simulations, each replicate consisted of 200,000,000 steps where each step was ten femtoseconds apart. Similar to the auxin-free simulations, the first 500,000 steps of the simulation were discarded to allow for equilibration and coordinates of the simulation were recorded every 10,000 steps. For all simulations, the Python package SOURSOP was used for analysis, which is based in part on MDTraj (Lalmansingh, Keeley, Ruff, Pappu, & Holehouse, 2023; McGibbon et al., 2015). For contact frequency calculations, residues were 'in contact' if they were less than 10 Å apart from each other. Determination of residue contact was binary in that if a residue was within at least one residue of the other protein, it was considered 'in contact' for the calculation, as determined using the compute_contacts function in MDTraj.

## 6.17 Apparent mass and $R_S$ determination by SEC

The last SEC purification step for ASK1·TIR1 was used to determine the Stokes radius ($R_S^{SEC}$) in an Increase 10/300 Superdex 200 pg using an ÄKTA FPLC system. The column calibration was performed using gel filtration standards (Bio-Rad, Cat. #151-1901) plus bovine serum albumin (BSA) added to protein mix before the run. Stokes radii and protein masses from the globular known reference proteins were used to construct a linear curves from both parameters (Uversky, 1993). The $R_S^{SEC}$ and apparent mass of ASK1·TIR1 was calculated from the resulting calibration curve equation based on their retention volume.

# References

Abel, S., Nguyen, M. D., & Theologis, A. (1995). The PS-IAA4/5-like family of early auxin-inducible mRNAs in Arabidopsis thaliana. *J Mol Biol, 251*(4), 533-549. doi:10.1006/jmbi.1995.0454

Abel, S., & Theologis, A. (1996). Early Genes and Auxin Action. *Plant Physiol, 111*(1), 9-17. doi:10.1104/pp.111.1.9

Aebersold, R., Agar, J. N., Amster, I. J., Baker, M. S., Bertozzi, C. R., Boja, E. S., . . . Zhang, B. (2018). How many human proteoforms are there? *Nature Chemical Biology, 14*(3), 206-214. doi:10.1038/nchembio.2576

The Amborella genome and the evolution of flowering plants. (2013). *Science, 342*(6165), 1241089. doi:10.1126/science.1241089

Baek, K., Krist, D. T., Prabu, J. R., Hill, S., Klügel, M., Neumaier, L. M., . . . Schulman, B. A. (2020). NEDD8 nucleates a multivalent cullin-RING-UBE2D ubiquitin ligation assembly. *Nature, 578*(7795), 461-466. doi:10.1038/s41586-020-2000-y

Baker, N. A., Sept, D., Joseph, S., Holst, M. J., & McCammon, J. A. (2001). Electrostatics of nanosystems: Application to microtubules and the ribosome. *Proceedings of the National Academy of Sciences, 98*(18), 10037-10041. doi:doi:10.1073/pnas.181342398

Bandurski, R. S., & Schulze, A. (1977). Concentration of Indole-3-acetic Acid and Its Derivatives in Plants. *Plant Physiol, 60*(2), 211-213. doi:10.1104/pp.60.2.211

Banks, J. A., Nishiyama, T., Hasebe, M., Bowman, J. L., Gribskov, M., dePamphilis, C., . . . Grigoriev, I. V. (2011). The Selaginella Genome Identifies Genetic Changes Associated with the Evolution of Vascular Plants. *Science, 332*(6032), 960-963. doi:10.1126/science.1203810

Beh, L. Y., Colwell, L. J., & Francis, N. J. (2012). A core subunit of Polycomb repressive complex 1 is broadly conserved in function but not primary sequence. *Proceedings of the National Academy of Sciences, 109*(18), E1063-E1071. doi:10.1073/pnas.1118678109

Berleth, T., & Jürgens, G. (1993). The role of the monopteros gene in organising the basal body region of the Arabidopsis embryo. *Development, 118*(2), 575-587. doi:10.1242/dev.118.2.575

Bernadó, P., Mylonas, E., Petoukhov, M. V., Blackledge, M., & Svergun, D. I. (2007). Structural Characterization of Flexible Proteins Using Small-Angle X-ray Scattering. *Journal of the American Chemical Society, 129*(17), 5656-5664. doi:10.1021/ja069124n

Birol, M., & Melo, A. M. (2019). Untangling the Conformational Polymorphism of Disordered Proteins Associated With Neurodegeneration at the Single-Molecule Level. *Front Mol Neurosci, 12*, 309. doi:10.3389/fnmol.2019.00309

Boer, D. R., Freire-Rios, A., van den Berg, W. A., Saaki, T., Manfield, I. W., Kepinski, S., . . . Solano, R. (2014). Structural basis for DNA binding specificity by the auxin-dependent ARF transcription factors. *Cell, 156*(3), 577-589.

Bondos, S. E., Dunker, A. K., & Uversky, V. N. (2021). On the roles of intrinsically disordered proteins and regions in cell communication and signaling. *Cell Communication and Signaling, 19*(1), 88. doi:10.1186/s12964-021-00774-3

Borgia, A., Borgia, M. B., Bugge, K., Kissling, V. M., Heidarsson, P. O., Fernandes, C. B., . . . Schuler, B. (2018). Extreme disorder in an ultrahigh-affinity protein complex. *Nature, 555*(7694), 61-66. doi:10.1038/nature25762

Bowman, J. L., Kohchi, T., Yamato, K. T., Jenkins, J., Shu, S., Ishizaki, K., . . . Schmutz, J. (2017). Insights into Land Plant Evolution Garnered from the Marchantia polymorpha Genome. *Cell, 171*(2), 287-304.e215. doi:https://doi.org/10.1016/j.cell.2017.09.030

Brady, G. P., & Sharp, K. A. (1997). Entropy in protein folding and in protein—protein interactions. *Current Opinion in Structural Biology, 7*(2), 215-221. doi:https://doi.org/10.1016/S0959-440X(97)80028-0

Brodsky, S., Jana, T., Mittelman, K., Chapal, M., Kumar, D. K., Carmi, M., & Barkai, N. (2020). Intrinsically Disordered Regions Direct Transcription Factor In Vivo Binding Specificity. *Mol Cell, 79*(3), 459-471.e454. doi:https://doi.org/10.1016/j.molcel.2020.05.032

Calderón Villalobos, L. I., Lee, S., De Oliveira, C., Ivetac, A., Brandt, W., Armitage, L., . . . Estelle, M. (2012). A combinatorial TIR1/AFB-Aux/IAA co-receptor system for differential sensing of auxin. *Nat Chem Biol, 8*(5), 477-485. doi:10.1038/nchembio.926

Cao, S., Kang, S., Mao, H., Yao, J., Gu, L., & Zheng, N. (2022). Defining molecular glues with a dual-nanobody cannabidiol sensor. *Nature Communications, 13*(1), 815. doi:10.1038/s41467-022-28507-1

Cermakova, K., & Hodges, H. C. (2023). Interaction modules that impart specificity to disordered protein. *Trends in Biochemical Sciences, 48*(5), 477-490. doi:https://doi.org/10.1016/j.tibs.2023.01.004

Chance, M. R., Farquhar, E. R., Yang, S., Lodowski, D. T., & Kiselar, J. (2020). Protein Footprinting: Auxiliary Engine to Power the Structural Biology Revolution. *J Mol Biol, 432*(9), 2973-2984. doi:https://doi.org/10.1016/j.jmb.2020.02.011

Chapman, E. J., & Estelle, M. (2009). Mechanism of Auxin-Regulated Gene Expression in Plants. *Annual Review of Genetics, 43*(1), 265-285. doi:10.1146/annurev-genet-102108-134148

Cheng, C. Y., Krishnakumar, V., Chan, A. P., Thibaud-Nissen, F., Schobel, S., & Town, C. D. (2017). Araport11: a complete reannotation of the Arabidopsis thaliana reference genome. *Plant J, 89*(4), 789-804. doi:10.1111/tpj.13415

Choi, J.-M., Holehouse, A. S., & Pappu, R. V. (2020). Physical Principles Underlying the Complex Biology of Intracellular Phase Transitions. *Annual Review of Biophysics, 49*(1), 107-133. doi:10.1146/annurev-biophys-121219-081629

Consortium, T. U. (2022). UniProt: the Universal Protein Knowledgebase in 2023. *Nucleic Acids Research, 51*(D1), D523-D531. doi:10.1093/nar/gkac1052

Coskuner, O., & Uversky, V. N. (2019). Intrinsically disordered proteins in various hypotheses on the pathogenesis of Alzheimer's and Parkinson's diseases. *Prog Mol Biol Transl Sci, 166*, 145-223. doi:10.1016/bs.pmbts.2019.05.007

Craig, K. L., & Tyers, M. (1999). The F-box: a new motif for ubiquitin dependent proteolysis in cell cycle regulation and signal transduction. *Progress in Biophysics and Molecular Biology, 72*(3), 299-328. doi:https://doi.org/10.1016/S0079-6107(99)00010-3

Das, R. K., Huang, Y., Phillips, A. H., Kriwacki, R. W., & Pappu, R. V. (2016). Cryptic sequence features within the disordered protein p27Kip1 regulate cell cycle signaling. *Proceedings of the National Academy of Sciences, 113*(20), 5616-5621. doi:10.1073/pnas.1516277113

Davis, C., Spaller, B. L., & Matouschek, A. (2021). Mechanisms of substrate recognition by the 26S proteasome. *Current Opinion in Structural Biology, 67*, 161-169. doi:https://doi.org/10.1016/j.sbi.2020.10.010

de Vries, J., Fischer, A. M., Roettger, M., Rommel, S., Schluepmann, H., Bräutigam, A., . . . Gould, S. B. (2016). Cytokinin-induced promotion of root meristem size in the fern Azolla supports a shoot-like origin of euphyllophyte roots. *New Phytologist, 209*(2), 705-720. doi:https://doi.org/10.1111/nph.13630

Dinesh, D. C., Kovermann, M., Gopalswamy, M., Hellmuth, A., Calderón Villalobos, L. I. A., Lilie, H., . . . Abel, S. (2015). Solution structure of the PsIAA4 oligomerization domain reveals interaction modes for transcription factors in early auxin response. *Proceedings of the National Academy of Sciences, 112*(19), 6230-6235. doi:doi:10.1073/pnas.1424077112

Dreher, K. A., Brown, J., Saw, R. E., & Callis, J. (2006). The Arabidopsis Aux/IAA protein family has diversified in degradation and auxin responsiveness. *Plant Cell, 18*(3), 699-714. doi:10.1105/tpc.105.039172

Droc, G., Larivière, D., Guignon, V., Yahiaoui, N., This, D., Garsmeur, O., . . . Bocs, S. (2013). The Banana Genome Hub. *Database, 2013*, bat035. doi:10.1093/database/bat035

Dyla, M., & Kjaergaard, M. (2020). Intrinsically disordered linkers control tethered kinases via effective concentration. *Proceedings of the National Academy of Sciences, 117*(35), 21413-21419. doi:doi:10.1073/pnas.2006382117

Edwards, Y. J. K., Lobley, A. E., Pentony, M. M., & Jones, D. T. (2009). Insights into the regulation of intrinsically disordered proteins in the human proteome by analyzing sequence and gene expression data. *Genome Biology, 10*(5), R50. doi:10.1186/gb-2009-10-5-r50

Eklund, D. M., Ishizaki, K., Flores-Sandoval, E., Kikuchi, S., Takebayashi, Y., Tsukamoto, S., . . . Bowman, J. L. (2015). Auxin Produced by the Indole-3-Pyruvic Acid Pathway Regulates Development and Gemmae Dormancy in the Liverwort Marchantia polymorpha  *The Plant Cell, 27*(6), 1650-1669. doi:10.1105/tpc.15.00065

Evans, R., Ramisetty, S., Kulkarni, P., & Weninger, K. (2023). Illuminating Intrinsically Disordered Proteins with Integrative Structural Biology. *Biomolecules, 13*(1), 124.

Felli, I. C., Gonnelli, L., & Pierattelli, R. (2014). In-cell 13C NMR spectroscopy for the study of intrinsically disordered proteins. *Nature Protocols, 9*(9), 2005-2016. doi:10.1038/nprot.2014.124

Figueiredo, M. R. A. d., Küpper, A., Malone, J. M., Petrovic, T., Figueiredo, A. B. T. B. d., Campagnola, G., . . . Gaines, T. A. (2022). An in-frame deletion mutation in the degron tail of auxin coreceptor <i>IAA2</i> confers resistance to the herbicide 2,4-D in <i>Sisymbrium orientale</i>. *Proceedings of the National Academy of Sciences, 119*(9), e2105819119. doi:doi:10.1073/pnas.2105819119

Figueiredo, M. R. A. d., & Strader, L. C. (2022). Intrinsic and extrinsic regulators of Aux/IAA protein degradation dynamics. *Trends in Biochemical Sciences, 47*(10), 865-874. doi:https://doi.org/10.1016/j.tibs.2022.06.004

Finn, R. D., Clements, J., & Eddy, S. R. (2011). HMMER web server: interactive sequence similarity searching. *Nucleic Acids Res, 39*(Web Server issue), W29-37. doi:10.1093/nar/gkr367

Flores-Sandoval, E., Eklund, D. M., & Bowman, J. L. (2015). A Simple Auxin Transcriptional Response System Regulates Multiple Morphogenetic Processes in the Liverwort Marchantia polymorpha. *PLOS Genetics, 11*(5), e1005207. doi:10.1371/journal.pgen.1005207

Freire-Rios, A., Tanaka, K., Crespo, I., van der Wijk, E., Sizentsova, Y., Levitsky, V., . . . Weijers, D. (2020). Architecture of DNA elements mediating ARF transcription factor binding and auxin-responsive gene expression in *Arabidopsis*. *Proceedings of the National Academy of Sciences, 117*(39), 24557-24566. doi:doi:10.1073/pnas.2009554117

Frere, G. A., de Araujo, E. D., & Gunning, P. T. (2022). Emerging mechanisms of targeted protein degradation by molecular glues. *Methods Cell Biol, 169*, 1-26. doi:10.1016/bs.mcb.2022.01.001

Fukaki, H., Tameda, S., Masuda, H., & Tasaka, M. (2002). Lateral root formation is blocked by a gain-of-function mutation in the SOLITARY-ROOT/IAA14 gene of Arabidopsis. *Plant J, 29*(2), 153-168. doi:10.1046/j.0960-7412.2001.01201.x

Fuxreiter, M. (2018). Fuzziness in Protein Interactions-A Historical Perspective. *J Mol Biol, 430*(16), 2278-2287. doi:10.1016/j.jmb.2018.02.015

Fuxreiter, M. (2020a). Classifying the Binding Modes of Disordered Proteins. *Int J Mol Sci, 21*(22). doi:10.3390/ijms21228615

Fuxreiter, M. (2020b). Fuzzy protein theory for disordered proteins. *Biochem Soc Trans, 48*(6), 2557-2564. doi:10.1042/bst20200239

Gagne, J. M., Downes, B. P., Shiu, S. H., Durski, A. M., & Vierstra, R. D. (2002). The F-box subunit of the SCF E3 complex is encoded by a diverse superfamily of genes in Arabidopsis. *Proc Natl Acad Sci U S A, 99*(17), 11519-11524. doi:10.1073/pnas.162339999

Gast, K., & Fiedler, C. (2012). Dynamic and static light scattering of intrinsically disordered proteins. *Methods Mol Biol, 896*, 137-161. doi:10.1007/978-1-4614-3704-8_9

Gast, K., Nöppert, A., Müller-Frohne, M., Zirwer, D., & Damaschun, G. (1997). Stopped-flow dynamic light scattering as a method to monitor compaction during protein folding. *European Biophysics Journal, 25*(3), 211-219. doi:10.1007/s002490050033

González-Foutel, N. S., Glavina, J., Borcherds, W. M., Safranchik, M., Barrera-Vilarmau, S., Sagar, A., . . . Chemes, L. B. (2022). Conformational buffering underlies functional selection in intrinsically disordered protein regions. *Nat Struct Mol Biol, 29*(8), 781-790. doi:10.1038/s41594-022-00811-w

Goodstein, D. M., Shu, S., Howson, R., Neupane, R., Hayes, R. D., Fazo, J., . . . Rokhsar, D. S. (2012). Phytozome: a comparative platform for green plant genomics. *Nucleic Acids Res, 40*(Database issue), D1178-1186. doi:10.1093/nar/gkr944

Gray, W. M., Kepinski, S., Rouse, D., Leyser, O., & Estelle, M. (2001). Auxin regulates SCFTIR1-dependent degradation of AUX/IAA proteins. *Nature, 414*(6861), 271-276. doi:10.1038/35104500

Guan, R., Zhao, Y., Zhang, H., Fan, G., Liu, X., Zhou, W., . . . Chen, W. (2016). Draft genome of the living fossil Ginkgo biloba. *GigaScience, 5*(1), s13742-13016-10154-13741. doi:10.1186/s13742-016-0154-1

Guharoy, M., Bhowmick, P., Sallam, M., & Tompa, P. (2016). Tripartite degrons confer diversity and specificity on regulated protein degradation in the ubiquitin-proteasome system. *Nat Commun, 7*, 10239. doi:10.1038/ncomms10239

Guilfoyle, T. J. (2015). The PB1 Domain in Auxin Response Factor and Aux/IAA Proteins: A Versatile Protein Interaction Module in the Auxin Response. *The Plant Cell, 27*(1), 33-43. doi:10.1105/tpc.114.132753

Gupta, M. N., & Uversky, V. N. (2023). Chapter 10 - Role of plasticity and disorder in protein moonlighting: blurring of lines between biocatalysts and other biologically active proteins. In M. N. Gupta & V. N. Uversky (Eds.), *Structure and Intrinsic Disorder in Enzymology* (pp. 279-301): Academic Press.

Hadfi, K., Speth, V., & Neuhaus, G. (1998). Auxin-induced developmental patterns in Brassica juncea embryos. *Development, 125*(5), 879-887. doi:10.1242/dev.125.5.879

Hagen, G., & Guilfoyle, T. (2002). Auxin-responsive gene expression: genes, promoters and regulatory factors. *Plant Molecular Biology, 49*(3), 373-385. doi:10.1023/A:1015207114117

Hamann, T., Benkova, E., Bäurle, I., Kientz, M., & Jürgens, G. (2002). The Arabidopsis BODENLOS gene encodes an auxin response protein inhibiting MONOPTEROS-mediated embryo patterning. *Genes Dev, 16*(13), 1610-1615. doi:10.1101/gad.229402

Hamann, T., Mayer, U., & Jürgens, G. (1999). The auxin-insensitive bodenlos mutation affects primary root formation and apical-basal patterning in the Arabidopsis embryo. *Development, 126*(7), 1387-1395. doi:10.1242/dev.126.7.1387

Han, M., Park, Y., Kim, I., Kim, E.-H., Yu, T.-K., Rhee, S., & Suh, J.-Y. (2014). Structural basis for the auxin-induced transcriptional regulation by Aux/IAA17. *Proceedings of the National Academy of Sciences, 111*(52), 18613-18618. doi:doi:10.1073/pnas.1419525112

Hatos, A., Teixeira, J. M. C., Barrera-Vilarmau, S., Horvath, A., Tosatto, Silvio C. E., Vendruscolo, M., & Fuxreiter, M. (2023). FuzPred: a web server for the sequence-based prediction of the context-dependent binding modes of proteins. *Nucleic Acids Research, 51*(W1), W198-W206. doi:10.1093/nar/gkad214

Havens, K. A., Guseman, J. M., Jang, S. S., Pierre-Jerome, E., Bolten, N., Klavins, E., & Nemhauser, J. L. (2012). A Synthetic Approach Reveals Extensive Tunability of Auxin Signaling *Plant Physiol, 160*(1), 135-142. doi:10.1104/pp.112.202184

Hellmuth, A., & Calderón Villalobos, L. I. (2016). Radioligand Binding Assays for Determining Dissociation Constants of Phytohormone Receptors. *Methods Mol Biol, 1450*, 23-34. doi:10.1007/978-1-4939-3759-2_3

Howe, K. L., Achuthan, P., Allen, J., Allen, J., Alvarez-Jarreta, J., Amode, M. R., . . . Flicek, P. (2021). Ensembl 2021. *Nucleic Acids Res, 49*(D1), D884-d891. doi:10.1093/nar/gkaa942

Hraber, P., O'Maille, P. E., Silberfarb, A., Davis-Anderson, K., Generous, N., McMahon, B. H., & Fair, J. M. (2020). Resources to Discover and Use Short Linear Motifs in Viral Proteins. *Trends Biotechnol, 38*(1), 113-127. doi:10.1016/j.tibtech.2019.07.004

Hu, T. T., Pattyn, P., Bakker, E. G., Cao, J., Cheng, J.-F., Clark, R. M., . . . Guo, Y.-L. (2011). The Arabidopsis lyrata genome sequence and the basis of rapid genome size change. *Nature Genetics, 43*(5), 476-481. doi:10.1038/ng.807

Ihling, C. H., Piersimoni, L., Kipping, M., & Sinz, A. (2021). Cross-Linking/Mass Spectrometry Combined with Ion Mobility on a timsTOF Pro Instrument for Structural Proteomics. *Analytical Chemistry, 93*(33), 11442-11450. doi:10.1021/acs.analchem.1c01317

Jin, J., Ang, X. L., Shirogane, T., & Wade Harper, J. (2005). Identification of Substrates for F-Box Proteins. In *Methods in Enzymology* (Vol. 399, pp. 287-309): Academic Press.

Jing, H., Yang, X., Emenecker, R. J., Feng, J., Zhang, J., Figueiredo, M. R. A., . . . Zuo, J. (2023). Nitric oxide-mediated S-nitrosylation of IAA17 protein in intrinsically disordered region represses auxin signaling. *J Genet Genomics*. doi:10.1016/j.jgg.2023.05.001

Joseph, J. A., Reinhardt, A., Aguirre, A., Chew, P. Y., Russell, K. O., Espinosa, J. R., . . . Collepardo-Guevara, R. (2021). Physics-driven coarse-grained model for biomolecular phase separation with near-quantitative accuracy. *Nature Computational Science, 1*(11), 732-743. doi:10.1038/s43588-021-00155-3

Kanehisa, M., Sato, Y., Kawashima, M., Furumichi, M., & Tanabe, M. (2016). KEGG as a reference resource for gene and protein annotation. *Nucleic Acids Res, 44*(D1), D457-462. doi:10.1093/nar/gkv1070

Kato, H., Nishihama, R., Weijers, D., & Kohchi, T. (2018). Evolution of nuclear auxin signaling: lessons from genetic studies with basal land plants. *Journal of Experimental Botany, 69*(2), 291-301. doi:10.1093/jxb/erx267

Ke, J., Ma, H., Gu, X., Thelen, A., Brunzelle, J. S., Li, J., . . . Melcher, K. (2015). Structural basis for recognition of diverse transcriptional repressors by the TOPLESS family of corepressors. *Science Advances, 1*(6), e1500107. doi:doi:10.1126/sciadv.1500107

Kim, Sun H., Bahk, S., Nguyen, Nhan T., Pham, Minh Le A., Kadam, Ulhas S., Hong, Jong C., & Chung, Woo S. (2022). Phosphorylation of the auxin signaling transcriptional repressor IAA15 by MPKs is required for the suppression of root development under drought stress in Arabidopsis. *Nucleic Acids Research, 50*(18), 10544-10561. doi:10.1093/nar/gkac798

Kim, Y., Park, C., Cha, S., Han, M., Ryu, K.-S., & Suh, J.-Y. (2020). Determinants of PB1 Domain Interactions in Auxin Response Factor ARF5 and Repressor IAA17. *J Mol Biol, 432*(14), 4010-4022. doi:https://doi.org/10.1016/j.jmb.2020.04.007

Kipreos, E. T., & Pagano, M. (2000). The F-box protein family. *Genome Biology, 1*(5), reviews3002.3001. doi:10.1186/gb-2000-1-5-reviews3002

Korasick, D. A., Enders, T. A., & Strader, L. C. (2013). Auxin biosynthesis and storage forms. *Journal of Experimental Botany, 64*(9), 2541-2555. doi:10.1093/jxb/ert080

Korasick, D. A., Westfall, C. S., Lee, S. G., Nanao, M. H., Dumas, R., Hagen, G., . . . Strader, L. C. (2014). Molecular basis for AUXIN RESPONSE FACTOR protein interaction and the control of auxin response repression. *Proceedings of the National Academy of Sciences, 111*(14), 5427-5432. doi:10.1073/pnas.1400074111

Krönke, J., Udeshi, N. D., Narla, A., Grauman, P., Hurst, S. N., McConkey, M., . . . Ebert, B. L. (2014). Lenalidomide causes selective degradation of IKZF1 and IKZF3 in multiple myeloma cells. *Science, 343*(6168), 301-305. doi:10.1126/science.1244851

Kumar, M., Gouw, M., Michael, S., Sámano-Sánchez, H., Pancsa, R., Glavina, J., . . . Gibson, T. J. (2019). ELM—the eukaryotic linear motif resource in 2020. *Nucleic Acids Research, 48*(D1), D296-D306. doi:10.1093/nar/gkz1030

Lalmansingh, J. M., Keeley, A. T., Ruff, K. M., Pappu, R. V., & Holehouse, A. S. (2023). SOURSOP: A Python package for the analysis of simulations of intrinsically disordered proteins. *bioRxiv*. doi:10.1101/2023.02.16.528879

Lang, D., Ullrich, K. K., Murat, F., Fuchs, J., Jenkins, J., Haas, F. B., . . . Rensing, S. A. (2018). The Physcomitrella patens chromosome-scale assembly reveals moss genome structure and evolution. *Plant J, 93*(3), 515-533. doi:10.1111/tpj.13801

Lerner, E., Barth, A., Hendrix, J., Ambrose, B., Birkedal, V., Blanchard, S. C., . . . Weiss, S. (2021). FRET-based dynamic structural biology: Challenges, perspectives and an appeal for open-science practices. *eLife, 10*, e60416. doi:10.7554/eLife.60416

Li, F.-W., Brouwer, P., Carretero-Paulet, L., Cheng, S., de Vries, J., Delaux, P.-M., . . . Pryer, K. M. (2018). Fern genomes elucidate land plant evolution and cyanobacterial symbioses. *Nature Plants, 4*(7), 460-472. doi:10.1038/s41477-018-0188-8

Liu, C., Xu, Z., & Chua, N. H. (1993). Auxin Polar Transport Is Essential for the Establishment of Bilateral Symmetry during Early Plant Embryogenesis. *Plant Cell, 5*(6), 621-630. doi:10.1105/tpc.5.6.621

Liu, S., Liu, Y., Yang, X., Tong, C., Edwards, D., Parkin, I. A. P., . . . Paterson, A. H. (2014). The Brassica oleracea genome reveals the asymmetrical evolution of polyploid genomes. *Nature Communications, 5*(1), 3930. doi:10.1038/ncomms4930

Ljung, K., Bhalerao, R. P., & Sandberg, G. (2001). Sites and homeostatic control of auxin biosynthesis in Arabidopsis during vegetative growth. *The Plant Journal, 28*(4), 465-474. doi:https://doi.org/10.1046/j.1365-313X.2001.01173.x

Ljung, K., Hull, A. K., Celenza, J., Yamada, M., Estelle, M., Normanly, J., & Sandberg, G. r. (2005). Sites and Regulation of Auxin Biosynthesis in Arabidopsis Roots. *The Plant Cell, 17*(4), 1090-1104. doi:10.1105/tpc.104.029272

Long, J. A., Ohno, C., Smith, Z. R., & Meyerowitz, E. M. (2006). TOPLESS Regulates Apical Embryonic Fate in Arabidopsis. *Science, 312*(5779), 1520-1523. doi:10.1126/science.1123841

Long, J. A., Woody, S., Poethig, S., Meyerowitz, E. M., & Barton, M. K. (2002). Transformation of shoots into roots in Arabidopsis embryos mutant at the TOPLESS locus. *Development, 129*(12), 2797-2806. doi:10.1242/dev.129.12.2797

Luo, J., Zhou, J. J., & Zhang, J. Z. (2018). Aux/IAA Gene Family in Plants: Molecular Structure, Regulation, and Function. *Int J Mol Sci, 19*(1). doi:10.3390/ijms19010259

Marchant, D. B., Sessa, E. B., Wolf, P. G., Heo, K., Barbazuk, W. B., Soltis, P. S., & Soltis, D. E. (2019). The C-Fern (Ceratopteris richardii) genome: insights into plant genome evolution with the first partial homosporous fern genome assembly. *Scientific Reports, 9*(1), 18181. doi:10.1038/s41598-019-53968-8

Martin-Arevalillo, R., Nanao, M. H., Larrieu, A., Vinos-Poyo, T., Mast, D., Galvan-Ampudia, C., . . . Parcy, F. (2017). Structure of the *Arabidopsis* TOPLESS corepressor provides insight into the evolution of transcriptional repression. *Proceedings of the National Academy of Sciences, 114*(30), 8107-8112. doi:doi:10.1073/pnas.1703054114

Martin, E. W., & Mittag, T. (2018). Relationship of Sequence and Phase Separation in Protein Low-Complexity Regions. *Biochemistry, 57*(17), 2478-2487. doi:10.1021/acs.biochem.8b00008

Matyskiela, M. E., Clayton, T., Zheng, X., Mayne, C., Tran, E., Carpenter, A., . . . Chamberlain, P. P. (2020). Crystal structure of the SALL4-pomalidomide-cereblon-DDB1 complex. *Nat Struct Mol Biol, 27*(4), 319-322. doi:10.1038/s41594-020-0405-9

McGibbon, R. T., Beauchamp, K. A., Harrigan, M. P., Klein, C., Swails, J. M., Hernández, C. X., . . . Pande, V. S. (2015). MDTraj: A Modern Open Library for the Analysis of Molecular Dynamics Trajectories. *Biophys J, 109*(8), 1528-1532. doi:10.1016/j.bpj.2015.08.015

Michaelides, E. E. (2008). Entropy, order and disorder. *The Open Thermodynamics Journal, 2*(1).

Ming, R., Hou, S., Feng, Y., Yu, Q., Dionne-Laporte, A., Saw, J. H., . . . Alam, M. (2008). The draft genome of the transgenic tropical fruit tree papaya (Carica papaya Linnaeus). *Nature, 452*(7190), 991-996. doi:10.1038/nature06856

Mittag, T., Marsh, J., Grishaev, A., Orlicky, S., Lin, H., Sicheri, F., . . . Forman-Kay, J. D. (2010). Structure/function implications in a dynamic complex of the intrinsically disordered Sic1 with the Cdc4 subunit of an SCF ubiquitin ligase. *Structure, 18*(4), 494-506. doi:10.1016/j.str.2010.01.020

Mittag, T., Orlicky, S., Choy, W.-Y., Tang, X., Lin, H., Sicheri, F., . . . Forman-Kay, J. D. (2008). Dynamic equilibrium engagement of a polyvalent ligand with a single-site receptor. *Proceedings of the National Academy of Sciences, 105*(46), 17772-17777. doi:10.1073/pnas.0809222105

Mohan, A., Oldfield, C. J., Radivojac, P., Vacic, V., Cortese, M. S., Dunker, A. K., & Uversky, V. N. (2006). Analysis of molecular recognition features (MoRFs). *J Mol Biol, 362*(5), 1043-1059. doi:10.1016/j.jmb.2006.07.087

Morris, J. G. (1974). THERMODYNAMICS OF BIOLOGICAL PROCESSES. *British Journal of Anaesthesia, 46*(3), 210-216. doi:https://doi.org/10.1093/bja/46.3.210

Morris, O. M., Torpey, J. H., & Isaacson, R. L. (2021). Intrinsically disordered proteins: modes of binding with emphasis on disordered domains. *Open Biology, 11*(10), 210222. doi:doi:10.1098/rsob.210222

Moss, B. L., Mao, H., Guseman, J. M., Hinds, T. R., Hellmuth, A., Kovenock, M., . . . Nemhauser, J. L. (2015). Rate Motifs Tune Auxin/Indole-3-Acetic Acid Degradation Dynamics. *Plant Physiol, 169*(1), 803-813. doi:10.1104/pp.15.00587

Moss, B. L., Mao, H., Guseman, J. M., Hinds, T. R., Hellmuth, A., Kovenock, M., . . . Nemhauser, J. L. (2015). Rate Motifs Tune Auxin/Indole-3-Acetic Acid Degradation Dynamics *Plant Physiol, 169*(1), 803-813. doi:10.1104/pp.15.00587

Mutte, S. K., Kato, H., Rothfels, C., Melkonian, M., Wong, G. K.-S., & Weijers, D. (2018). Origin and evolution of the nuclear auxin response system. *eLife, 7*, e33399. doi:10.7554/eLife.33399

Mutte, S. K., & Weijers, D. (2020). Deep Evolutionary History of the Phox and Bem1 (PB1) Domain Across Eukaryotes. *Scientific Reports, 10*(1), 3797. doi:10.1038/s41598-020-60733-9

Nagpal, P., Walker, L. M., Young, J. C., Ami, S., Candace, T., Estelle, M., & Reed, J. W. (2000). AXR2 Encodes a Member of the Aux/IAA Protein Family. *Plant Physiol, 123*(2), 563-573.

Nemhauser, J. L. (2018). Back to basics: what is the function of an Aux/IAA in auxin response? *New Phytologist, 218*(4), 1295-1297. doi:https://doi.org/10.1111/nph.15172

Newberry, R. W., & Raines, R. T. (2019). Secondary Forces in Protein Folding. *ACS Chemical Biology, 14*(8), 1677-1686. doi:10.1021/acschembio.9b00339

Niemeyer, M., Moreno Castillo, E., Ihling, C. H., Iacobucci, C., Wilde, V., Hellmuth, A., . . . Calderón Villalobos, L. I. A. (2020). Flexibility of intrinsically disordered degrons in AUX/IAA proteins reinforces auxin co-receptor assemblies.

Nishimura, K., Fukagawa, T., Takisawa, H., Kakimoto, T., & Kanemaki, M. (2009). An auxin-based degron system for the rapid depletion of proteins in nonplant cells. *Nature Methods, 6*(12), 917-922. doi:10.1038/nmeth.1401

Nystedt, B., Street, N. R., Wetterbom, A., Zuccolo, A., Lin, Y.-C., Scofield, D. G., . . . Jansson, S. (2013). The Norway spruce genome sequence and conifer genome evolution. *Nature, 497*(7451), 579-584. doi:10.1038/nature12211

Orlicky, S., Tang, X., Willems, A., Tyers, M., & Sicheri, F. (2003). Structural Basis for Phosphodependent Substrate Selection and Orientation by the SCFCdc4 Ubiquitin Ligase. *Cell, 112*(2), 243-256. doi:https://doi.org/10.1016/S0092-8674(03)00034-5

Ouyang, S., Zhu, W., Hamilton, J., Lin, H., Campbell, M., Childs, K., . . . Buell, C. R. (2007). The TIGR Rice Genome Annotation Resource: improvements and new features. *Nucleic Acids Res, 35*(Database issue), D883-887. doi:10.1093/nar/gkl976

Overvoorde, P. J., Okushima, Y., Alonso, J. M., Chan, A., Chang, C., Ecker, J. R., . . . Theologis, A. (2005). Functional Genomic Analysis of the AUXIN/INDOLE-3-ACETIC ACID Gene Family Members in Arabidopsis thaliana [W]. *The Plant Cell, 17*(12), 3282-3300. doi:10.1105/tpc.105.036723

Paciorek, T., Zažímalová, E., Ruthardt, N., Petrášek, J., Stierhof, Y.-D., Kleine-Vehn, J., . . . Geldner, N. (2005). Auxin inhibits endocytosis and promotes its own efflux from cells. *Nature, 435*(7046), 1251-1256.

Pancsa, R., & Tompa, P. (2012). Structural Disorder in Eukaryotes. *PLoS One, 7*(4), e34687. doi:10.1371/journal.pone.0034687

Paponov, I. A., Teale, W., Lang, D., Paponov, M., Reski, R., Rensing, S. A., & Palme, K. (2009). The evolution of nuclear auxin signalling. *BMC Evolutionary Biology, 9*(1), 126. doi:10.1186/1471-2148-9-126

Pérez-Pinera, P., Menéndez-González, M., & Vega, J. A. (2006). Deletion of DNA sequences of using a polymerase chain reaction based approach. *Electronic Journal of Biotechnology, 9*, 0-0.

Petzold, G., Fischer, E. S., & Thomä, N. H. (2016). Structural basis of lenalidomide-induced CK1α degradation by the CRL4(CRBN) ubiquitin ligase. *Nature, 532*(7597), 127-130. doi:10.1038/nature16979

Pietrosemoli, N., García-Martín, J. A., Solano, R., & Pazos, F. (2013). Genome-wide analysis of protein disorder in Arabidopsis thaliana: implications for plant environmental adaptation. *PLoS One, 8*(2), e55524. doi:10.1371/journal.pone.0055524

Plach, M. G., Grasser, K. D., & Schubert, T. (2017). MicroScale Thermophoresis as a Tool to Study Protein-peptide Interactions in the Context of Large Eukaryotic Protein Complexes. *Bio-protocol, 7*(23), e2632. doi:10.21769/BioProtoc.2632

Powers, S. K., Holehouse, A. S., Korasick, D. A., Schreiber, K. H., Clark, N. M., Jing, H., . . . Strader, L. C. (2019). Nucleo-cytoplasmic Partitioning of ARF Proteins Controls Auxin Responses in Arabidopsis thaliana. *Mol Cell, 76*(1), 177-190.e175. doi:10.1016/j.molcel.2019.06.044

Provencher, S. W. (1982). CONTIN: A general purpose constrained regularization program for inverting noisy linear algebraic and integral equations. *Computer Physics Communications, 27*(3), 229-242. doi:https://doi.org/10.1016/0010-4655(82)90174-6

Ramans-Harborough, S., Kalverda, A. P., Manfield, I. W., Thompson, G. S., Kieffer, M., Uzunova, V., . . . Kepinski, S. (2023). Intrinsic disorder and conformational coexistence in auxin coreceptors. *Proceedings of the National Academy of Sciences, 120*(40), e2221286120. doi:10.1073/pnas.2221286120

Ramos, J. A., Zenser, N., Leyser, O., & Callis, J. (2001). Rapid degradation of auxin/indoleacetic acid proteins requires conserved amino acids of domain II and is proteasome dependent. *Plant Cell, 13*(10), 2349-2360. doi:10.1105/tpc.010244

Rice, S. K. (2009). Mosses (Bryophytes). In G. E. Likens (Ed.), *Encyclopedia of Inland Waters* (pp. 88-96). Oxford: Academic Press.

Ruegger, M., Dewey, E., Gray, W. M., Hobbie, L., Turner, J., & Estelle, M. (1998). The TIR1 protein of Arabidopsis functions in auxin response and is related to human SKP2 and yeast grr1p. *Genes Dev, 12*(2), 198-207. doi:10.1101/gad.12.2.198

Sato, S., Tabata, S., Hirakawa, H., Asamizu, E., Shirasawa, K., Isobe, S., . . . Universitat Pompeu, F. (2012). The tomato genome sequence provides insights into fleshy fruit evolution. *Nature, 485*(7400), 635-641. doi:10.1038/nature11119

Schmidt, M. W., McQuary, P. R., Wee, S., Hofmann, K., & Wolf, D. A. (2009). F-box-directed CRL complex assembly and regulation by the CSN and CAND1. *Mol Cell, 35*(5), 586-597. doi:10.1016/j.molcel.2009.07.024

Schoch, C. L., Ciufo, S., Domrachev, M., Hotton, C. L., Kannan, S., Khovanskaya, R., . . . Karsch-Mizrachi, I. (2020). NCBI Taxonomy: a comprehensive update on curation, resources and tools. *Database (Oxford), 2020.* doi:10.1093/database/baaa062

Sharma, R., Raduly, Z., Miskei, M., & Fuxreiter, M. (2015). Fuzzy complexes: Specific binding without complete folding. *FEBS Letters, 589*(19PartA), 2533-2542. doi:https://doi.org/10.1016/j.febslet.2015.07.022

Shen, C., Wang, S., Bai, Y., Wu, Y., Zhang, S., Chen, M., . . . Qi, Y. (2010). Functional analysis of the structural domain of ARF proteins in rice (Oryza sativa L.). *Journal of Experimental Botany, 61*(14), 3971-3981. doi:10.1093/jxb/erq208

Shim, K. H., Kang, M. J., Youn, Y. C., An, S. S. A., & Kim, S. (2022). Alpha-synuclein: a pathological factor with Aβ and tau and biomarker in Alzheimer's disease. *Alzheimers Res Ther, 14*(1), 201. doi:10.1186/s13195-022-01150-0

Shimizu-Mitao, Y., & Kakimoto, T. (2014). Auxin Sensitivities of All Arabidopsis Aux/IAAs for Degradation in the Presence of Every TIR1/AFB. *Plant and Cell Physiology, 55*(8), 1450-1459. doi:10.1093/pcp/pcu077

Sigurd Ramans, H., Arnout, P. K., Gary, S. T., Martin, K., Martin, K., Mussa, Q., . . . Stefan, K. (2019). A fuzzy encounter complex precedes formation of the fully-engaged TIR1-Aux/IAA auxin co-receptor system. *bioRxiv*, 781922. doi:10.1101/781922

Skaar, J. R., Pagan, J. K., & Pagano, M. (2013). Mechanisms and function of substrate recruitment by F-box proteins. *Nat Rev Mol Cell Biol, 14*(6), 369-381. doi:10.1038/nrm3582

Skoog, F., & Miller, C. O. (1957). Chemical regulation of growth and organ formation in plant tissues cultured in vitro. *Symp Soc Exp Biol, 11*, 118-130.

Slotte, T., Hazzouri, K. M., Ågren, J. A., Koenig, D., Maumus, F., Guo, Y.-L., . . . Wright, S. I. (2013). The Capsella rubella genome and the genomic consequences of rapid mating system evolution. *Nature Genetics, 45*(7), 831-835. doi:10.1038/ng.2669

Soto, C., & Pritzkow, S. (2018). Protein misfolding, aggregation, and conformational strains in neurodegenerative diseases. *Nature Neuroscience, 21*(10), 1332-1340. doi:10.1038/s41593-018-0235-9

Su, L., Zhang, T., Yang, B., Dong, T., Liu, X., Bai, Y., . . . Cheng, Z.-M. (2023). Different evolutionary patterns of TIR1/AFBs and AUX/IAAs and their implications for the morphogenesis of land plants. *BMC Plant Biology, 23*(1), 265. doi:10.1186/s12870-023-04253-4

Suzuki, H., Kato, H., Iwano, M., Nishihama, R., & Kohchi, T. (2023). Auxin signaling is essential for organogenesis but not for cell survival in the liverwort Marchantia polymorpha. *The Plant Cell, 35*(3), 1058-1075. doi:10.1093/plcell/koac367

Szemenyei, H., Hannon, M., & Long, J. A. (2008). TOPLESS Mediates Auxin-Dependent Transcriptional Repression During Arabidopsis Embryogenesis. *Science, 319*(5868), 1384-1386. doi:10.1126/science.1151461

Tan, X., Calderón-Villalobos, L. I., Sharon, M., Zheng, C., Robinson, C. V., Estelle, M., & Zheng, N. (2007). Mechanism of auxin perception by the TIR1 ubiquitin ligase. *Nature, 446*(7136), 640-645. doi:10.1038/nature05731

Tatematsu, K., Kumagai, S., Muto, H., Sato, A., Watahiki, M. K., Harper, R. M., . . . Yamamoto, K. T. (2004). MASSUGU2 Encodes Aux/IAA19, an Auxin-Regulated Protein That Functions Together with the Transcriptional Activator NPH4/ARF7 to Regulate Differential Growth Responses of Hypocotyl and Formation of Lateral Roots in Arabidopsis thaliana. *The Plant Cell, 16*(2), 379-393. doi:10.1105/tpc.018630

Thomasen, F. E., & Lindorff-Larsen, K. (2022). Conformational ensembles of intrinsically disordered proteins and flexible multidomain proteins. *Biochem Soc Trans, 50*(1), 541-554. doi:10.1042/bst20210499

Tian, Q., Nagpal, P., & Reed, J. W. (2003). Regulation of Arabidopsis SHY2/IAA3 protein turnover. *The Plant Journal, 36*(5), 643-651. doi:https://doi.org/10.1046/j.1365-313X.2003.01909.x

Tian, Q., Uhlir, N. J., & Reed, J. W. (2002). Arabidopsis SHY2/IAA3 Inhibits Auxin-Regulated Gene Expression. *The Plant Cell, 14*(2), 301-319. doi:10.1105/tpc.010283

Timpte, C., Wilson, A. K., & Estelle, M. (1994). The axr2-1 mutation of Arabidopsis thaliana is a gain-of-function mutation that disrupts an early step in auxin response. *Genetics, 138*(4), 1239-1249. doi:10.1093/genetics/138.4.1239

Tiwari, S. B., Hagen, G., & Guilfoyle, T. (2003). The roles of auxin response factor domains in auxin-responsive transcription. *Plant Cell, 15*(2), 533-543. doi:10.1105/tpc.008417

Tiwari, S. B., Hagen, G., & Guilfoyle, T. J. (2004). Aux/IAA proteins contain a potent transcriptional repression domain. *Plant Cell, 16*(2), 533-543. doi:10.1105/tpc.017384

Tiwari, S. B., Wang, X. J., Hagen, G., & Guilfoyle, T. J. (2001). AUX/IAA proteins are active repressors, and their stability and activity are modulated by auxin. *Plant Cell, 13*(12), 2809-2822. doi:10.1105/tpc.010289

Tomita, T., & Matouschek, A. (2019). Substrate selection by the proteasome through initiation regions. *Protein Sci, 28*(7), 1222-1232. doi:10.1002/pro.3642

Tompa, P., & Fersht, A. (2009). *Structure and Function of Intrinsically Disordered Proteins* (1ST Edition ed.).

Toseland, C. P. (2013). Fluorescent labeling and modification of proteins. *J Chem Biol, 6*(3), 85-95. doi:10.1007/s12154-013-0094-5

Tria, G., Mertens, H. D., Kachala, M., & Svergun, D. I. (2015). Advanced ensemble modelling of flexible macromolecules using X-ray solution scattering. *IUCrJ, 2*(Pt 2), 207-217. doi:10.1107/s205225251500202x

Trivedi, R., & Nagarajaram, H. A. (2022). Intrinsically Disordered Proteins: An Overview. *International Journal of Molecular Sciences, 23*(22), 14050.

Tuskan, G. A., Difazio, S., Jansson, S., Bohlmann, J., Grigoriev, I., Hellsten, U., . . . Rokhsar, D. (2006). The genome of black cottonwood, Populus trichocarpa (Torr. & Gray). *Science, 313*(5793), 1596-1604. doi:10.1126/science.1128691

Uversky, V. N. (1993). Use of fast protein size-exclusion liquid chromatography to study the unfolding of proteins which denature through the molten globule. *Biochemistry, 32*(48), 13288-13298. doi:10.1021/bi00211a042

Uversky, V. N. (2019). Intrinsically Disordered Proteins and Their "Mysterious" (Meta)Physics. *Frontiers in Physics, 7.* doi:10.3389/fphy.2019.00010

Uversky, V. N., Santambrogio, C., Brocca, S., & Grandori, R. (2012). Length-dependent compaction of intrinsically disordered proteins. *FEBS Letters, 586*(1), 70-73. doi:https://doi.org/10.1016/j.febslet.2011.11.026

Vacic, V., Oldfield, C. J., Mohan, A., Radivojac, P., Cortese, M. S., Uversky, V. N., & Dunker, A. K. (2007). Characterization of Molecular Recognition Features, MoRFs, and Their Binding Partners. *Journal of Proteome Research, 6*(6), 2351-2366. doi:10.1021/pr0701411

Valliyodan, B., Cannon, S. B., Bayer, P. E., Shu, S., Brown, A. V., Ren, L., . . . Nguyen, H. T. (2019). Construction and comparison of three reference-quality genome assemblies for soybean. *The Plant Journal, 100*(5), 1066-1082. doi:https://doi.org/10.1111/tpj.14500

van der Lee, R., Buljan, M., Lang, B., Weatheritt, R. J., Daughdrill, G. W., Dunker, A. K., . . . Babu, M. M. (2014). Classification of Intrinsically Disordered Regions and Proteins. *Chemical Reviews, 114*(13), 6589-6631. doi:10.1021/cr400525m

Van Roey, K., Uyar, B., Weatheritt, R. J., Dinkel, H., Seiler, M., Budd, A., . . . Davey, N. E. (2014). Short Linear Motifs: Ubiquitous and Functionally Diverse Protein Interaction Modules Directing Cell Regulation. *Chemical Reviews, 114*(13), 6733-6778. doi:10.1021/cr400585q

Wang, J., Yan, D.-W., Yuan, T.-T., Gao, X., & Lu, Y.-T. (2013). A gain-of-function mutation in IAA8 alters Arabidopsis floral organ development by change of jasmonic acid level. *Plant Molecular Biology, 82*(1), 71-83. doi:10.1007/s11103-013-0039-y

Wang, X., Wang, H., Wang, J., Sun, R., Wu, J., Liu, S., . . . The Brassica rapa Genome Sequencing Project, C. (2011). The genome of the mesopolyploid crop species Brassica rapa. *Nature Genetics, 43*(10), 1035-1039. doi:10.1038/ng.919

Weijers, D., Benkova, E., Jäger, K. E., Schlereth, A., Hamann, T., Kientz, M., . . . Jürgens, G. (2005). Developmental specificity of auxin response by pairs of ARF and Aux/IAA transcriptional regulators. *Embo j, 24*(10), 1874-1885. doi:10.1038/sj.emboj.7600659

Winkler, M., Niemeyer, M., Hellmuth, A., Janitza, P., Christ, G., Samodelov, S. L., . . . Calderón Villalobos, L. I. A. (2017). Variation in auxin sensing guides AUX/IAA transcriptional repressor ubiquitylation and destruction. *Nature Communications, 8*(1), 15706. doi:10.1038/ncomms15706

Wolff, M., Schüler, A., Gast, K., Seckler, R., Evers, A., Pfeiffer-Marek, S., . . . Thalhammer, A. (2020). Self-Assembly of Exendin-4-Derived Dual Peptide Agonists is Mediated by Acylation and Correlated to the Length of Conjugated Fatty Acyl Chains. *Molecular Pharmaceutics, 17*(3), 965-978. doi:10.1021/acs.molpharmaceut.9b01195

Wright, P. E., & Dyson, H. J. (2015). Intrinsically disordered proteins in cellular signalling and regulation. *Nature Reviews Molecular Cell Biology, 16*(1), 18-29. doi:10.1038/nrm3920

Wu, W., Liu, Y., Wang, Y., Li, H., Liu, J., Tan, J., . . . Ma, H. (2017). Evolution Analysis of the Aux/IAA Gene Family in Plants Shows Dual Origins and Variable Nuclear Localization Signals. *Int J Mol Sci, 18*(10). doi:10.3390/ijms18102107

Xu, S., Brockmöller, T., Navarro-Quezada, A., Kuhl, H., Gase, K., Ling, Z., . . . Baldwin, I. T. (2017). Wild tobacco genomes reveal the evolution of nicotine biosynthesis. *Proceedings of the National Academy of Sciences, 114*(23), 6133-6138. doi:10.1073/pnas.1700073114

Yang, R., Jarvis, D. E., Chen, H., Beilstein, M. A., Grimwood, J., Jenkins, J., . . . Wang, X. (2013). The Reference Genome of the Halophytic Plant Eutrema salsugineum. *Front Plant Sci, 4*, 46. doi:10.3389/fpls.2013.00046

Yee, A. A., Semesi, A., Garcia, M., & Arrowsmith, C. H. (2014). Screening proteins for NMR suitability. *Methods Mol Biol, 1140*, 169-178. doi:10.1007/978-1-4939-0354-2_13

Yesbolatova, A., Saito, Y., Kitamoto, N., Makino-Itou, H., Ajima, R., Nakano, R., . . . Kanemaki, M. T. (2020). The auxin-inducible degron 2 technology provides sharp degradation control in yeast, mammalian cells, and mice. *Nature Communications, 11*(1), 5701. doi:10.1038/s41467-020-19532-z

Zhang, J., Liu, S., Shang, Z., Shi, L., & Yun, J. (2012). Analysis of the relationship between end-to-end distance and activity of single-chain antibody against colorectal carcinoma. *Theor Biol Med Model, 9*, 38. doi:10.1186/1742-4682-9-38
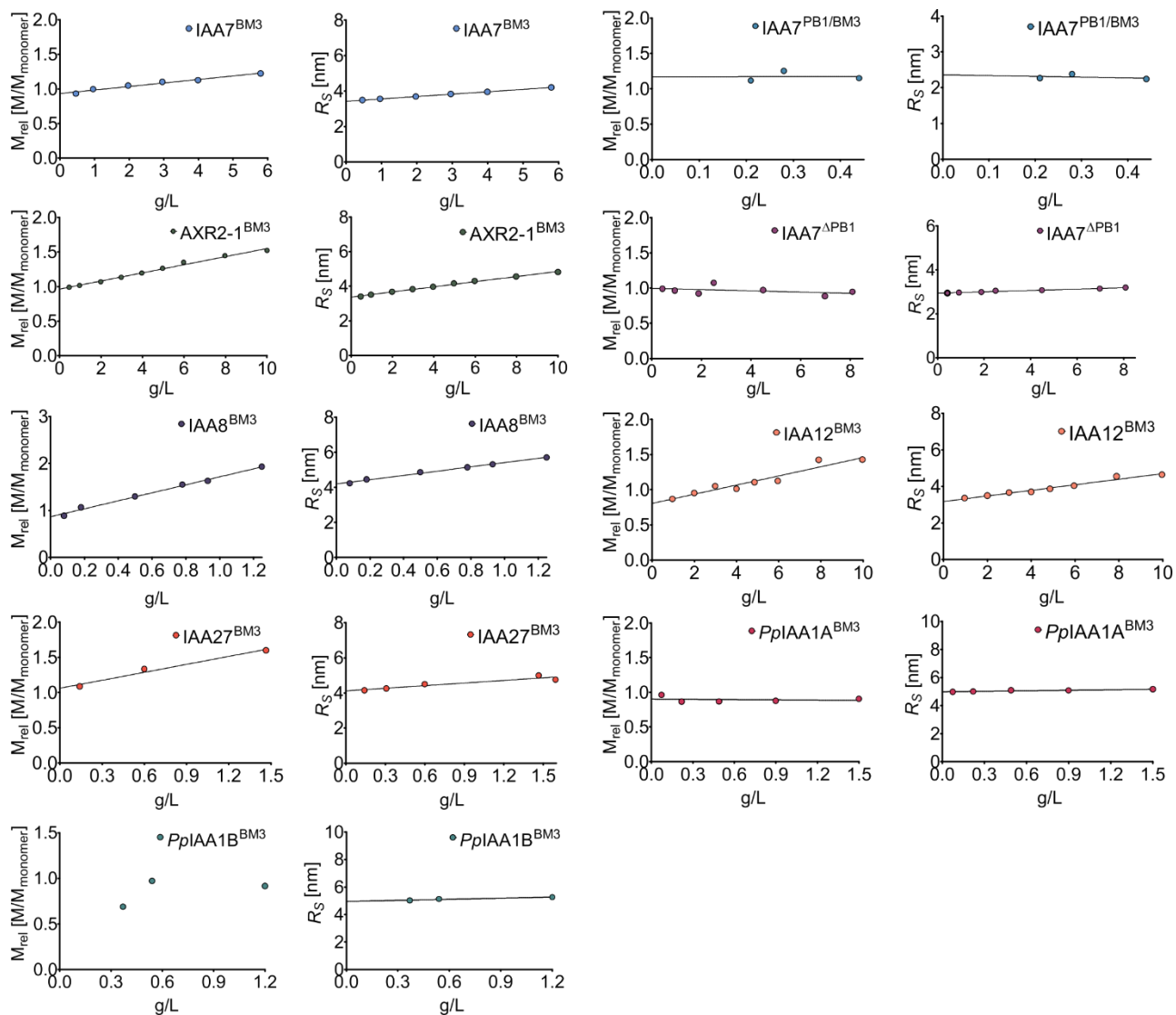
# 7. Appendix



**Figure S1. Extrapolated relative mass and $R_S$ results from AUX/IAA DLS/SLS measurements.** Measurements were performed in serial dilutions and results were extrapolated to zero to determine the relative masses and $R_S$ values, respectively. Some of our relative mass determination exceeded our 10% expected error, nevertheless, for these cases the relative mass slope clearly indicates a monomeric state.
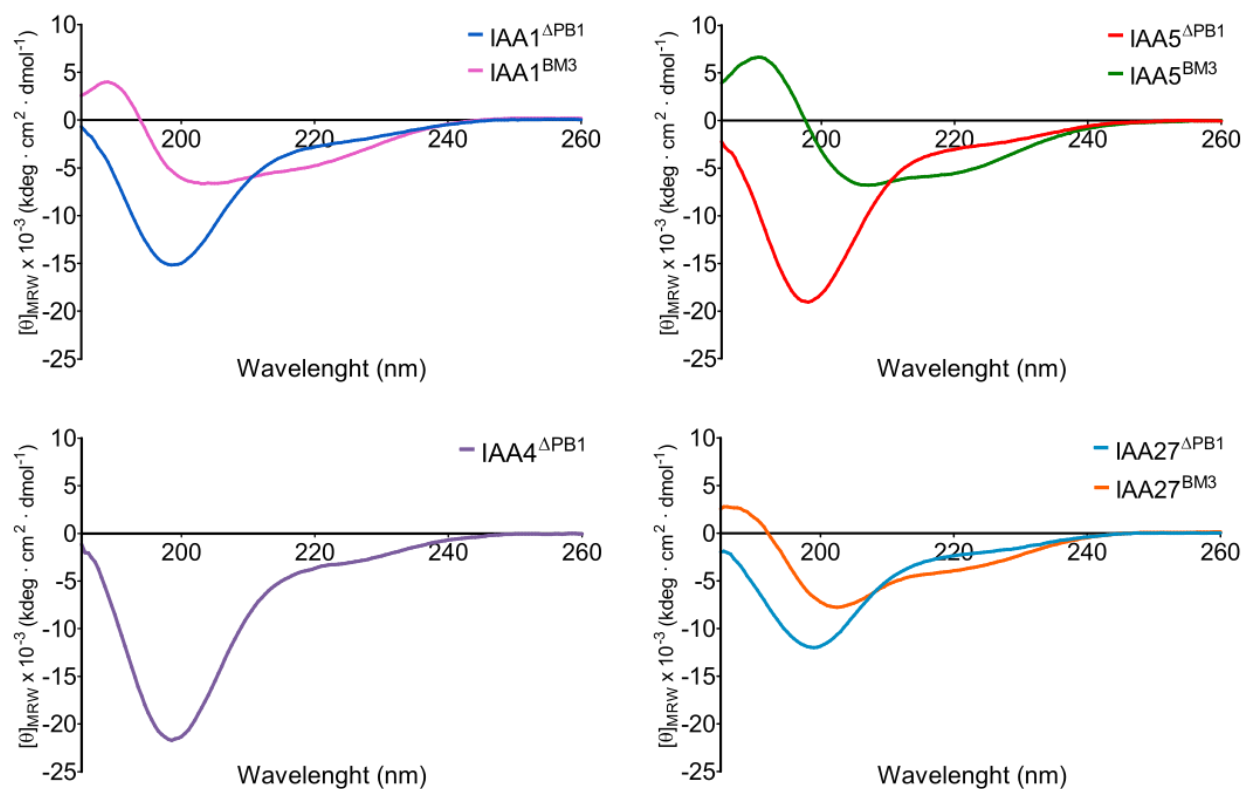
**Figure S2. CD spectroscopy shows random coil structures at the N-terminal IDR of short and long length AUX/IAAs.** Measurements with IAA1, IAA4, IAA5 variants were carried out at 5 µM. For IAA27 variants the measurements were carried out at 2.5 µM. Ellipticity values were corrected a normalized by the protein concentration and the numbers of peptide bonds of each protein measured.
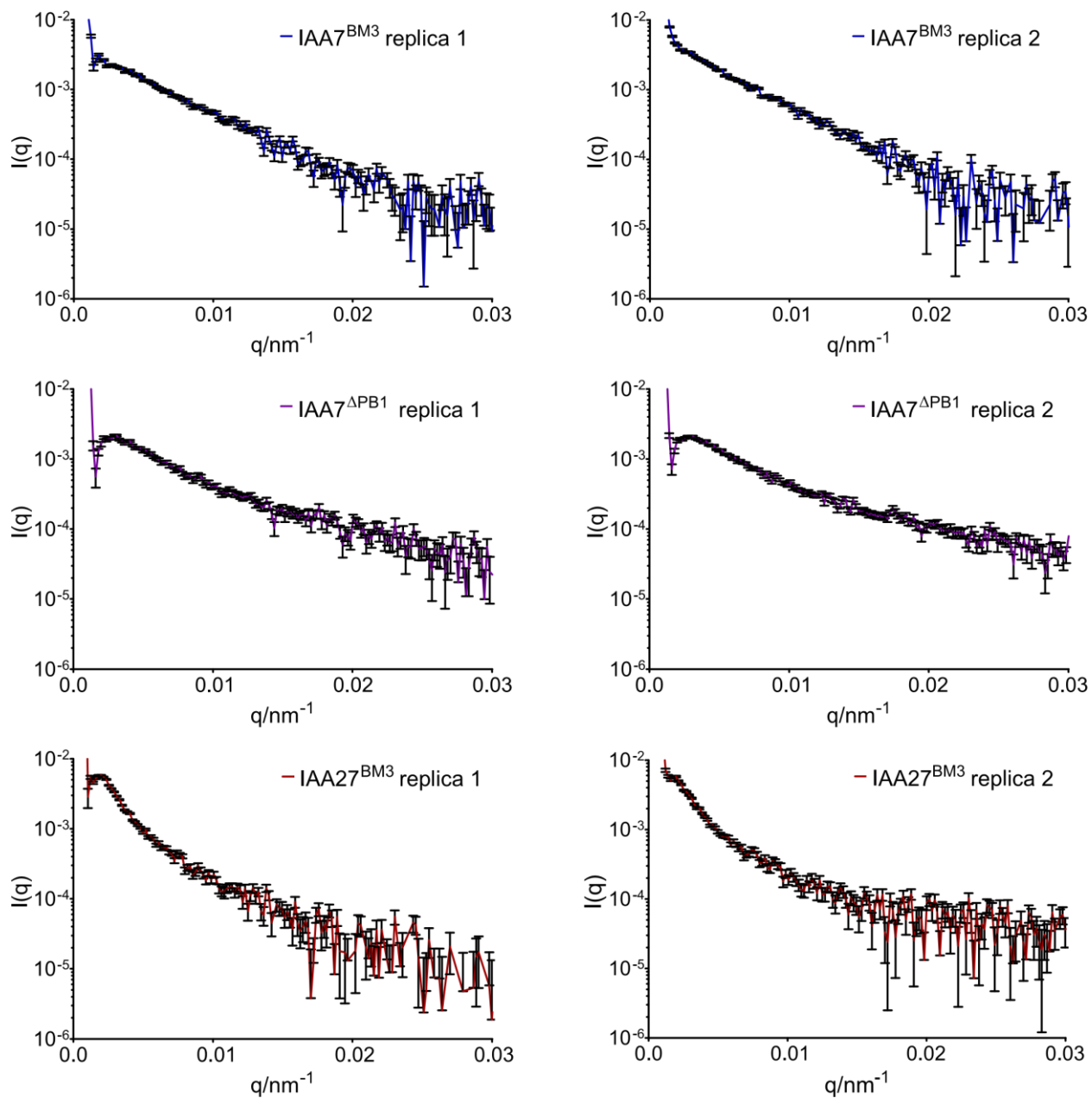
**Figure S3. SAXS profiles of IAA7$^{BM3}$, IAA7$^{\Delta PB1}$ and IAA27$^{BM3}$.** SAXS profiles were recorded in two technical replicas with protein concentrations of 3.3 g/L, 2 g/L and 1.05 g/L for IAA7$^{\Delta PB1}$, IAA7$^{BM3}$and IAA27$^{BM3}$, respectively. In each replica the I(q) error is shown.
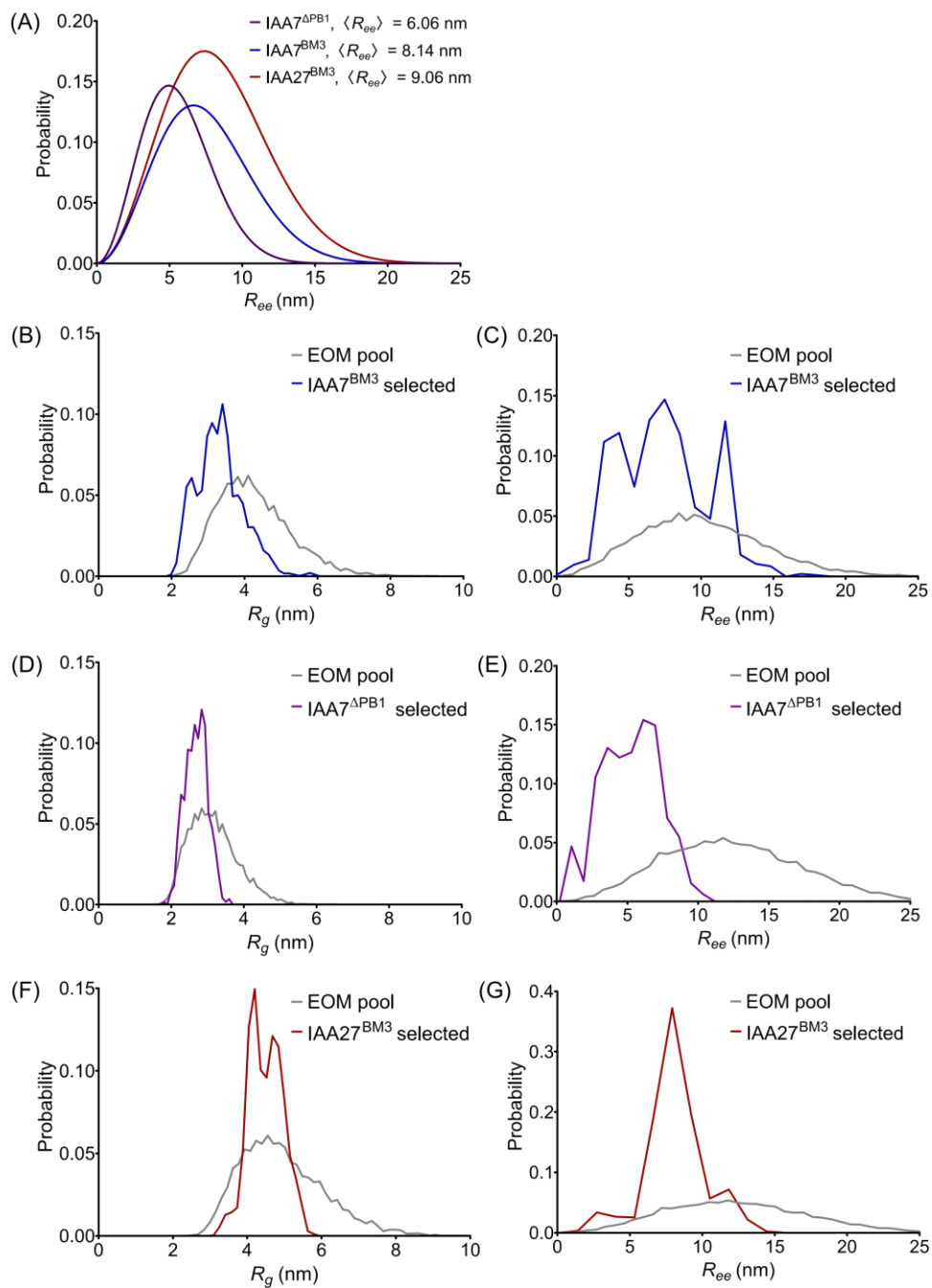
**Figure S4. Ensemble optimization method (EOM) performed on IAA7$^{BM3}$, IAA7$^{\Delta PB1}$ and IAA27$^{BM3}$ SAXS profile.** Initial pool contained 10,000 models with random conformations of which those that best match the experimental SAXS average profile were selected. EOM results are presented in terms of $R_{ee}$ fitted curves (A) or unfitted (C, E and G), and $R_g$ unfitted curves (B, D and F).
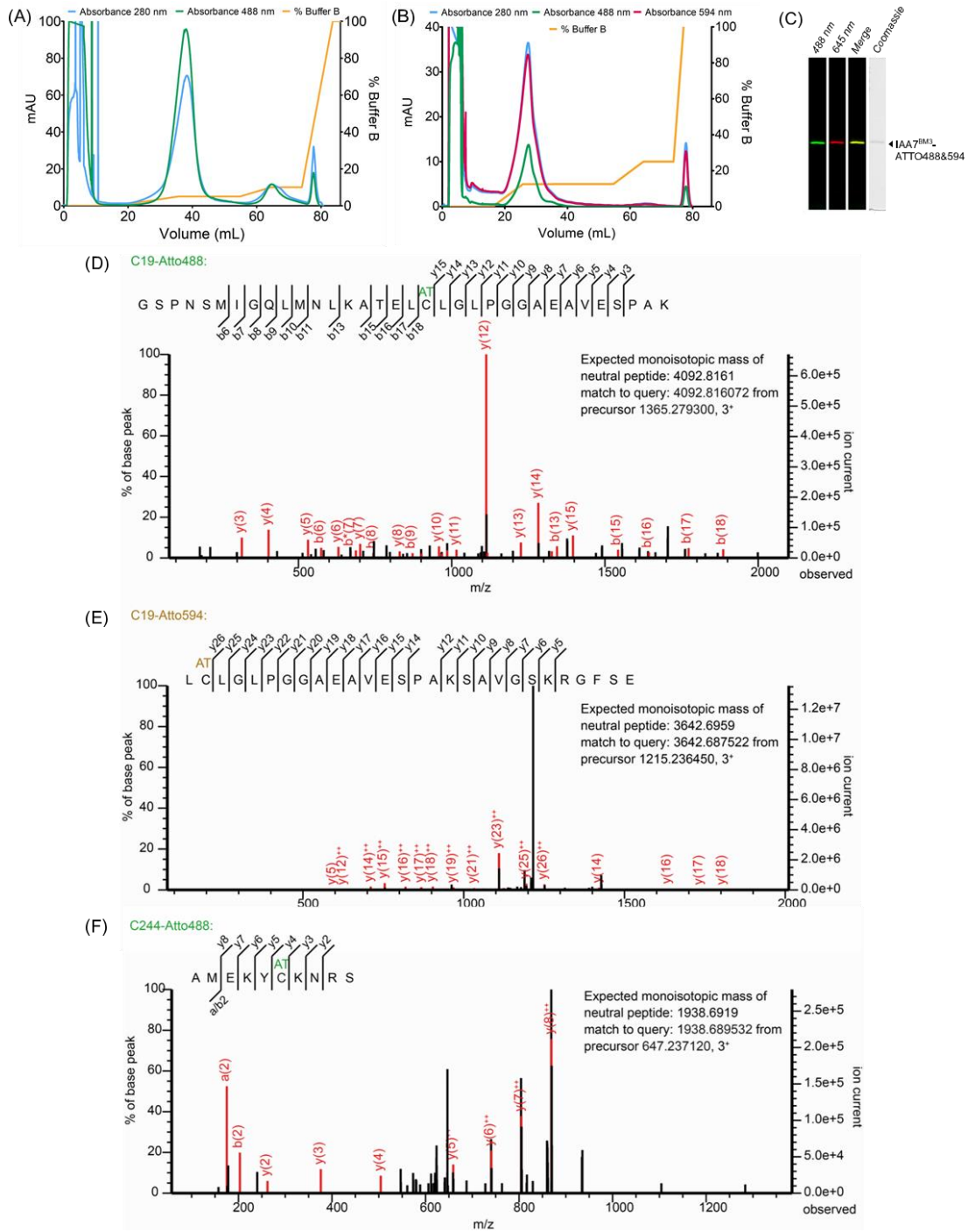
**Figure S5. Purification and detection of labeled IAA7<sup>BM3</sup> for smFRET experiments.** (A, B) Elution profile of ATTO488 and ATTO488-594 labeled IAA7$^{BM3}$ in a HiTrap$^{TM}$ SP HP column with an ÄKTA FPLC system. Samples were eluted in 20 mM KPi pH 5.0, 5 mM DTT buffer with a gradient from 0.02 to 1 M of NaCl. Wavelength detection at 280 nm, 488 nm and 594 nm were used to identify elution of protein, ATTO488 and ATTO594, respectively. (C) Gel scan detection of doubly labeled IAA7$^{BM3}$ fractions in Typhoon FLA 9500 shows fluorescence emission of acceptor and donor of IAA7$^{BM3}$. (D) LC-MS/MS Identification of ATTO488 and ATTO594 labeled IAA7$^{BM3}$. ATTO488 was identified in C19 and C244, while ATTO594 was identified only in C244 due to low sequence coverage at the C-terminal.
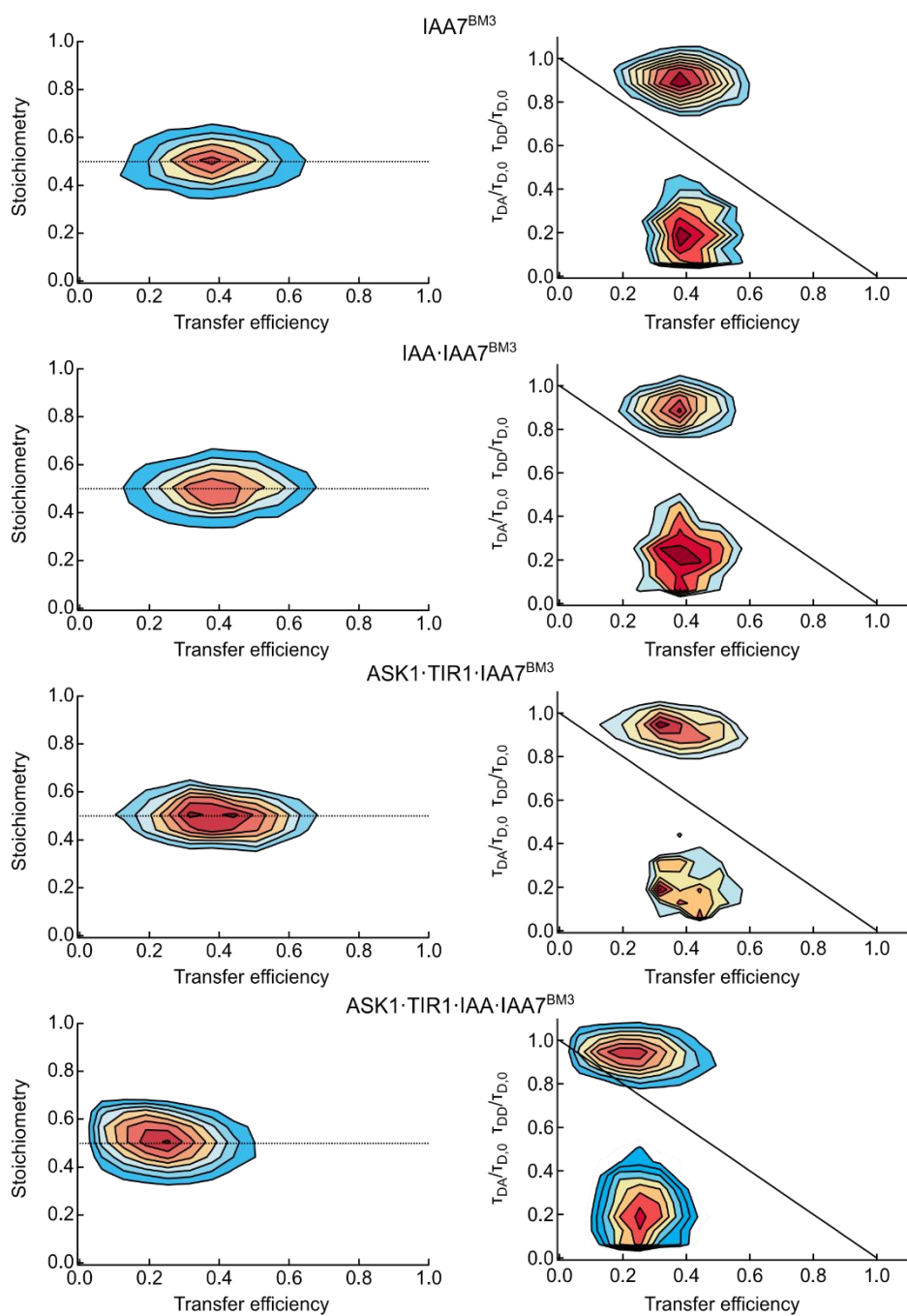
**Figure S6. smFRET stoichiometry plots and fluorescence lifetime analysis.** Stoichiometry versus transfer efficiency plots from intermolecular smFRET measurements. Fluorescence lifetimes of ATTO488 donor ($\tau_{DD}$) and ATTO594 acceptor ($\tau_{AD}$) normalized by the intrinsic donor lifetime ($\tau_{D,0}$) versus the radiometric transfer efficiency *E* used as a diagnose of a broad distance distribution rapidly sampled during the time of a fluorescence burst. The location of the normalized donor lifetimes clustered above the solid diagonal and the acceptor lifetimes below, which is expected for an IDP.
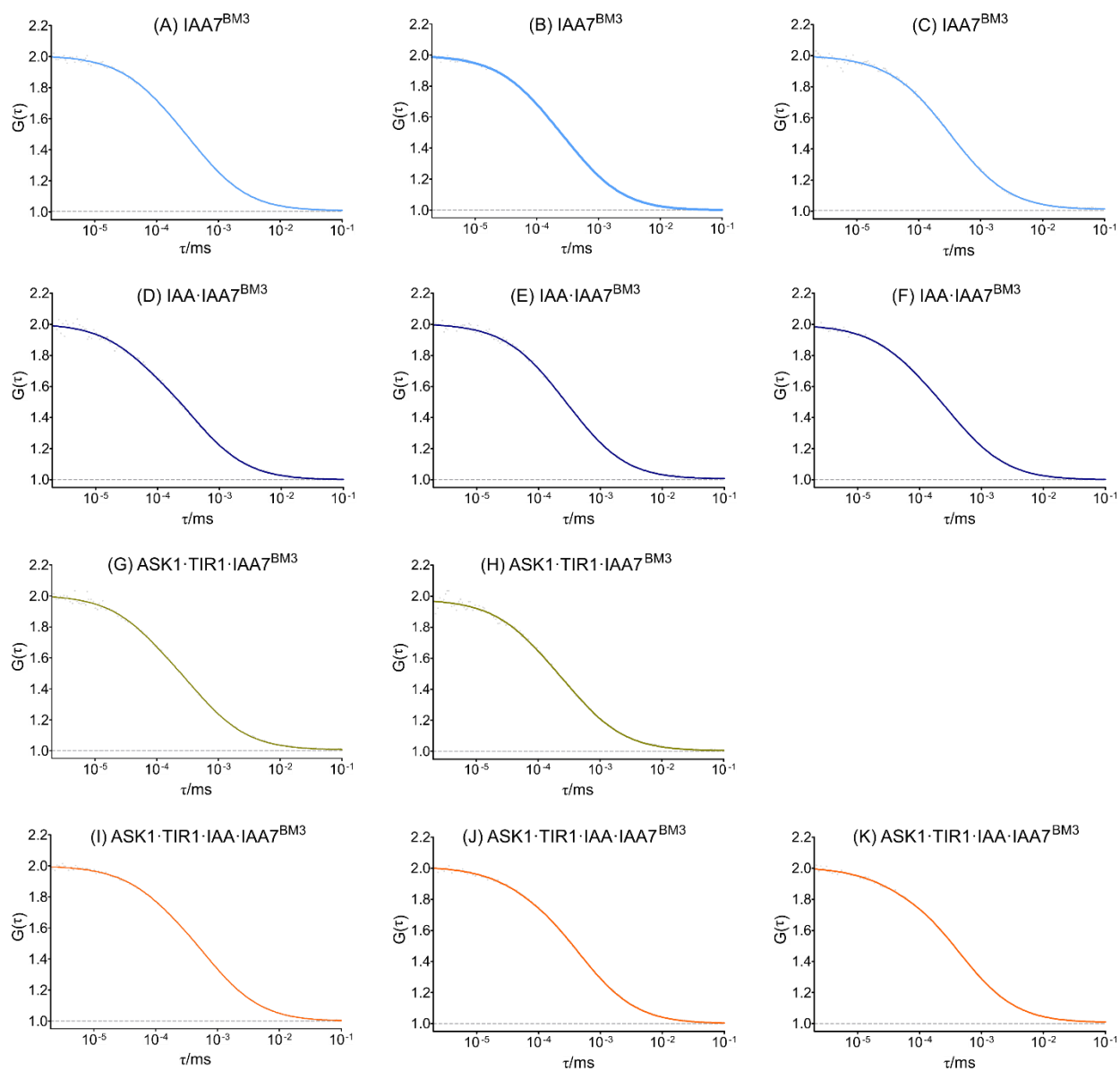
93

**Figure S7. FCCS individual replicas.** (A) Autocorrelation fitted curves describe the decay time of the translational diffusion used for determination of $R_S^{FCCS}$ values of doubly labeled IAA7[BM3] (A-C), IAA·IAA7[BM3] (D-F), ASK1·TIR1·IAA7[BM3] (G-H) and ASK1·TIR1·IAA7[BM3] (I-K) in each replica.
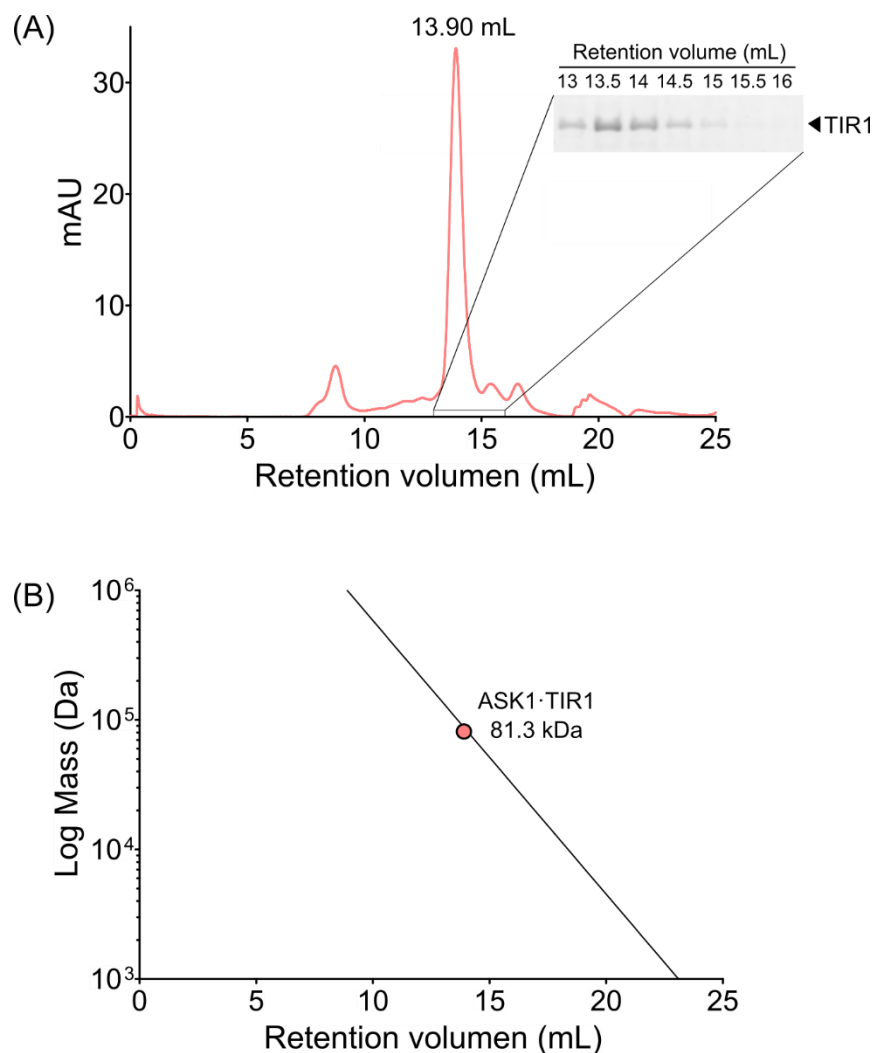
94

**Figure S8. Mass determination of ASK1·TIR1 by size exclusion chromatography (SEC).** (A) Elution profile of ASK1·TIR1 in an Increase 10/300 Superdex 200 SEC column. Elution of ASK1·TIR1 at 13.90 mL was confirmed by SDS-PAGE, only TIR1 is shown in gel for visualization purposes. (B) Mass determination was perform from a linear regression with protein standards of known molecular weight and determined retention times in the Increase 10/300 Superdex 200 SEC column, using the equation: $Mass = 10^{\wedge(-0.24*(retention\ volume)+8.34)}$. The protein standards used for the linear regression were thyroglobulin (670000 Da), y-globuling (158000 Da), BSA (66460 Da), ovalbumin (44000 Da), myoglobin (17000 Da), and vitamin B12 (1350 Da).
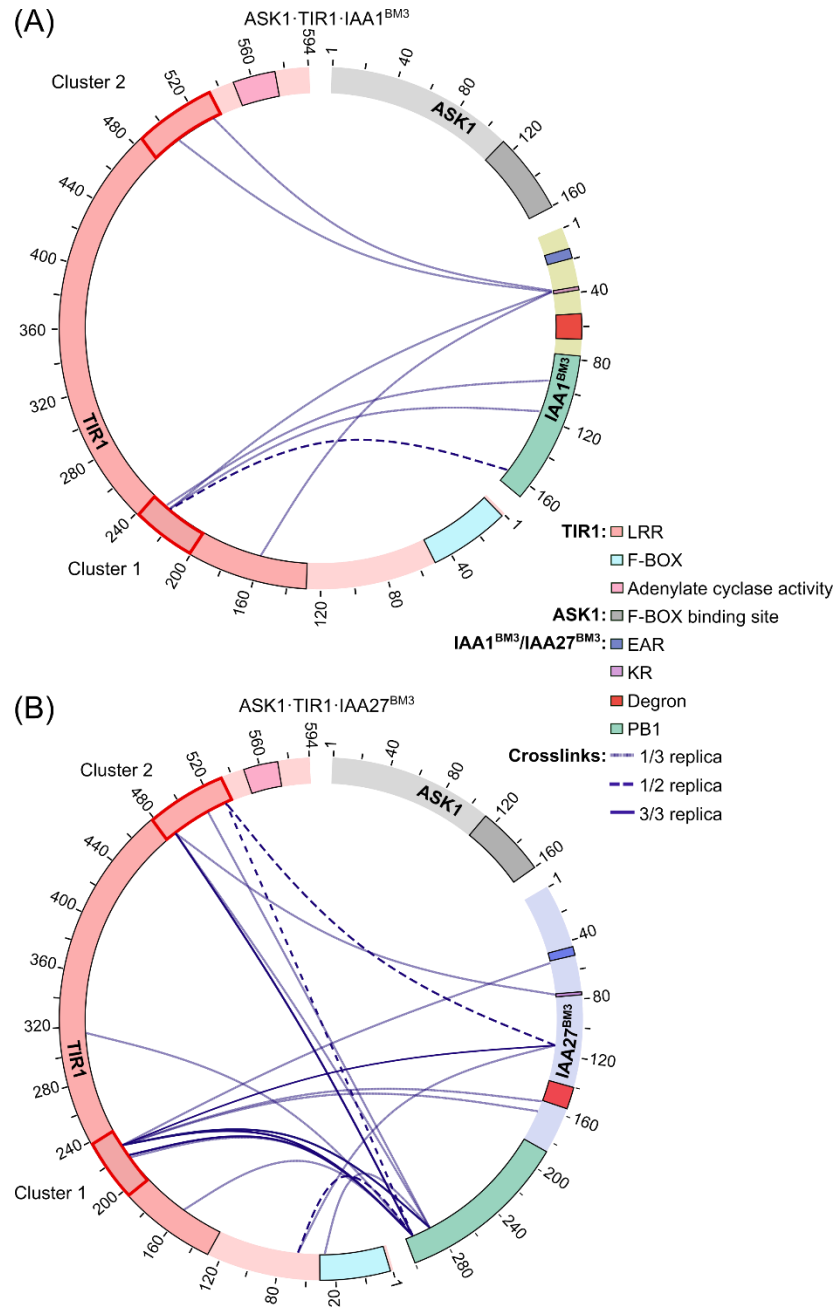
**Figure S9. Circular plots with XL-MS results for ASK1·TIR1·IAA1^BM3 and ASK1·TIR1·IAA27^BM3.** ASK1·TIR1 and IAA1^BM3 or IAA27^BM3 were incubated in the absence of IAA for 15 min before the addition of 100-fold excess of the DSBU crosslinker. Plots show results that were reproducible 1/3, 2/3 and 3/3 of the replicas. In the absence of IAA less crosslinking is observed.
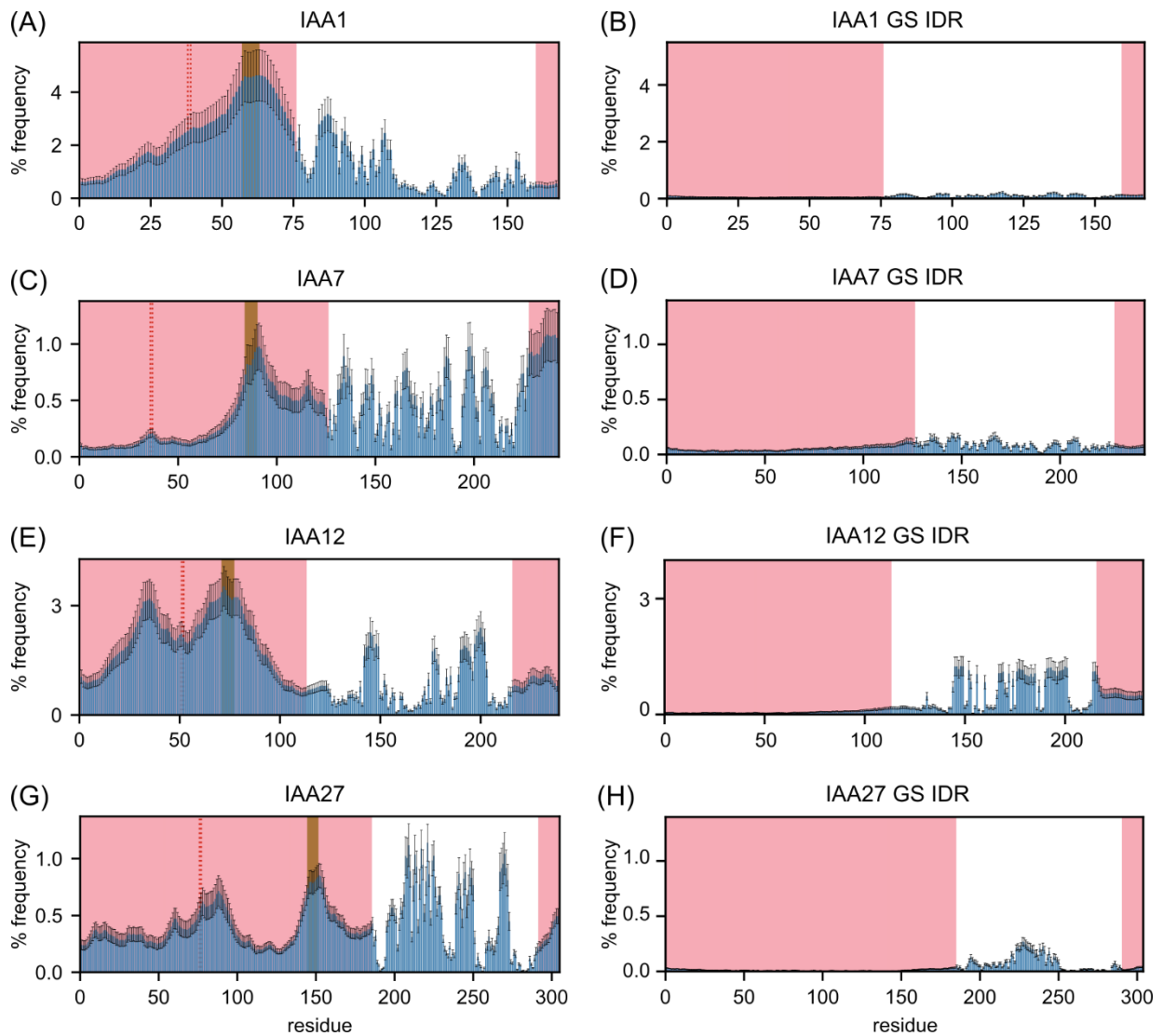
**Figure S10. Mechanisms of ASK·TIR1 and AUX/IAAs association by CG modeling in an auxin-free state.** (A, C, E, and G) Interaction frequency maps of IAA1, IAA7, IAA12 and IAA27 with TIR1·ASK1 in the auxin-free state. For all graphs, the pink shaded areas denote the AUX/IAAs IDRs, the brown shaded region is the GWPPV degron motif, the red dashed lines signify the location of the KR motif, and the white are shows the PB1 domain. (B, D, F, and H) Interaction frequency maps of IAA1, IAA7, IAA12 and IAA27 where the IDR sequence was substituted GS-repeats but the PB1 identity was kept the same for each AUX/IAA protein.
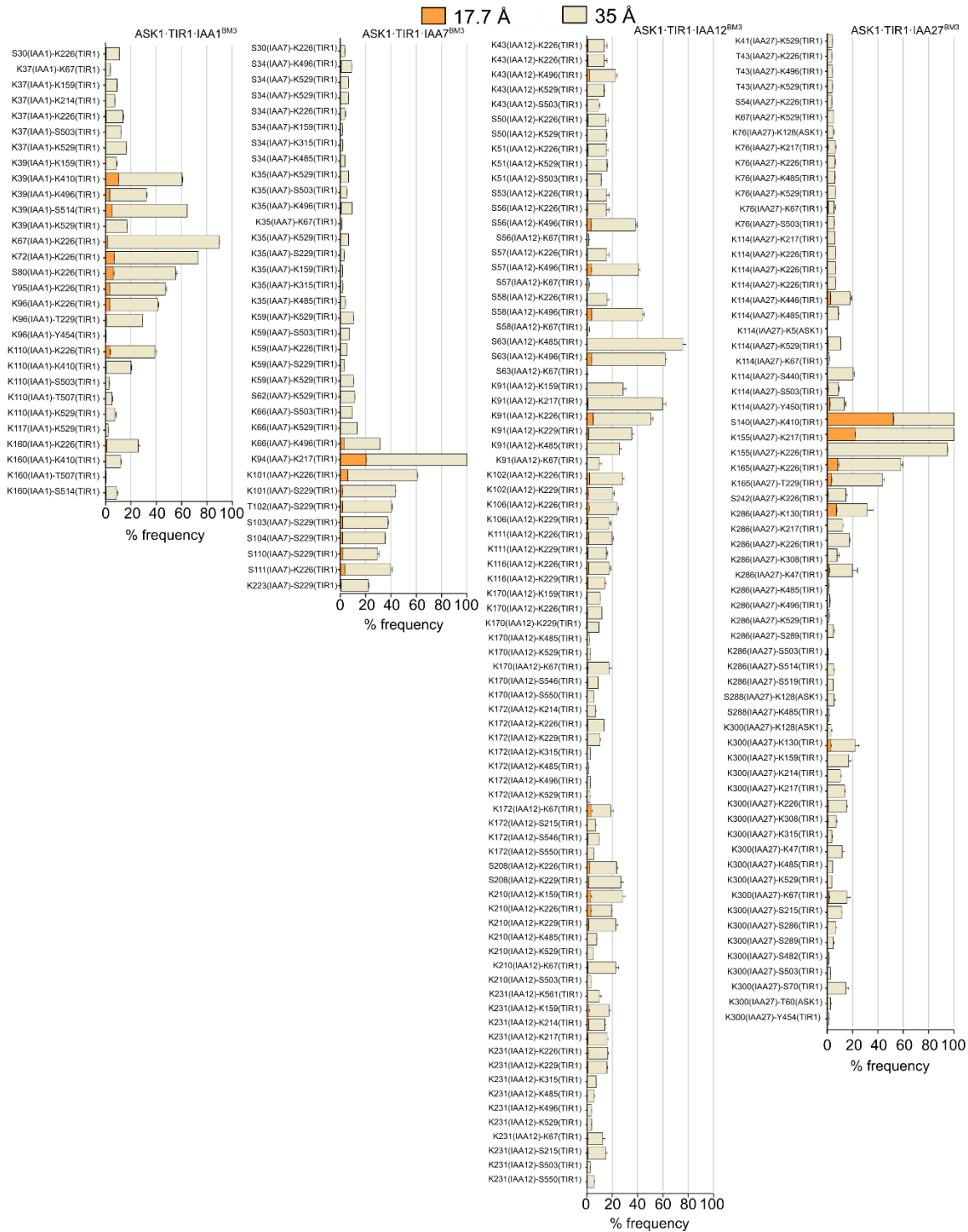
**Figure S11. % of frequency of interaction between AUX/IAA and ASK1·TIR1.** Crosslinked residues between ASK1·TIR1 and AUX/IAAs were traced for interactions throughout the CG-simulations using 17.7 Å and 35 Å distance cutoffs determined as the average and maximum Cα-Cα distance of DSBU, respectively.
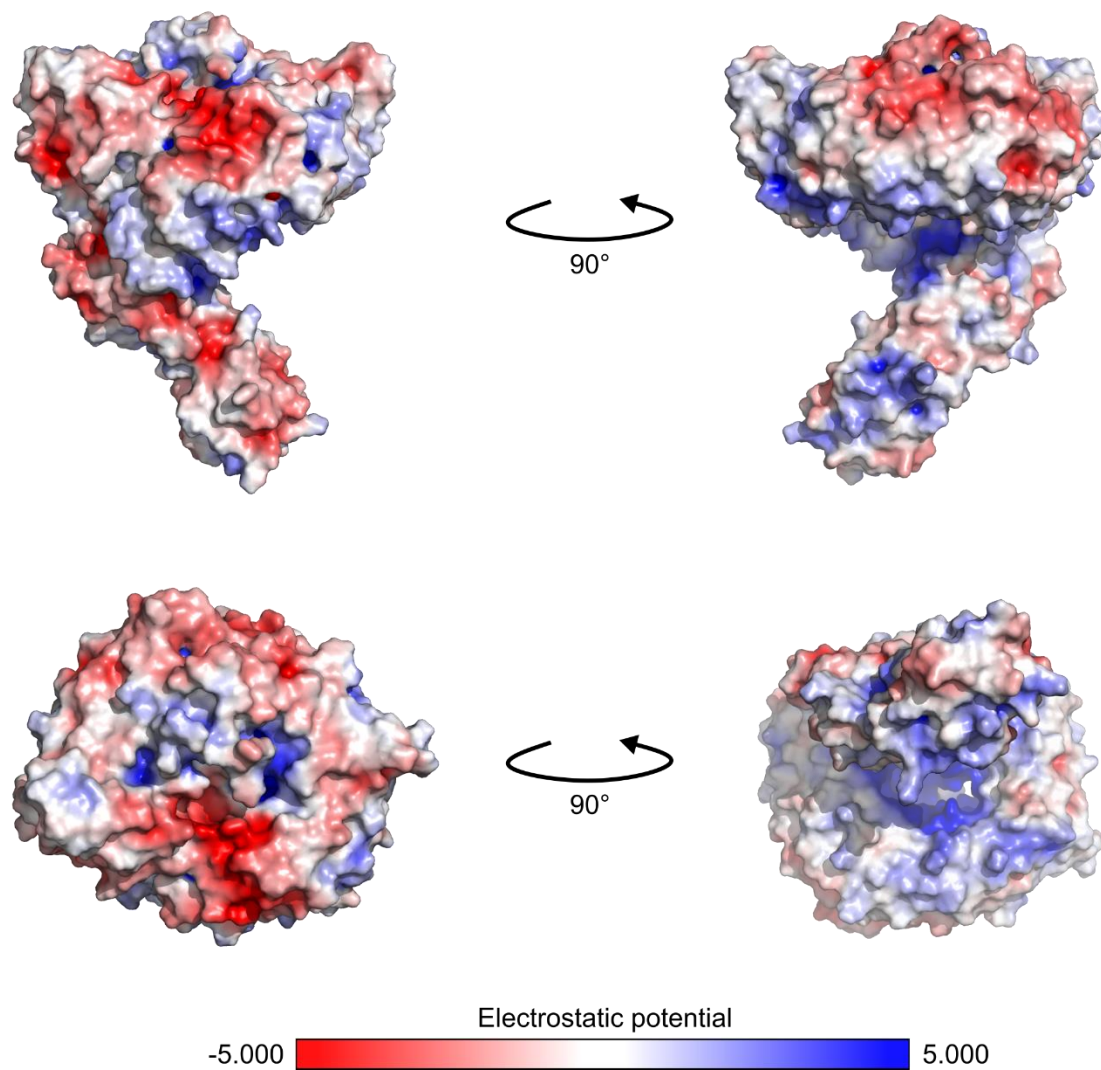
**Figure S12**. **Electrostatic properties of ASK1·TIR complex determined by the Adaptive Poisson-Boltzmann Solver (APBS) tool in pymol.** Electrostatic potentials were obtained with a solute dielectric constant of 2 and a solvent dielectric of 78.5. (A, B) Front and back view of ASK1·TIR1. (C, D) Top and bottom view of ASK1·TIR1. The blue color indicates regions of positive potential whereas red depicts negative potential values. White areas indicate an electrostatic potential of 0 (Baker, Sept, Joseph, Holst, & McCammon, 2001).
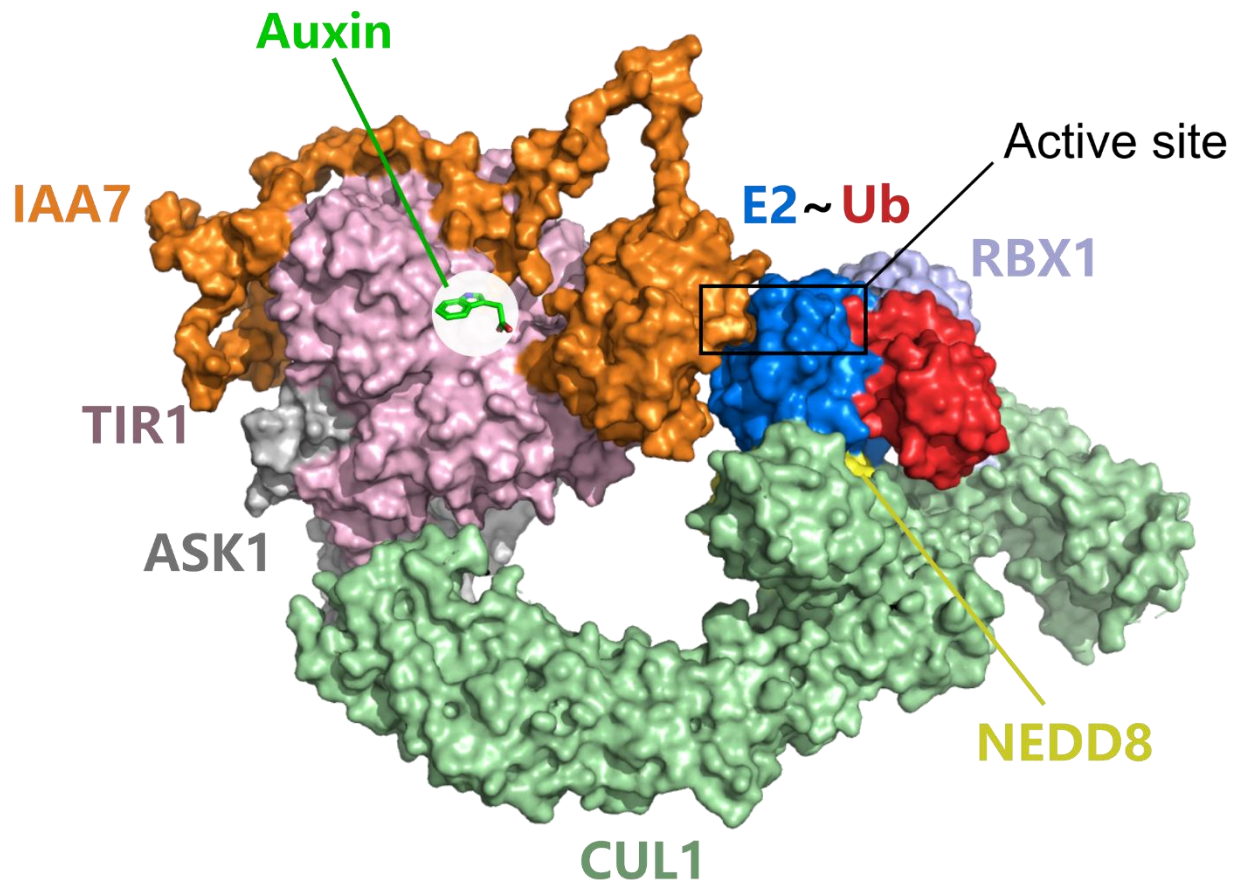
**Figure S13. Reconstruction of a NEDD8 activated SCF^TIR1 – E3 ligase model.** The model was build using the SCF^βTrCP crystal structure (PDB: 6TTU) where the SKP1·βTrCP was aligned and substituted by ASK1·TIR1 (PDB: 2P1Q) with the modeled IAA7 docked in the respective cluster I and II (Baek et al., 2020; Niemeyer et al., 2020; Tan et al., 2007). The IAA7 model docked in TIR1 cluster I and cluster II were generated by Elena Moreno.

**Table S1. Summary table with AUX/IAAs extrapolated relative masses, extrapolated $R_S$ (nm) and compaction index (CI) values.** For AtIAA1[BM3], AtIAA1[BM4] and AtIAA4[BM3] the extrapolated $R_S$ (nm) and CIs were calculated with a single protein concentration with a clear distinction between the monomer and dimer population.

| Aux/IAAs | Extrapolated relative mass | Oligomarization state | Extrapolated $R_S$ (nm) | Compaction index (CI) |
|---|---|---|---|---|
| *At*IAA1[BM3] | - | Monomer-dimer equilibrium | 3.72 (3.93 g/L)* | 0.49 (3.93 g/L)** |
| *At*IAA1[BM4] | - | Monomer-dimer equilibrium | 3.89 (9.50 g/L)* | 0.42 (9.50 g/L)** |
| *At*IAA4[BM3] | - | Monomer-dimer equilibrium | 3.28 (0.46 g/L)* | 0.25 (0.46 g/L)** |
| *At*IAA7[BM3] | 0.93 | Monomer | 3.422 | 0.36 |
| *At*AXR2-1[BM3] | 0.96 | Monomer | 3.369 | 0.39 |
| *At*IAA7[ΔPB1] | 1.00 | Monomer | 2.94 | 0.08 |
| *At*IAA7[PB1/BM3] | 1.17 | Monomer | 2.359 | 0.53 |
| *At*IAA8[BM3] | 0.87 | Monomer | 4.196 | 0.23 |
| *At*IAA12[BM3] | 0.81 | Monomer | 3.173 | 0.48 |
| *At*IAA27[BM3] | 1.06 | Monomer | 4.12 | 0.22 |
| *Pp*IAA1A[BM3] | 0.9 | Monomer | 4.986 | 0.25 |
| *Pp*IAA1B[BM3] | - | Monomer | 4.946 | 0.29 |

**Table S2. smFRET summary.** Measurements were performed in three separate biological replicas. Single replicas FRET burst were combined into a single file which was used for plotting the final results.

| | Replica | $\langle E \rangle$ | Fit Error of the mean | Gaussian width | Gaussian Sigma | $R_{ee}^{FRET}$ (nm) | $R_{ee}^{FRET}$ (nm) without linker correction |
|---|---|---|---|---|---|---|---|
| IAA7$^{BM3}$ | 1 | 0.373 | 0.003 | 0.174 | 0.123 | 7.08 | 7.26 |
| | 2 | 0.402 | 0.003 | 0.192 | 0.136 | 6.77 | 6.97 |
| | 3 | 0.387 | 0.005 | 0.206 | 0.146 | 6.92 | 7.11 |
| | Combine files | 0.383 | 0.002 | 0.19 | 0.134 | 7.16 | 7.16 |
| ASK1·TIR1·IAA7$^{BM3}$ | 1 | 0.389 | 0.006 | 0.265 | 0.187 | 7.09 | 7.09 |
| | 2 | 0.402 | 0.007 | 0.286 | 0.202 | 6.96 | 6.96 |
| | 3 | 0.392 | 0.004 | 0.255 | 0.18 | 7.06 | 7.06 |
| | Combine files | 0.392 | 0.003 | 0.266 | 0.188 | 7.06 | 7.08 |
| IAA·IAA7$^{BM3}$ | 1 | 0.39 | 0.004 | 0.191 | 0.135 | 7.08 | 7.08 |
| | 2 | 0.39 | 0.004 | 0.191 | 0.135 | 7.08 | 7.08 |
| | 3 | 0.378 | 0.008 | 0.191 | 0.135 | 7.21 | 7.21 |
| | Combine files | 0.405 | 0.002 | 0.189 | 0.134 | 6.93 | 6.93 |
| ASK1·TIR1·IAA·IAA7$^{BM3}$ | 1 | 0.23 | 0.009 | 0 | 0.12 | 9.28 | 9.28 |
| | | 0.39 | Fixed | | 0.13 | | |
| | 2 | 0.215 | 0.006 | 0 | 0.111 | 9.58 | 9.58 |
| | | 0.39 | Fixed | | 0.13 | | |
| | 3 | 0.204 | 0.003 | 0 | 0.123 | 9.8 | 9.8 |
| | | 0.39 | Fixed | | 0.13 | | |
| | Combine files | 0.212 | 0.003 | 0 | 0.119 | 9.64 | 9.64 |
| | | 0.39 | Fixed | | 0.13 | | |

**Table S3.** Summary table with $R_S$ values with IAA7[BM3] alone or in the presence of IAA, ASK1·TIR1 or both determine by FCCS.

| | | 1ST replica | 2nd replica | 3rd replica | $R_S^{FCCS}$ (nm)±s.d. |
|---|---|---|---|---|---|
| IAA7[BM3] | $\tau_D$ (ms) | 3.38E-04 | 3.15E-04 | 3.88E-04 | 3.48±0.18 |
| | $R_S^{FCCS}$ (nm) | 3.39±0.09 | 3.69±0.03 | 3.36±0.11 | |
| IAA·IAA7[BM3] | $\tau_D$ (ms) | 3.54E-04 | 3.13E-04 | 3.60E-04 | 3.35±0.07 |
| | $R_S^{FCCS}$ (nm) | 3.59±0.17 | 3.47±0.09 | 3.23±0.15 | |
| ASK1·TIR1·IAA7[BM3] | $\tau_D$ (ms) | 3.05E-04 | 3.81E-04 | N.D. | 3.43±0.18 |
| | $R_S^{FCCS}$ (nm) | 3.40±0.18 | 3.30±0.16 | N.D. | |
| ASK1·TIR1·IAA·IAA7[BM3] | $\tau_D$ (ms) | 6.11E-04 | 6.72E-04 | 8.84E-04 | 7.56±0.30 |
| | $R_S^{FCCS}$ (nm) | 7.24±0.20 | 7.83±0.14 | 7.60±0.17 | |

**Table S4.** Summary of the dataset used for AUX/IAAs analysis across land plant species.

| Species group | Species | Family | Source database | Database reference | AUX/IAAs sequence count |
|---|---|---|---|---|---|
| Bryophytes | *Marchantia polymorpha* | Marchantiaceae | Phytozome | (Bowman et al., 2017; Goodstein et al., 2012) | 1 |
| | *Physcomitrium patens* | Funariaceae | Phytozome | (Goodstein et al., 2012; Lang et al., 2018) | 3 |
| Lycophyte | *Selaginella moellendorffii* | Selaginellaceae | Phytozome | (Banks et al., 2011; Goodstein et al., 2012) | 6 |
| Ferns | *Azolla filiculoides* | Salviniaceae | Fernbase | (Li et al., 2018) | 6 |
| | *Ceratopteris richardii* | Pteridaceae | NCBI | (Marchant et al., 2019; Schoch et al., 2020) | 1 |
| | *Salvinia cucullata* | Salviniaceae | Fernbase | (Li et al., 2018) | 8 |
| Gymnosperms | *Ginkgo biloba L.* | Ginkgoaceae | GIGA | (Guan et al., 2016) | 7 |
| Angiosperms basal | *Amborella trichopoda* | Amborellaceae | Phytozome | ("The Amborella genome and the evolution of flowering plants," 2013; Consortium, 2022) | 9 |
| Angiosperms monocots | *Brachypodium distachyon* | Poaceae | UniProtKB; KEGG Orthology K14484 | (Consortium, 2022; Kanehisa et al., 2016) | 22 |
| | *Elaeis guineensis var. tenera* | Arecaceae | UniProtKB; KEGG Orthology K14484 | (Consortium, 2022; Kanehisa et al., 2016) | 25 |
| | *Musa acuminata subsp. malaccensis* | Musaceae | Phytozome | (Droc et al., 2013; Goodstein et al., 2012) | 45 |
| | *Oryza brachyantha* | Poaceae | UniProtKB; KEGG Orthology K14484 | (Consortium, 2022; Kanehisa et al., 2016) | 14 |
| | *Oryza sativa subsp. japonica* | Poaceae | Phytozome | (Goodstein et al., 2012; Ouyang et al., 2007) | 27 |
| | *Phoenix dactylifera* | Arecaceae | UniProtKB; KEGG Orthology K14484 | (Consortium, 2022; Kanehisa et al., 2016) | 25 |
| | *Setaria italica* | Poaceae | UniProtKB; KEGG Orthology K14484 | (Consortium, 2022; Kanehisa et al., 2016) | 24 |
| | *Sorghum bicolor* | Poaceae | UniProtKB; KEGG Orthology K14484 | (Consortium, 2022; Kanehisa et al., 2016) | 15 |
| | *Zea mays* | Poaceae | UniProtKB; KEGG Orthology K14484 | (Consortium, 2022; Kanehisa et al., 2016) | 29 |
| Angiosperms dicots | Abrus precatorius | Fabaceae | UniProtKB; KEGG Orthology K14484 | (Consortium, 2022; Kanehisa et al., 2016) | 27 |
| | Arabidopsis lyrata subsp. lyrata | Brassicaceae | Phytozome | (Goodstein et al., 2012; Hu et al., 2011) | 25 |
| | Arabidopsis thaliana | Brassicaceae | Phytozome | (Cheng et al., 2017; Goodstein et al., 2012) | 24 |
| | Arachis duranensis | Fabaceae | UniProtKB; KEGG Orthology K14484 | (Consortium, 2022; Kanehisa et al., 2016) | 20 |
| | Beta vulgaris subsp. vulgaris | Amaranthaceae | UniProtKB; KEGG Orthology K14484 | (Consortium, 2022; Kanehisa et al., 2016) | 3 |
| | Brassica campestris | Brassicaceae | UniProtKB; KEGG Orthology K14484 | (Consortium, 2022; Kanehisa et al., 2016) | 20 |
| | Brassica napus | Brassicaceae | UniProtKB; KEGG Orthology K14484 | (Consortium, 2022; Kanehisa et al., 2016) | 27 |
| | Brassica oleracea var. oleracea | Brassicaceae | UniProtKB | (Goodstein et al., 2012; S. Liu et al., 2014) | 23 |
| | Brassica rapa | Brassicaceae | Phytozome | (Goodstein et al., 2012; X. Wang et al., 2011) | 29 |
| | Capsella rubella | Brassicaceae | Phytozome | (Goodstein et al., 2012; Slotte et al., 2013) | 24 |
| | Capsicum annuum | Solanaceae | UniProtKB; KEGG Orthology K14484 | (Consortium, 2022; Kanehisa et al., 2016) | 19 |
| | Carica papaya | Caricaceae | Phytozome | (Goodstein et al., 2012; Ming et al., 2008) | 16 |
| | Cicer arietinum | Fabaceae | UniProtKB; KEGG Orthology K14484 | (Consortium, 2022; Kanehisa et al., 2016) | 17 |

| | Citrus clementina | Rutaceae | UniProtKB; KEGG Orthology K14484 | (Consortium, 2022; Kanehisa et al., 2016) | 20 |
|---|---|---|---|---|---|
| | Citrus sinensis | Rutaceae | UniProtKB; KEGG Orthology K14484 | (Consortium, 2022; Kanehisa et al., 2016) | 4 |
| | Cleome violacea | Cleomeaceae | Phytozome | (Goodstein et al., 2012) | 19 |
| | Cucumis melo | Cucurbitaceae | UniProtKB; KEGG Orthology K14484 | (Consortium, 2022; Kanehisa et al., 2016) | 25 |
| | Cucumis sativus | Cucurbitaceae | UniProtKB; KEGG Orthology K14484 | (Consortium, 2022; Kanehisa et al., 2016) | 23 |
| | Cucurbita maxima | Cucurbitaceae | UniProtKB; KEGG Orthology K14484 | (Consortium, 2022; Kanehisa et al., 2016) | 46 |
| | Cucurbita moschata | Cucurbitaceae | UniProtKB; KEGG Orthology K14484 | (Consortium, 2022; Kanehisa et al., 2016) | 44 |
| | Daucus carota subsp. sativus | Apiaceae | UniProtKB; KEGG Orthology K14484 | (Consortium, 2022; Kanehisa et al., 2016) | 18 |
| | Durio zibethinus | Malvaceae | UniProtKB; KEGG Orthology K14484 | (Consortium, 2022; Kanehisa et al., 2016) | 49 |
| | Erythranthe guttata | Phrymaceae | UniProtKB; KEGG Orthology K14484 | (Consortium, 2022; Kanehisa et al., 2016) | 15 |
| | Eucalyptus grandis | Myrtaceae | UniProtKB; KEGG Orthology K14484 | (Consortium, 2022; Kanehisa et al., 2016) | 14 |
| | Eutrema salsugineum | Brassicaceae | Phytozome | (Goodstein et al., 2012; Yang et al., 2013) | 22 |
| | Glycine max | Fabaceae | Phytozome | (Goodstein et al., 2012; Valliyodan et al., 2019) | 51 |
| | Gossypium arboreum | Malvaceae | UniProtKB; KEGG Orthology K14484 | (Consortium, 2022; Kanehisa et al., 2016) | 38 |
| | Gossypium hirsutum | Malvaceae | UniProtKB; KEGG Orthology K14484 | (Consortium, 2022; Kanehisa et al., 2016) | 59 |
| | Gossypium raimondii | Malvaceae | UniProtKB; KEGG Orthology K14484 | (Consortium, 2022; Kanehisa et al., 2016) | 32 |
| Angiosperms dicots | Ipomoea nil | Convolvulaceae | UniProtKB; KEGG Orthology K14484 | (Consortium, 2022; Kanehisa et al., 2016) | 1 |
| | Jatropha curcas | Euphorbiaceae | UniProtKB; KEGG Orthology K14484 | (Consortium, 2022; Kanehisa et al., 2016) | 16 |
| | Juglans regia | Juglandaceae | UniProtKB; KEGG Orthology K14484 | (Consortium, 2022; Kanehisa et al., 2016) | 33 |
| | Lupinus angustifolius | Fabaceae | UniProtKB; KEGG Orthology K14484 | (Consortium, 2022; Kanehisa et al., 2016) | 5 |
| | Malus domestica | Rosaceae | UniProtKB; KEGG Orthology K14484 | (Consortium, 2022; Kanehisa et al., 2016) | 13 |
| | Medicago truncatula | Fabaceae | UniProtKB; KEGG Orthology K14484 | (Consortium, 2022; Kanehisa et al., 2016) | 20 |
| | Momordica charantia | Cucurbitaceae | UniProtKB; KEGG Orthology K14484 | (Consortium, 2022; Kanehisa et al., 2016) | 25 |
| | Morus notabilis | Moraceae | UniProtKB; KEGG Orthology K14484 | (Consortium, 2022; Kanehisa et al., 2016) | 10 |
| | Nelumbo nucifera | Nelumbonaceae | UniProtKB; KEGG Orthology K14484 | (Consortium, 2022; Kanehisa et al., 2016) | 19 |
| | Nicotiana attenuata | Solanaceae | UniProtKB | (Consortium, 2022; Xu et al., 2017) | 24 |
| | Nicotiana sylvestris | Solanaceae | UniProtKB; KEGG Orthology K14484 | (Consortium, 2022; Kanehisa et al., 2016) | 17 |
| | Nicotiana tabacum | Solanaceae | UniProtKB; KEGG Orthology K14484 | (Consortium, 2022; Kanehisa et al., 2016) | 35 |
| | Phaseolus angularis | Fabaceae | UniProtKB; KEGG Orthology K14484 | (Consortium, 2022; Kanehisa et al., 2016) | 16 |
| | Phaseolus vulgaris | Fabaceae | UniProtKB; KEGG Orthology K14484 | (Consortium, 2022; Kanehisa et al., 2016) | 23 |
| | Picea abies | Pinaceae | NCBI | (Nystedt et al., 2013; Schoch et al., 2020) | 13 |
| | Populus trichocarpa | Salicaceae | UniProtKB | (Goodstein et al., 2012; Tuskan et al., 2006) | 22 |
| | Prunus avium | Rosaceae | UniProtKB; KEGG Orthology K14484 | (Consortium, 2022; Kanehisa et al., 2016) | 20 |
| | Prunus persica | Rosaceae | UniProtKB; KEGG Orthology K14484 | (Consortium, 2022; Kanehisa et al., 2016) | 17 |

| Angiosperms dicots | Raphanus sativus | Brassicaceae | UniProtKB; KEGG Orthology K14484 | (Consortium, 2022; Kanehisa et al., 2016) | 40 |
|---|---|---|---|---|---|
| | Ricinus communis | Euphorbiaceae | UniProtKB; KEGG Orthology K14484 | (Consortium, 2022; Kanehisa et al., 2016) | 14 |
| | Sesamum indicum | Pedaliaceae | UniProtKB; KEGG Orthology K14484 | (Consortium, 2022; Kanehisa et al., 2016) | 22 |
| | Solanum lycopersicum | Solanaceae | UniProtKB | (Goodstein et al., 2012; Sato et al., 2012) | 23 |
| | Solanum tuberosum | Solanaceae | UniProtKB; KEGG Orthology K14484 | (Consortium, 2022; Kanehisa et al., 2016) | 25 |
| | Theobroma cacao | Malvaceae | UniProtKB; KEGG Orthology K14484 | (Consortium, 2022; Kanehisa et al., 2016) | 7 |
| | Vigna radiata var. radiata | Fabaceae | UniProtKB; KEGG Orthology K14484 | (Consortium, 2022; Kanehisa et al., 2016) | 25 |
| | Vitis vinifera | Vitaceae | UniProtKB; KEGG Orthology K14484 | (Consortium, 2022; Kanehisa et al., 2016) | 12 |
| | Ziziphus jujuba | Rhamnaceae | UniProtKB; KEGG Orthology K14484 | (Consortium, 2022; Kanehisa et al., 2016) | 17 |
| | | | | Total | 1534 |

**Table S5.** List of oligonucleotides used in this study.

| Name | Target | 5' → 3' | Goal |
|------|--------|---------|------|
| IAA4_BM1_FW | pGEX-IAA4 | GGTCAAGGAAACTATGTGGCAGTAAGTATGGATGGTGCTCC | K91 to A amino acid exchange aiming monomeric IAA4 |
| IAA4_BM1_RV | pGEX-IAA4 | GGAGCACCATCCATACTTACTGCCACATAGTTTCCTTGACC | K91 to A amino acid exchange aiming monomeric IAA4 |
| IAA4_BM2_FW | pGEX-IAA4 | GGATGGTGCTCCATATCTAGCGGCGATAGATCTAACGATGTATAAAC | R102 to A and K103 to A amino acid exchange aiming monomeric IAA4 |
| IAA4_BM2_RV | pGEX-IAA4 | GTTTATACATCGTTAGATCTATCGCCGCTAGATATGGAGCACCATCC | R102 to A and K103 to A amino acid exchange aiming monomeric IAA4 |
| IAA1_DELTA_PB1_FW | pGEX-IAA1 | CAAAAACGTGAGTTATGTGAAATAGAGTATGGACGGAGCTC | Exchange of residue V93 by a premature STOP codon for generation of IAA1$^{\Delta PB1}$ variant |
| IAA1_DELTA_PB1_RV | pGEX-IAA1 | GAGCTCCGTCCATACTCTATTTCACATAACTCACGTTTTTG | Exchange of residue V93 by a premature STOP codon for generation of IAA1$^{\Delta PB1}$ variant |
| IAA27_DEL_FW | pGEX(GW)-IAA27 | GGAATTCCAATGTCTGTATCTGTAGCAGCAGAGCATG | Deletion of gateway recombination and exchange of thrombin cleavage site by TEV in pGEX(GW)-IAA27 constructs |
| IAA27_DELTA_PB1_FW | pGEX-IAA27 | CCTTGCTTGTATGTCAAATAGAGTATGGAAGGTGCTCCTTAC | Exchange of residue V190 by a premature STOP codon for generation of IAA27$^{\Delta PB1}$ variant |
| IAA27_DELTA_PB1_RV | pGEX-IAA27 | GTAAGGAGCACCTTCCATACTCTATTTGACATACAAGCAAGG | Exchange of residue V190 by a premature STOP codon for generation of IAA27$^{\Delta PB1}$ variant |
| IAA27_BM1_FW | pGEX-IAA27 | CAACCTTGCTTGTATGTCGCAGTGAGTATGGAAGGTGCTCC | K189 to A amino acid exchange aiming monomeric IAA27 |
| IAA27_BM1_RV | pGEX-IAA27 | GGAGCACCTTCCATACTCACTGCGACATACAAGCAAGGTTG | K189 to A amino acid exchange aiming monomeric IAA27 |
| IAA27_BM2_FW | pGEX-IAA27 | GAAGGTGCTCCTTACTTGGCGGCAATCGATCTCAAGACTTAC | R199 to A and K200 to A amino acid exchange aiming monomeric IAA27 |
| IAA27_BM2_RV | pGEX-IAA27 | GTAAGTCTTGAGATCGATTGCCGCCAAGTAAGGAGCACCTTC | R199 to A and K200 to A amino acid exchange aiming monomeric IAA27 |
| PpIAA1a_FW_attb | cDNA PpIAA1a | GGGGACAAGTTTGTACAAAAAAGCAGGCTTCATGAACGTCAGCGAAGGTTGTAG | Cloning of Physcomitrium patens IAA1A from cDNA with ATTB attachment sites |
| PpIAA1a_RV_attb | cDNA PpIAA1a | GGGGACCACTTTGTACAAGAAAGCTGGGTATCACCCCACCGCCACTTGC | Cloning of Physcomitrium patens IAA1A from cDNA with ATTB attachment sites |
| PpIAA1b_FW_attb | cDNA PpIAA1b | GGGGACAAGTTTGTACAAAAAAGCAGGCTTCATGAAGTTTAGCAACGAAGTT | Cloning of Physcomitrium patens IAA1B from cDNA with ATTB attachment sites |
| PpIAA1b_RV_attb | cDNA PpIAA1b | GGGGACCACTTTGTACAAGAAAGCTGGGTATCACCCCACCGCCACTTGC | Cloning of Physcomitrium patens IAA1B from cDNA with ATTB attachment sites |
| PpIAA2_FW_attb | cDNA PpIAA2 | GGGGACAAGTTTGTACAAAAAAGCAGGCTTCATGAAGTTTAGTGGTGAAGGTT | Cloning of Physcomitrium patens IAA2 from cDNA with ATTB attachment sites |
| PpIAA2_RV_attb | cDNA PpIAA2 | GGGGACCACTTTGTACAAGAAAGCTGGGTATCAACCCACAGCACCTTGG | Cloning of Physcomitrium patens IAA2 from cDNA with ATTB attachment sites |
| IAA1_BM4_FW | pGEX-IAA1$^{BM3}$ | GTTCTCTTCATCTTGTCAAGCACTCAGAATCATGAAAGGATC | K155 to A amino acid exchange aiming monomeric IAA1 |
| IAA1_BM4_RV | pGEX-IAA1$^{BM3}$ | GATCCTTTCATGATTCTGAGTGCTTGACAAGATGAAGAGAAC | K155 to A amino acid exchange aiming monomeric IAA1 |
| IAA7_KR_to_DD_FW | pGEX-IAA7 | CCAAATCGGCGGTGGGAAGCGATGATGGCTTCTCCGAAACCGTTG | K35 to D and R36 to D amino acid exchange for generation of IAA7$^{KR \rightarrow DD}$ |
| IAA7_KR_to_DD_RV | pGEX-IAA7 | CAACGGTTTCGGAGAAGCCATCATCGCTTCCCACCGCCGATTTGG | K35 to D and R36 to D amino acid exchange for generation of IAA7$^{KR \rightarrow DD}$ |

| | | | |
|---|---|---|---|
| IAA8_FW_del_corrected | pGEX-IAA8(GW) | GGAATTCCAATGTCTT ATCGATTGCTAAGTGTGG | Deletion of gateway recombination and exchange of thrombin clevage site by TEV in pGEX(GW)-IAA8 construct |
| PpIAA1A_deletion_FW | pGEX-PpIAA1A(GW) | GGAATTCCAATGAACGTC AGCGAAGGTTGTAGCACC | Deletion of gateway recombination and exchange of thrombin clevage site by TEV in pGEX(GW)-IAA1A construct |
| PpIAA1B_deletion_FW | pGEX-PpIAA1B(GW) | GGAATTCCAATGAAGTT TAGCAACGAAGTTGTCC | Deletion of gateway recombination and exchange of thrombin clevage site by TEV in pGEX(GW)-IAA1B construct |
| pGEX(GW)_deletion_w/TEV | pGEX(GW) | GGAATTCCGGATCCCTGAAAATAAAG ATTCTCTTTTGGAGGATGGTCGCCACC | Deletion of gateway recombination and exchange of thrombin clevage site by TEV in all pGEX(GW) constructs |
| IAA8_BM1_FW | pGEX-IAA8 | CTTGGTGTTCTGTTTGTG GCGGTGAGCATGGATGGTGC | K203 to A amino acid exchange aiming monomeric IAA8 |
| IAA8_BM1_RV | pGEX-IAA8 | GCACCATCCATGCTCACC GCCACAAACAGAACACCAAG | K203 to A amino acid exchange aiming monomeric IAA8 |
| IAA8_BM2_FW | pGEX-IAA8 | GGATGGTGCTCCGTATCTGG CAGCGGTCGACTTGAGAACTTAC | R213 to A and K214 to A amino acid exchange aiming monomeric IAA8 |
| IAA8_BM2_RV | pGEX-IAA8 | GTAAGTTCTCAAGTCGACCG CTGCCAGATACGGAGCACCATCC | R213 to A and K214 to A amino acid exchange aiming monomeric IAA8 |
| PpIAA1B_BM1_FW | pGEX-PpIAA1B | CGAGCGGGAACCTTGTG GCGATCTACATGGATGGTGTG | K381 to A amino acid exchange aiming monomeric IAA1B |
| PpIAA1B_BM1_RV | pGEX-PpIAA1B | CACACCATCCATGTAGAT CGCCACAAGGTTCCCGCTCG | K381 to A amino acid exchange aiming monomeric IAA1B |
| PpIAA1B_BM2_FW | pGEX-PpIAA1B | GGATGGTGTGCCGTTCGG TGCCGCGGTTGACTTGAAGACG | R391 to A and K392 to A amino acid exchange aiming monomeric PpIAA1B |
| PpIAA1B_BM2_RV | pGEX-PpIAA1B | CGTCTTCAAGTCAACCGCG GCACCGAACGGCACACCATCC | R391 to A and K392 to A amino acid exchange aiming monomeric PpIAA1B |
| PpIAA1A_BM1_FW | pGEX-PpIAA1A | CGAGCGGGAACCTTGTGGC GATCTACATGGATGGTGTGCCG | K362 to A amino acid exchange aiming monomeric IAA1A |
| PpIAA1A_BM1_RV | pGEX-PpIAA1A | CGGCACACCATCCATGTAG ATCGCCACAAGGTTCCCGCTCG | K362 to A amino acid exchange aiming monomeric IAA1A |
| PpIAA1A_BM2_FW | pGEX-PpIAA1A | GATGGTGTGCCGTTCGGTGC CGCGGTTGACTTGAAGACGAAC | R372 to A and K373 to A amino acid exchange aiming monomeric IAA1A |
| PpIAA1A_BM2_RV | pGEX-PpIAA1A | GTTCGTCTTCAAGTCAACCGC GGCACCGAACGGCACACCATC | R372 to A and K373 to A amino acid exchange aiming monomeric IAA1A |
| IAA7_P237G_FW | pGEX-IAA7 | GAAGCAGTTGGACTTGCTG GGAGAGCAATGGAGAAGTAC | Exchange of P237G in IAA7 for generation of the gain-of-function variant AXR2-1 |
| IAA7_P237G_RV | pGEX-IAA7 | GTACTTCTCCATTGCTCTC CCAGCAAGTCCAACTGCTTC | Exchange of P237G in IAA7 for generation of gain-of-function variant AXR2-1 |

# Acknowledgment

This work was accomplished thanks to the contributions of all thesis advisors, collaborators, and colleagues who actively supported my research by providing data, offering scientific advice, teaching me, and engaging in fruitful discussions, for which I will always be grateful.

I must first thank Dr. Luz Irina Calderón Villalobos for her constant guidance and support in all the endeavors I undertook during the project. After her departure from the IPB, Luz Irina trusted me to continue the project without daily supervision. During the one year we worked together at IPB, she taught me many valuable skills related to lab work, presentation preparation, and collaboration management—skills that I will carry with me throughout my professional career. I further appreciate Luz Irina's effort to balance her work at KWS with our weekly meetings, Thesis Advisory Committee (TAC) meetings, and for revising my thesis. She nourished my scientific critical thinking, and in retrospect, I am extremely grateful to have had her as my advisor.

I would like to thank Dr. Anja Thalhammer, who supported me from the very beginning of my journey into Germany's scientific community. Anja opened the doors of her lab at the University of Potsdam and continued to support my work at IPB/RTG 2467 by providing light scattering data for many samples that I shipped to her. I am also thankful for her active participation in the TAC meetings and for her mentorship. I would also like to express my gratitude to Dr. Martin Wolff, who assisted in the analysis of the light scattering data. Martin was always kind, helpful, and patient in our exchanges, and I learned a great deal from him during the process.

I would like to thank Dr. Maria Ott for her support in answering many scientific questions and for allowing me to explore multiple biophysical techniques. I truly enjoyed working with Maria and appreciated her willingness to have open discussions and conduct experiments with me.

I also want to give special thanks to Twinkle Bhatia, who stayed long hours in the lab with me to perform the smFRET and FCCS experiments and analysis.

I extend my gratitude to the Sinz group for their help with the XL-MS experiments and analysis, especially to Dirk Tanzler, Dr. Claudio Iacobucci, and Dr. Christian Ihling. I am also grateful to Prof. Andrea Sinz for her support during the TAC meetings and for encouraging me to attend conferences and share my scientific findings.

A special thanks to the RTG 2467 scientific coordinators, Dr. Lolita Piersimoni and Janet Köppen, for organizing workshops and retreats, and for coordinating external speakers whom I invited to

# Curriculum vitae

Name: Jhonny Oscar Figueroa Parra

Nationality: Venezuelan

**Education and research experiences**

| | |
|---|---|
| 06.2019 - present | Doctorate<br>Faculty of Natural Science – Biological Sciences Martin-Luther University of Halle-Wittenberg Dissertation thesis<br>"Biophysical insights into the conformational flexibility of AUX/IAA transcriptional repressors for auxin sensing"<br>Signal Integration Group/Research training group 2467: Intrinsically Disordered Proteins – Molecular Principles, Cellular Functions, and Diseases.<br>Advisor: Dr. Luz Irina A. Calderón Villalobos<br>Leibniz Institute for Plant Biochemistry, Halle (Saale) |
| 10.2018 – 05.2019 | Research assistant<br>Department of Physical Biochemistry<br>Supervisor: Dr. Anja Thalhammer<br>Potsdam University |
| 10.2014-02.2019 | Studies in Biochemistry<br>Venezuelan Institute for Scientific Research<br>Graduation: Master of science, final grade: 1.9 |
| 10.2007-2013 | Studies in Nutrition and Dietetics<br>Central University of Venezuela, Caracas, Venezuela<br>Graduation: Diploma-Nutrition and Dietetics, final grade: 1.9 |
| 09.2002-07.2006 | High-School education at the "U.E. El Ilustre Americano"<br>Final grade: 1.8 |

**Conference attendances**

Auxin conference 2022, Cavtat (Croatia) (selected talk).

Gordon Research Conference on Intrinsically Disordered Proteins 2022, Les Diablerets (Switzerland).

Plant Science Student Conference, Halle (Saale), GER, 18. - 21.06.2019

Halle (Saale), October 10th, 2023

# List of publications

Niemeyer, M., Figueroa Parra, J.O., Calderón Villalobos, L.I.A. (2023). An In vitro Assay to Recapitulate Hormone-Triggered and SCF-Mediated Protein Ubiquitylation. In: Lois, L.M., Trujillo, M. (eds) Plant Proteostasis. ***Methods in Molecular Biology***, vol 2581. Humana, New York, NY. https://doi.org/10.1007/978-1-0716-2784-6_4

Piersimoni, L., Abd El Malek, M., Bhatia, T., Bender, J., Brankatschk, C., Calvo Sánchez, J., Dayhoff, G. W., Di Ianni, A., Figueroa Parra, J. O., Garcia-Martinez, D., Hesselbarth, J., Köppen, J., Lauth, L. M., Lippik, L., Machner, L., Sachan, S., Schmidt, L., Selle, R., Skalidis, I., Sorokin, O., … Uversky, V. N. (2022). Lighting up Nobel Prize-winning studies with protein intrinsic disorder. ***Cellular and molecular life sciences: CMLS***, *79*(8), 449. https://doi.org/10.1007/s00018-022-04468-y

# Statutory declaration

Hiermit erkläre ich an Eides statt, dass ich mich mit der vorliegenden wissenschaftlichen Arbeit erstmals um die Erlangung des Doktorgrades bewerbe, die Arbeit selbstständig und ohne fremde Hilfe verfasst, nur die angegebenen Quellen und Hilfsmittel genutzt und die den benutzten Werken wörtlich oder inhaltlich entnommenen Stellen als solche kenntlichgemacht habe.

Halle (Saale), den_____          Jhonny Oscar Figueroa Parra_____